

University of Alberta

Microseismic event location using the Double-difference technique for
multiplet analysis

by

Fernando Rafael Castellanos Jurado

A thesis submitted to the Faculty of Graduate Studies and Research
in partial fulfillment of the requirements for the degree of

Master of Science
in
Geophysics

Department of Physics

©Fernando Rafael Castellanos Jurado
Fall 2013
Edmonton, Alberta

Permission is hereby granted to the University of Alberta Libraries to reproduce single copies of this thesis and to lend or sell such copies for private, scholarly or scientific research purposes only. Where the thesis is converted to, or otherwise made available in digital form, the University of Alberta will advise potential users of the thesis of these terms.

The author reserves all other publication and other rights in association with the copyright in the thesis and, except as herein before provided, neither the thesis nor any substantial portion thereof may be printed or otherwise reproduced in any material form whatsoever without the author's prior written permission.

To my mother

To Karla

Abstract

Microseismic event location provides a plethora of information about underground processes such as hydraulic fracturing, steam injection or mining and volcano activities. Nevertheless, accuracy is limited by acquisition geometry and errors in the velocity model and time picks. Although microseismic events can happen anywhere, they tend to re-occur in the same zone. This thesis describes a post-processing technique to relocate events originated in the same source region based on the double-difference method. This technique includes a crosscorrelation procedure to detect similar events and correct time picking errors. The performance of the algorithm is tested on synthetic data and a set of microseismic events recorded in a mine. The method significantly improves locations of similar events, compared to a conventional grid-search algorithm, revealing seismicity patterns likely associated with routine mining operations. The method also includes plots used for quality control of time picking and event location, facilitating geological interpretations.

Acknowledgements

I am very grateful to Dr. Mirko van der Baan for allowing me to be part of the Microseismic Research Consortium group, his patience and way to tackle and simplify problems helped me build a better approach to attack scientific problems.

I would also like to thank my officemates Jiajun and Andres, for all the discussions and support. Special thanks to Melanie, Henry, Jean Baptiste, Josh for the discussions about microseismic monitoring and geophysical topics in general. Every member of the microseismic crew has made this experience invaluable and I am very grateful for that.

Special thanks to the members of my supervisory committee for their insights and feedback: Dr. Claire Currie, Dr. Mathieu Dumbery and Dr. Jeff Gu.

My mother and rest of the family that supported and encouraged me throughout this program. I feel so lucky to have them.

I also thank the sponsors of the Microseismic Research Consortium for supporting this project. Also special thanks to Clinton Keller from Cameco for his insights.

You all made my stay at the UofA an amazing experience which I will never forget.

Contents

1 Introduction.	1
1.1 Background	1
1.2 Main applications	2
1.2.1 Hydraulic fracturing	2
1.2.2 Reservoir monitoring	3
1.2.3 Underground deep mines	5
1.2.4 CO2 sequestration	6
1.2.5 Geothermal energy	7
1.3 Importance of accurate microseismic event locations	8
1.4 Objective of this thesis	11
1.5 Motivation and contribution of this thesis	12
1.6 Thesis structure	13
2 Pre-processing: Theory.	14
2.1 Introduction	14
2.2 Noise attenuation	14
2.3 Event detection	16
2.4 Arrival time picking	19
2.5 Velocity model building	20

3	Location techniques in microseismic monitoring: Theory.	24
3.1	Introduction	24
3.2	Direct-Search Methods	24
3.3	Linearized Methods	27
3.3.1	Single Event technique	27
3.3.2	Master Event technique	29
3.3.3	Double-Difference technique	30
3.3.4	Other techniques	30
3.4	Synthetic Example	31
3.4.1	Lookup-table	31
3.4.2	Effect of time picking errors	32
3.4.3	Effect of velocity model	35
3.4.4	Effect of receiver array	36
4	Multiplets and Double-difference technique: Theory.	39
4.1	Introduction	39
4.2	Event similarity	40
4.2.1	Crosscorrelation method	40
4.2.2	Clustering doublets into multiplets	43
4.3	P-wave time repicking method	44
4.4	Double-difference method	46
4.4.1	Matrix structure	49
4.4.2	Solution	49
4.4.3	Weighting scheme	50
4.5	Application to synthetic data	52
4.5.1	Effect of noise	57
4.5.2	Effect of velocity	60
4.5.3	Effect of receiver array	63

5	Case study: Background.	66
5.1	Introduction	66
5.2	Geological setting	66
5.3	Geological challenges	68
5.3.1	Water inflow incidents	68
5.4	Microseismic installation	71
5.5	Problems encountered	73
6	Case study: Pre-processing.	77
6.1	Introduction	77
6.2	Bandpass filter	77
6.3	Automatic event detection and onset picking	79
6.4	Velocity model used	84
6.5	Absolute event location	84
7	Case study: Multiplets and Double-difference technique.	89
7.1	Introduction	89
7.2	Event similarity	89
7.3	P-wave time repicking	93
7.4	Weighting scheme	95
8	Discussion.	110
8.1	Mining data interpretation	110
8.1.1	Pattern of multiplets occurrence over time	110
8.1.2	Blasting activities	112
8.1.3	Interpretation of largest multiplet groups	118
8.2	Pre-processing workflow	124
8.3	Doublet definition	125
8.4	Relocation algorithm	125
8.5	Weighting scheme	126

9 Conclusions.	128
9.1 Further research	129
Bibliography	130
A Appendix: Partial derivatives determination	138

List of Tables

3.1	Computation times using a lookup-table.	31
3.2	Effect of velocity errors in event locations.	35
7.1	Number of events per multiplet group.	90
8.1	Master advance of blasting activities.	116

List of Figures

1.1	Histogram of the word "microseismic" on online libraries.	2
1.2	Typical microseismic monitoring geometry.	3
1.3	Example of Cyclic Steam Stimulation (CCS).	5
1.4	Microseismic monitoring in mining activities.	7
1.5	Seismograms with low and high SNR.	9
1.6	Impact of SNR on microseismic event patterns.	10
2.1	Illustration of trapezoidal filter.	15
2.2	Bandpass filter application.	16
2.3	Illustration of <i>STA/LTA</i> method.	17
2.4	Example of <i>STA/LTA</i> event detection algorithm.	18
2.5	Illustration of the <i>MER</i> method.	19
2.6	Autoregressive time picking example.	20
2.7	Common sonic log in microseismic monitoring.	22
2.8	Conventional workflow for velocity model building.	22
2.9	Artifacts due to erroneous velocity model.	23
3.1	Illustration of lookup table	27
3.2	Lookup-table processing times.	32
3.3	Hypocenter probability density when adding random errors.	33
3.4	Location errors versus noise percentage.	34
3.5	Hypocenter probability density for different data uncertainties σ	34
3.6	Hypocenter probability density for different velocity percentages.	36
3.7	Location error versus velocity perturbations.	37

3.8	Hypocenter probability density for different receiver arrays.	38
4.1	Crosscorrelation versus distance for synthetic data.	42
4.2	Chain-like linkage for multiplet detection.	43
4.3	Illustration of repicking method using crosscorrelation.	45
4.4	Illustration of the double-difference technique for multiplets relocation.	46
4.5	Location with noise-free time readings.	53
4.6	Location with noise-free time readings and random initial locations.	54
4.7	Event locations when using true barycenter as initial locations.	55
4.8	Event locations when using shifted initial locations.	56
4.9	Location using travel times with 10% of added random noise.	58
4.10	Discrepancy as a function of noise present in time readings.	59
4.11	Location using an underestimated velocity model.	61
4.12	Location using an overestimated velocity model.	62
4.13	Location using two receiver boreholes aligned with the cluster strike.	64
4.14	Location using two boreholes orthogonal to the cluster strike.	65
5.1	Geographical location of Athabasca Basin and Cigar Lake mine.	67
5.2	Geological map of Northern Saskatchewan.	69
5.3	Cross sectional view of the Cigar Lake mine.	70
5.4	Receiver setup at Cigar Lake project.	72
5.5	Total triggered event files from January to March 2011.	73
5.6	Seismogram file triggered by noisy arrivals.	74
5.7	Seismogram with synchronization problems.	75
5.8	Residual times for all detected events from January to March 2011.	76
6.1	Effect of bandpass filter on a microseismic event.	78
6.2	<i>STA/LTA</i> method to detect microseismic signals.	80
6.3	Interactive procedure to activate, deactivate or edit P-wave time picks.	81
6.4	Percentage of time picks available.	83
6.5	1-D layered isotropic velocity model.	84
6.6	Initial locations using a 1-D layered isotropic velocity model.	86
6.7	Initial locations using a homogeneous velocity model.	87

6.8	Histogram of residuals of detected seismicity.	88
6.9	Depth distribution of detected seismicity.	88
7.1	Four similar microseismic events recorded at a common station.	90
7.2	Percentage of multiplets as a function of minimum correlation level.	91
7.3	Histogram of events per multiplet group.	91
7.4	Upper triangular crosscorrelation matrix.	92
7.5	P-wave time repicking method.	93
7.6	Histogram of time lags between doublets in multiplet group 1.	94
7.7	Distance-based weighting using $a=1$, $b=7$ and $dmax=700$ m.	96
7.8	Distance-based weighting using $a=3$, $b=7$ and $dmax=700$ m.	97
7.9	Crosscorrelation-based weighting.	98
7.10	Relocation using crosscorrelation-based weighting.	100
7.11	Multiplet group 1 after relocation.	101
7.12	Crosscorrelation versus inter-event distance for multiplet group 1.	102
7.13	Relocation vectors for multiplet group 1.	103
7.14	Histogram of separation distance between events in multiplet group 1.	104
7.15	Relocation of multiplet group 3.	105
7.16	Crosscorrelation versus distance for multiplet group 3.	106
7.17	Relocation vectors for multiplet group 3.	107
7.18	Relocation of all multiplet groups.	109
8.1	Gantt chart showing multiplets occurrence.	111
8.2	Comparison microseismic event versus blast signal.	113
8.3	Amplitude spectrum of microseismic event and blast signal.	113
8.4	Temporal distribution of triggered files during January 2011.	114
8.5	Blasting activities during January 4th, 2011.	115
8.6	Hourly seismicity and blasting activities in January 2011.	116
8.7	Crosscorrelation matrix for blasts during January 2011.	117
8.8	Histogram of amplitudes of microseismic events.	119
8.9	Histogram of S-to-P wave amplitude ratios.	120
8.10	Relocations of multiplet group 1.	121
8.11	Relocations of multiplet group 3.	122
8.12	Relocations of multiplet group 4.	123

List of Symbols and Abbreviations

1-D: One-dimensional.

2-D: Two-dimensional.

3-D: Three-dimensional.

a : Autoregressive method coefficient.

a and b : Exponential values for distance weighting.

A : Maximum amplitude of seismogram.

AECL: Atomic-Energy of Canada Limited.

$AR - AIC$: Autoregressive Akaike Information Criterion.

Az : Backazimuth.

BH: Borehole.

CF: Characteristic function.

CSS: Cyclic Steam Stimulation.

CCS: Carbon Capture and Storage.

C_1 : Constant.

C : Crosscorrelation value between two events at a specific component.

CC : Crosscorrelation value between two events.

DD: Double-difference.

d : Exponential value for crosscorrelation weighting.

$dmax$: Maximum inter-event distance allowed in relocation method.

EAGE: European Association of Geoscientists and Engineers.

EDZ: Excavation damaged zone.

EGS: Enhanced Geothermal Systems.

EOR: Enhanced Oil Recovery.

f : Frequency.

f_1, f_2, f_3, f_4 : Corner frequencies of trapezoidal bandpass filter.

\mathbf{G} : Partial derivative matrix.

H1-comp and H2-comp: Horizontal components of seismogram.

\mathbf{I} : Identity matrix.

l_1, l_2 : Lengths of short and long time windows in *STA/LTA* method.

MS: Microseismic.

master: Superscript for master event data.

M : Autoregressive model order.

MER: Modified energy ratio.

\mathbf{m}_0 : Initial guess of hypocenter location for a single event.

\mathbf{m} : Current hypocenter location for a single event.

NW-SE: Northwest-Southeast.

N : Number of events.

nsta: Number of receivers.

obs and *cal*: Subscripts for observed and calculated data.

P : Number of parameters of the Autoregressive Akaike Information Criterion.

pdf: Probability density function.

QC: Quality control.

rel: Superscript for relative data.

SAGD: Steam-Assisted Gravity Drainage.

SEG: Society of Exploration Geophysicists.

SNR: Signal-to-noise ratio.

SPE Society of Petroleum Engineers.

S-N: South-North.

S : Semblance trace.

STA/LTA: Short term to long term average ratio.

SVD: Singular value decomposition.

s: Inter-event distance for distance weighting.

slave: Superscript for slave event data.

t: Time.

URL: Underground Research Laboratory.

$u(t)$: Preprocessed trace.

V_p : P-wave velocity.

W-E: West-East.

W: Weighting matrix.

$x(t)$: Seismic trace.

$X(f)$: Fourier transform of seismic trace.

Z-comp: Vertical component of seismogram.

α : Scaling factor for crosscorrelation weighting.

λ : Damping factor.

$\Delta X, \Delta Y, \Delta Z, \Delta T$: Node spacing in grid.

$\Delta \mathbf{m}$: Perturbation vector.

$\Delta \mathbf{X}, \Delta \mathbf{Y}, \Delta \mathbf{Z}, \Delta \mathbf{T}$: Perturbation to hypocentral parameters.

$\Delta \mathbf{d}$: Residual vector.

ρ_D : Probability density of hypocenter location.

$\sigma_p, \sigma_s, \sigma_{Az}$: Uncertainties in P and S-waves time picks and backazimuth observations.

τ : Time lag between two events.

φ : Backazimuth measurement.

CHAPTER 1

Introduction.

1.1 Background

Over the last several years, analysis of small-scale earthquakes has grown as a geophysical method to provide information about underground processes. This method is called microseismic (MS) monitoring. It consists of deploying sensors called geophones or accelerometers (downhole, at shallow depths or at the surface) that detect ground motions due to seismic energy occurring underground. This energy can be associated with a specific industrial process, human activity or natural phenomena. As the technique analyzes seismic waves, microseismic monitoring has taken most of its theory from earthquake seismology, it is a direct application of seismology principles that have been used and tested for decades.

The first application of microseismic monitoring was induced seismicity in the mining and geothermal industries. MS monitoring started in the oil and gas industry in the 1970s, where a controlled injection was used to prove the occurrence of induced seismicity [Raleigh et al., 1976]. Nevertheless, it is only in the last two decades that it has gained more acceptance, especially after the successful hydraulic fracturing imaging of the Barnett Shale, Forth Worth Basin in 2000 [Maxwell et al., 2002].

Figure 1.1 shows the number of papers (mainly published by SPE, SEG and EAGE among others) discussing the technology. This gives an idea of the rapid increase in the discussion of this technique, especially after efforts have been focused on extracting new sources of energy. MS monitoring has cross-disciplinary interests, so its main applications will be briefly introduced in the next section.

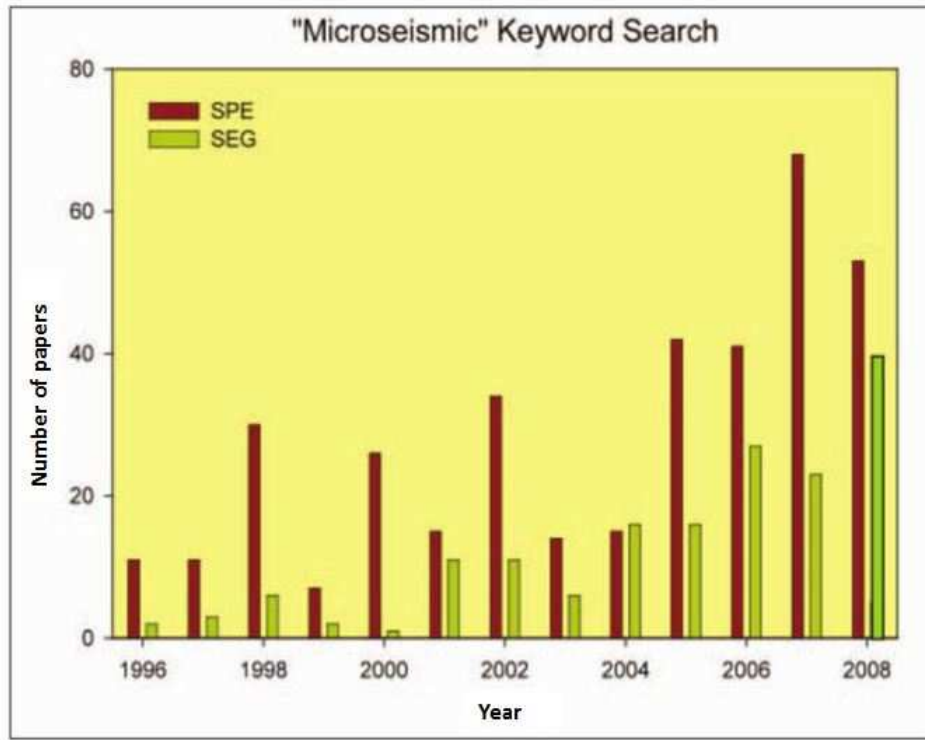


Figure 1.1: Histogram of the hits from a keyword search on "microseismic" in the SEG and SPE online libraries. Taken from Maxwell [2010a].

1.2 Main applications

1.2.1 Hydraulic fracturing

Microseismic monitoring on hydraulic fracturing stimulations is a very common application, especially in North America, with the largest effort from the engineering community [Maxwell, 2010b]. The petroleum industry is targeting unconventional reservoirs which have low permeability (tight sandstones, shale gas), so hydraulic fracturing has been widely used to stimulate production, by increasing the permeability in the reservoir, so hydrocarbons can migrate to the production well. This process involves the injection of slurry water at high pressure to create tensile fractures, as a proppant (usually sand or ceramic) is also introduced during the injection to keep the fractures open, which allows for a conductive flow path for hydrocarbons. This process, also commonly called "fracking", is usually performed in different stages, depending on the reservoir targets, at different positions along the well. To design the stimulation procedure and parameters, microseismic monitoring can image

the hydraulic fracturing process. It is an invaluable tool since it allows us to detect, locate and further analyze rock failure associated with the fracturing process, so operators can interpret fracture geometries, possible fracture networks, interactions with existing faults and seismicity out of zone. An additional major benefit is its real-time applicability for fracture mapping, so operators can quickly assess and adjust pumping and stimulation parameters such as pump rate, fluid properties, and volume, to optimize the stimulation within its original design criteria [Pei et al., 2008].

Figure 1.2 illustrates the principles of microseismic monitoring, where multiple receivers are positioned in a vertical interval in a single nearby offset well at a reasonable distance from the fracture and the receivers near to the depth of the fracture treatment. Different published papers have addressed the imaging of fractures [Warpinski et al., 1999, Fischer et al., 2008, Verdon and Kendall, 2011], motivated by the increasing interest in the hydrocarbon industry to move to unconventional resources. Thus, the need to develop techniques such as MS monitoring that contributes to a better understanding of fractures in situ is key to optimizing operations and reduce the environmental impact.

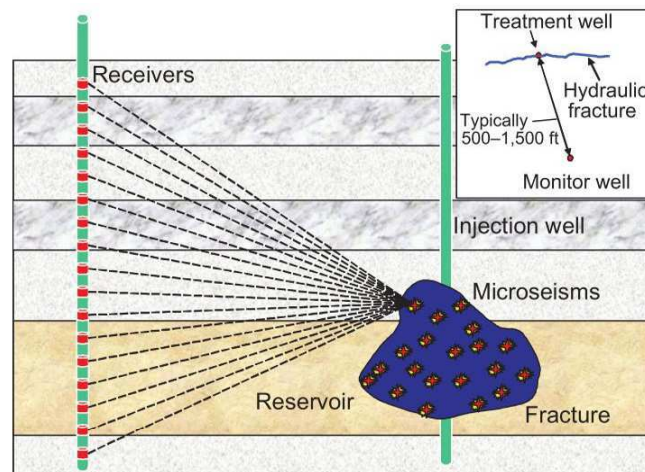


Figure 1.2: Side view of a typical monitoring geometry. Taken from Warpinski [2009].

1.2.2 Reservoir monitoring

Microseismic techniques can be used to monitor steam injection for enhanced oil recovery. Cyclic-Steam Stimulation (CSS) and Steam-Assisted Gravity Drainage (SAGD) are technologies used for the economic development of unconventional reservoirs. The most common

is CCS, also known as the Huff and Puff method, and consists of three stages: injection, soaking, and production (Figure 1.3). Steam is first injected into a well for a certain amount of time to heat the oil in the surrounding reservoir to a temperature at which it flows. After it is decided enough steam has been injected, the steam is usually left to soak for some time after, typically not more than a few days. Then oil is produced out of the same well, at first by natural flow (the steam injection will have increased the reservoir pressure) and then by using other mechanical means to lift the oil to the surface. Production will decrease as the oil cools down, and once production reaches an economically determined level the steps are repeated again. Tracking the deformation associated with production of heavy oil recovery is critical, as production can be optimized, confine the stimulation to the reservoir and identify bypassed regions [Maxwell et al., 2007]. Steam injection results in geomechanical strains associated with increased pore pressure, thermal stress changes and dramatic changes in material properties associated with heating the reservoir sufficiently to mobilize the heavy oil bitumen. This geomechanical deformation may be expressed through seismic deformation and the release of seismic energy as fractures adjust to the strain field [Maxwell et al., 2003], and also may result in surface expansion or subsidence [Davis et al., 2000]. Monitoring the microseismic activity, combined with other technologies such as sensitive seismometers and precise tiltmeters could also allow us to detect and better understand the geomechanical and surface deformation associated directly with the steam injection [Maxwell et al., 2007]. These induced-microseismic events usually emit very low seismic signals so they can only be detected with microseismic arrays. Additionally, it has also been used in the surveillance of accidents related to heavy oil production, such as well casing failures, cement cracking [Smith et al., 2002]. These failures, if overlooked, may cause serious environmental impact to groundwater and surface water resources. Hence, MS monitoring is considered a valuable tool for monitoring purposes.

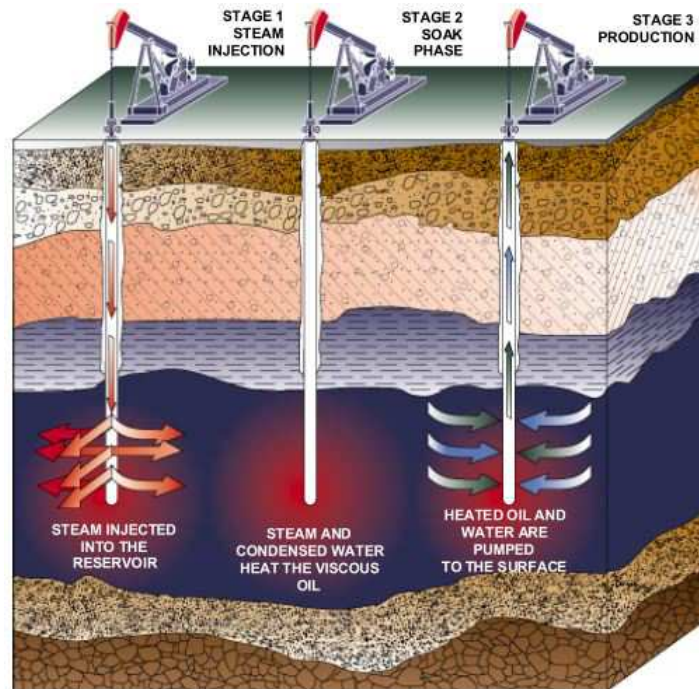


Figure 1.3: Example of Cyclic Steam Stimulation (CSS) for heavy oil extraction. In this Figure, the three-stage process taking place all in the same well is as follows; stage 1, steam is injected into the reservoir; stage 2, steam and condensed water heat the viscous oil; stage 3, heated oil and water are pumped to the surface. Taken from <http://www.limperiale.ca>.

1.2.3 Underground deep mines

Microseismic monitoring has been used in the mining industry for several decades. It started in the late 1930s, when two scientists from the U.S Bureau of Mines, L. Obert and W.I. Duvall, were conducting an experiment to measure seismic velocities in mine pillars in North-eastern Oklahoma. The receivers used detected seismic energy from unknown sources. After some further field studies, they realized these events were generated by stressed rocks. This triggered the use of microseismic monitoring for ground control and safety in mines. In the early 1960s, South African researchers created a system able to determine rock burst locations at deep gold mines [Cook, 1963]. This can be considered a major development at that time, since it demonstrated the possibility to study rock burst location, one key problem in mine installations.

In the middle 1980s and early 1990s, there were tragedies in Canadian mines. For instance, on June 20, 1984, a rock burst took the lives of four miners at Falconbridge No. 5 Shaft

near Sudbury, Ontario. This triggered community concerns about risk and health environment in the mining industry. Consequently, to better understand rock behaviors and hazard assessment within mines, a large scale research program was carried out jointly by the federal government, universities and mining companies, which allowed an improvement of the microseismic technique for the Canadian mining industry.

Nowadays, microseismic installation has been used extensively for monitoring mine infrastructure and surroundings [Pandey et al., 1995, Butt et al., 1997, Richardson and Jordan, 2002], as it gives information about the local stress of the rock mass, representing a useful tool for analyzing ground control and hazards in mines. If seismic energy is located, operators can learn where this seismicity is occurring and, if analyzed in real-time, the causes of rock bursts can be assessed in a short time, taking into account the geology, the mine infrastructure and stress conditions (Figure 1.4). Moreover, MS monitoring can identify unknown pre-existing faults or fractures. As a result, subsequent work on the mine can be reevaluated to mitigate or reduce the risk for rock bursts, slope instability or underground gas emissions. Additionally, it can be used to track caving front propagation, for mine sequence optimization and validation of pre-existing geomechanical mine models. It can be used to understand the rock mass response to the creation of underground openings before the design of structures such as transportation tunnels, shafts and emplacement rooms [Read, 2004]. Institutes such as the Underground Research Laboratory (URL), operated by Atomic-Energy of Canada Ltd (AECL) have studied the response to excavation processes, with the purpose of assessing the feasibility of safe disposal of nuclear fuel in a stable excavation in a low permeability rock mass.

Response of excavation processes have been studied by institutes such as the Underground Research Laboratory (URL), operated by Atomic-Energy of Canada Ltd (AECL), with the purpose to study the feasibility of safe disposal in nuclear fuel in a stable excavation in a low permeability rock mass.

1.2.4 CO₂ sequestration

Carbon Capture and Sequestration has been addressed as a possible way of reducing greenhouse effects. The main question is whether CO₂ remains safely within the reservoirs and stays there for a long time. As a result, microseismic monitoring has been used to track the progress of the CO₂ flood to ensure compliance target zones. This is crucial to better ensure integrity of the overlying seal rock, since microseismic event locations can reveal open

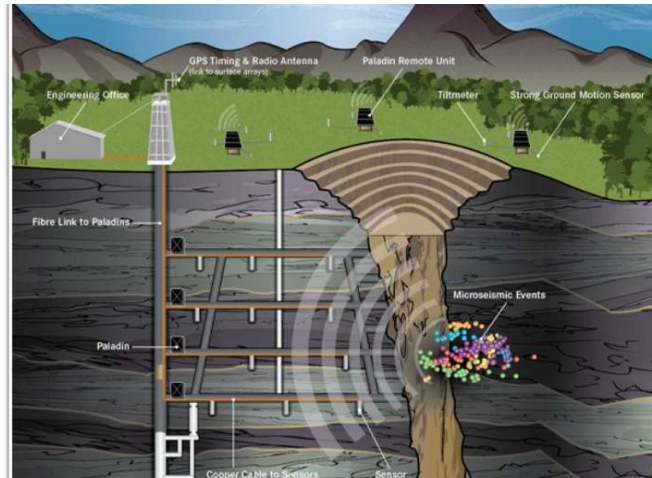


Figure 1.4: Illustration of microseismic events created in an open-pit mine. Taken from <http://www.esgsolutions.com>

fractures, related to excess deformation, which may provide pathways for CO₂ leakage from the reservoir [Verdon et al., 2011]. Moreover, it might also be necessary to combine fracture mapping with geomechanical models to reduce the concerns about the fate of the carbon dioxide over the 10 000 yr period required for storage [Bickle et al., 2007] and assess possible migration along pre-existing faults or fracture networks. As any sequestration program should be monitored, microseismic technologies are ideal to ensure injected gases stay in the storage areas, and that no environmental damages or safety concerns emerge.

1.2.5 Geothermal energy

Enhanced Geothermal Systems (EGS) has much promise as a way to obtain energy from a geothermal source. In the past, it was required to have a natural geothermal source such as geysers or hot aquifer. Nowadays, EGS extract geothermal energy from large amounts of hot dry rock using hydraulic fracturing stimulations. When fractures are created, water injected into the formation through injection wells travels through the fractures, acquiring heat from the rock [Michelet and Toksöz, 2007]. The resulting hot water is then pumped out production wells where it is used to generate electricity. Microseismic monitoring comes into play because it allows mapping the fractured rock volume after hydraulic fracture stimulations [Phillips et al., 1997, Fehler et al., 2001, Rowe et al., 2002]. It allows observing and assessing in the field the behavior of the geothermal reservoir and identifying properties that can impact the operations.

1.3 Importance of accurate microseismic event locations

As briefly explained in the former section, microseismic monitoring has gained importance as a geophysical method, due to its several applications, especially in the oil and gas industry. The basic objective of MS monitoring is to determine where (spatial coordinates) and when (origin time) a microseismic event occurred. A more accurate event location will certainly lead to a better understanding and interpretation of the associated underground process; hence, it is crucial to identify the main sources of uncertainty in event locations. According to Pavlis [1992], accuracy in event locations is mainly affected by three factors: a poor source-receiver configuration, errors in time picks and errors in the velocity model. Depending on factors such as depth of the target, areal extent, and economic constraints, an array of receivers can be placed downhole (in a single or multiple observations wells), at the surface (or near the surface). Thus the type of array will be sensitive to certain directions [Eisner et al., 2009]. For example, when using a single receiver array, a very common array design in hydraulic fracturing, trilateration or travel-time inversion methods do not provide accurate results, so particle polarizations of P- and S-waves are usually used since they give an additional constraint on the direction where the event came from [Pearson, 1981, Phillips et al., 1989, Fischer et al., 2008].

With regards to the velocity model, for most surface and downhole projects, this information is determined from sonic logs recorded in a nearby well [Eisner et al., 2009]. In general, a 1-D velocity model is usually used, as calibration shots are recorded and used to refine or "calibrate" the current velocity model using known source locations. Nevertheless, the Earth is a complex structure so the final velocity model rarely represents its exact true velocities, due to unanticipated velocity structures and heterogeneities.

Relative location methods such as master-event [Poupinet et al., 1984, Fremont and Malone, 1987] and double-difference [Waldhauser and Ellsworth, 2000] have been used in earthquake seismology to reduce source-receiver path effects [Gibbons and Ringdal, 2006, Zhou et al., 2009]. With regards to time picking, accuracy can be obtained by human interaction when using small data sets; however, for larger data sets, automatic methods based on STA/LTA [Allen, 1978] and modified versions [Akram and Eaton, 2012] and the Akaike Information Criterion (AIC) [Sleeman and van Eck, 1999], have been applied to microseismic data. These errors in time picking are affected by inherent uncertainties in signal quality that impact the confidence in the estimated location. Another advantage when using relative methods is that location accuracy can also be improved by improving relative arrival time readings between similar events through crosscorrelation methods [Poupinet et al., 1984,

Vandecar and Crosson, 1990].

Background noise due to conditions in wellbore, drilling and production operations can have a major impact on the recorded signal. Also, instrumental noise associated to the acquisition system can obscure the desired seismic waveforms. Figure 1.5 shows the effect of SNR on signal quality; uncertainty in P-wave and S-wave arrival time increases with decreasing SNR, and arrival times may not even be detected on all sensors in the array. These errors will have a direct effect on event location accuracy.

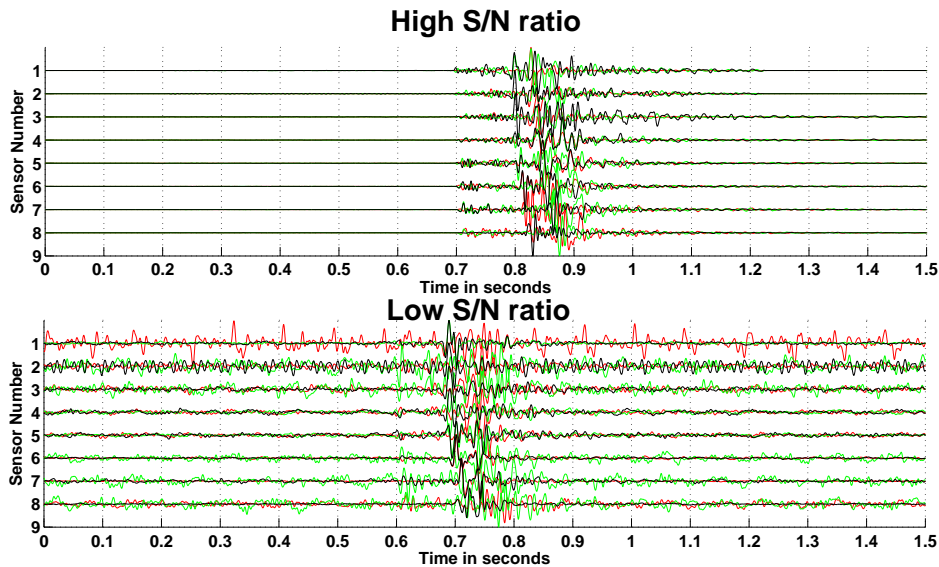


Figure 1.5: Top: Seismogram with high SNR. Bottom: Seismogram with low SNR. Note that it is more challenging to pick arrival times in seismograms with low SNR, hence it is more likely to pick an incorrect arrival.

As mentioned earlier, event location uncertainty thus increases as SNR decreases, requiring an evaluation of event quality to be included in the interpretation. In most cases a minimum SNR between two and three is used as a cutoff when reporting events [Cipolla et al., 2011]. Nevertheless, a higher SNR cutoff may be used in the interpretation to avoid misinterpreting uncertainty. Figure 1.6 shows that using a lower SNR threshold could lead to an interpretation of a complex fracture growth, whereas a higher SNR threshold indicates a simple planar fracture. The decision of which SNR threshold is most appropriate depends on the specific data set, since the number of events detected and source-receiver offset sometimes do not allow for an exclusion of lower quality events. A way to circumvent this is by filtering the data, in order to enhance the SNR, since it will allow for a more precise time picking

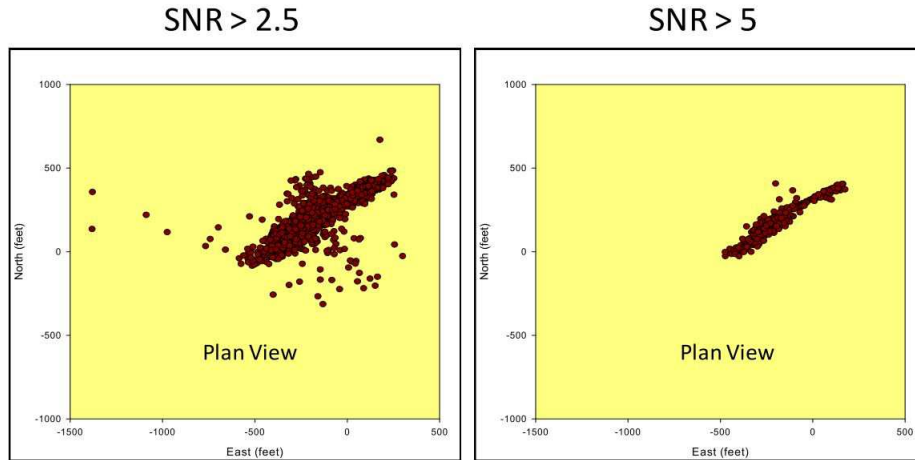


Figure 1.6: Impact of SNR on microseismic event patterns. Two different interpretations can be obtained depending on the quality of microseismic events. Taken from [Cipolla et al., 2011].

(manual or automatic).

Accurate microseismic locations have several benefits. For instance, in hydraulic fracturing, the fracture propagation is not always as operators expect, so an accurate location will produce a better determination of fracture orientation and geometries (length, size, height), reveal possible fracture networks and provides less ambiguity when locating seismicity out of zone and when performing numerical simulations of the fracturing [Maxwell and Urbancic, 2002]. These features allow for a more effective intervention during stimulation, to improve the pumping parameters and give operators an updated image of fracture growth. In reservoir monitoring, microseismic monitoring can track pressure changes associated with either fluid or gas injection, thus event locations are crucial to indicate preferential paths where fluid flow is confined [Phillips et al., 1997, Rowe et al., 2002, Michelet and Toksöz, 2007]. In the mining industry, rock bursts are often related to interaction of varying stress fields, so accurate determination of microseismic locations may yield better insights of possible causes of rock bursts. Accurate mining microseisms represent a particular challenge, given the usual complexity of the infrastructure and geological setting. For instance, propagation effects have been documented, where tunnels delay P-wave travel times [Maxwell and Young, 1998]. In the last few years, tomographic imaging has been documented to analyze stress redistributions, where event locations are used to generate tomograms, i.e., accurate locations can provide insights with regards to where we can identify zones with high stress loading (high velocities) and damaged zones (low velocities) [Westman et al., 2012].

In order to obtain accurate locations, a relative relocation technique is under investigation in this thesis, which combines multiplet analysis and the double difference algorithm. Multiplet analysis allows to detect microseismic events with nearly-identical waveforms, often called doublets (two similar events) and multiplets (more than two similar events) as they are assumed to come from similar source regions and have similar source mechanisms. Once groups of similar events are detected, the double difference technique is used to relocate these events, since the technique takes advantage of ray path similarity, i.e. two collocated events have identical ray-paths from the source region to the receiver, except in the source region where both events differ [Waldhauser and Ellsworth, 2000]. This leads to minimization of the effects of unanticipated velocity structures in the final locations. In this thesis, location accuracy between similar events is also improved through cross-correlation [Poupinet et al., 1984, Vandecar and Crosson, 1990]. Moreover, compared to a master event approach, the double-difference technique has an advantage, it does not rely on one master event, i.e. double-difference residuals are calculated for all possible event pairs in a multiplet group, so there is no spatial limit as there is for the master event case, and no bias is produced when crosscorrelating noisy master events [Fremont and Malone, 1987, Deichmann and Garcia-Fernandez, 1992, Waldhauser and Ellsworth, 2000]. A weighting scheme based on crosscorrelation values and inter-event distances plays a major role in this process, since it emphasizes observations of similar event pairs, i.e. correlated, over dissimilar events (uncorrelated).

This technique is useful because it can better delineate dike penetration [Rubin and Gillard, 1998, Murase et al., 2010], it can help differentiate between volcanism and faulting systems [Shaw and Lin, 1993]. It is also used for understanding volcano-tectonic seismicity, such as precursors, to monitor restless volcanoes [Roman and Cashman, 2006] and other types of events such as nuclear explosions [Waldhauser et al., 2004]. Velocity variations [Poupinet et al., 1984], migration of fluids in source regions [Tselentis, 1993] or better delineate faults geometry in microseismic or seismology scales have also been studied [Got et al., 1994, Waldhauser and Ellsworth, 2000, Moriya et al., 2003, De Meersman et al., 2009]. Most recently, earthquake doublets have revealed that the Earth's solid inner core rotation with respect to the mantle varies with time, as fluctuations in the rotation rate explain discrepancies in previous core rotation models [Tkalčić et al., 2013].

1.4 Objective of this thesis

The objective of this study is to develop a novel microseismic processing sequence that uses in the post-processing stage multiplet analysis and a relocation procedure based on

the double-difference technique to accurately relocate microseismic events from a dataset recorded by multiple borehole arrays near a mine. Both techniques combined seek to reduce the effects of velocity heterogeneities as they take advantage of the assumption that pairs of similar events have near-identical source-receiver raypaths. Due to the fact that essentially collocated events have near-identical waveforms, crosscorrelation methods can detect accurately relative shifts in position despite mispicks or missing time picks and unknown velocity structures, targeting two of the main sources of uncertainty in seismic locations suggested by Pavlis [1992].

1.5 Motivation and contribution of this thesis

The contributions of this thesis can be summarized as:

- Provide a microseismic processing sequence for the case of multiple observation wells, with stages including: bandpass and notch filtering, automatic time picking and repicking, interactive time pick quality control and absolute event location based on a grid search algorithm.
- Exemplify a method to identify similar events based on waveform coherency. This allows identifying multiplet groups (clusters of similar events), which is a usual step before applying any relative relocation algorithm.
- Develop a post-processing technique that uses time repicking and the double-difference relocation algorithm for the case of microseismic data. Microseismic event locations are usually affected by time picking uncertainties and unanticipated velocity structures. The aforementioned techniques aim to reduce these two sources of uncertainty.
- Emphasize the importance of the weighting scheme in the double-difference algorithm for microseismic data. Focus has been given to weighting based on correlation and separation distance between events and how these parameters change depending on the specific microseismic data set. The weighting scheme controls the importance of each observation during the inversion procedure. It also controls the compromise between using most information available and keeping the computational times at a reasonable level. Also, the effect of matrix normalization before solving the inverse problem is introduced.
- Demonstrate improvement in relative locations compared to absolute locations and describe plots that reveal uncertainties in time picks and seismic locations for quality control purposes.

1.6 Thesis structure

Chapter 1 Presents the different applications of microseismic monitoring and the importance of accurate microseismic event locations.

Chapter 2 Provides general background theory for processing of microseismic data recorded by multiplet arrays.

Chapter 3 Provides general background theory about event location techniques in microseismic monitoring.

Chapter 4 Presents the theory on multiplet detection and the double-difference technique for microseismic data. Most part of this chapter is taken from Castellanos and van der Baan [2013].

Chapter 5 Presents the case study: a data set recorded near a mine. The geologic setting, microseismic installation and problems encountered are addressed.

Chapter 6 Describes the application of the pre-processing workflow on the case study.

Chapter 7 Describes the applications of multiplet detection and the double-difference technique. Most part of this chapter is taken from Castellanos and van der Baan [2013].

Chapter 8 Contains the interpretation of the results presented in the previous chapter.

Chapter 9 Presents the concluding remarks of this research.

CHAPTER 2

Pre-processing: Theory.

2.1 Introduction

This chapter discusses the theory of basic microseismic processing steps. The selection of the appropriate workflow depends on the type of data available, noise present and receiver array. The following workflow applies for microseismic installation where multiple receiver arrays have been adopted. Noise attenuation based on bandpass filters contributes to enhance the SNR, a step necessary for more accurate event detection and onset time picking, which results in more accurate event locations. Also, microseismic waveforms need to be filtered as in further steps a waveform similarity assessment will be done to identify events originating in the same source region. For multiple receiver arrays, such as the case study presented in this thesis, there is a reasonably good azimuthal coverage, therefore, it is not required to measure backazimuth measurements, and as a result, the process of polarization analysis is skipped. The step of velocity model building is also discussed in this chapter.

2.2 Noise attenuation

Noise is considered as any unwanted signal that interferes with the desired signal (P and S-waves). They can be divided into incoherent and coherent noise and both types affect the quality of the seismograms in microseismic data. Given the small magnitude of microseismic events (< 0), any noise recorded will impact the signal-to-noise ratio and is an obstacle in microseismic detection since it might obscure weak events. Incoherent noise is of random nature, and its characteristics vary from receiver to receiver with different waveforms and energy levels. Examples of coherent noise include waves propagating within the borehole

casing and noise generated by pumping equipment. In addition, tube waves or interface waves, can be generated due to discontinuities inside the borehole, e.g. when a P-wave compresses a fluid filled fracture and injects a fluid pulse into the borehole [St-Onge and Eaton, 2011]. To attenuate these undesired signals, bandpass filtering is a commonly used step in microseismic analysis to remove the frequency content associated with them. It consists of preserving frequencies within a certain range and rejects (attenuates) frequencies outside that range (Figure 2.1). This step works well in MS monitoring for most situations except when the desired signals, P- and S-waves, share similar frequencies with noise. An ideal bandpass filter would have a completely flat band (no gain/ attenuation) and would completely attenuate frequencies outside the band. However, no filter is ideal, since it does not attenuate all frequencies outside the desired range. Within the transition zone, called roll-off, the frequencies are attenuated but not rejected, and is usually expressed in dB of attenuation per octave or decade of frequency.

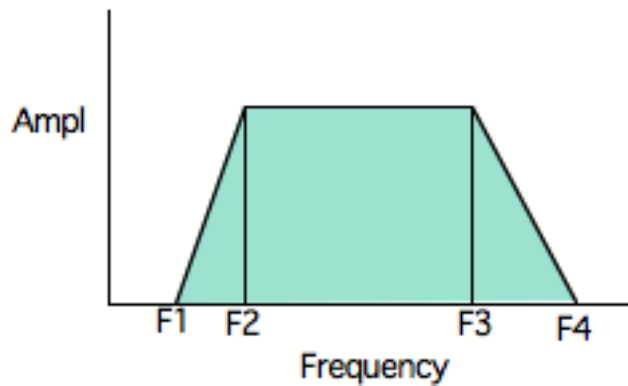


Figure 2.1: Illustration of trapezoidal filter used in this thesis. f_1 , f_2 , f_3 , and f_4 are the corner frequencies of a trapezoidal frequency bandpass filter. The frequencies preserved range between f_2 and f_3 . Frequencies lower than f_1 and greater than f_4 are removed and frequencies within $f_1 < f < f_2$ and $f_3 < f < f_4$ are attenuated according to their slopes.

Figure 2.2 illustrates the bandpass filtering effects on a single trace contaminated with Gaussian noise. Note the bandpass filter has enhanced the SNR of the trace. As a result, a cleaner trace will allow for more accurate onset time picking, which leads to better microseismic locations. In waveform similarity analysis, noise attenuation is of paramount importance, e.g. crosscorrelation methods used for doublet detection and master event techniques assume the time windows for analysis contain only waveforms originated due to the source event [Poupinet et al., 1984, Got et al., 1994, Moriya et al., 1994, Arrowsmith and Eisner, 2006].

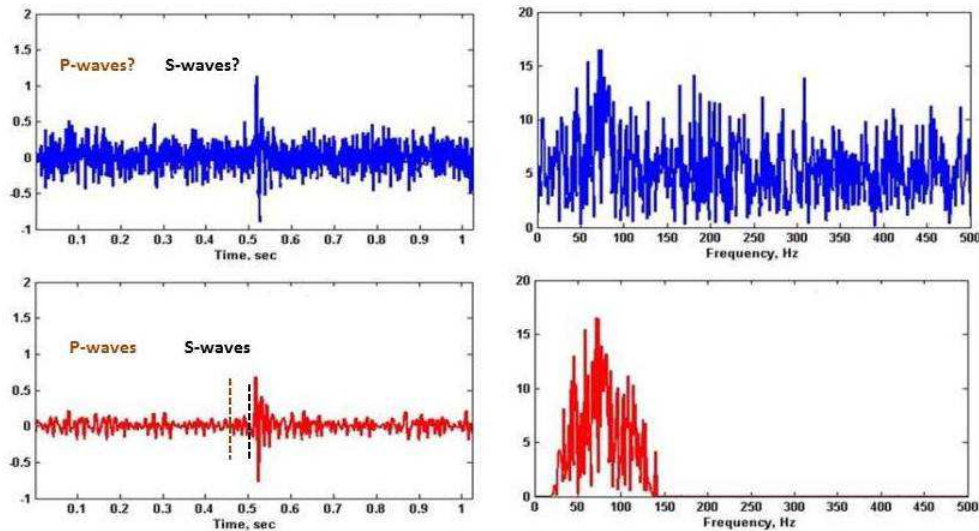


Figure 2.2: Bandpass filtering to reduce random noise. The blue plots show a raw seismic trace and its amplitude spectrum at a SNR=3. The red plots are the results after applying the Ormsby filter. After filtering the arrivals are clearer to identify. Modified from Han [2010].

2.3 Event detection

The primary goal in basic microseismic processing workflow is event location. In order to determine highly accurate locations, accurate time picks of P- and S-wave arrival times is crucial. For large data sets, identifying events in an automated process is required. The most common technique, used in this thesis, is the *STA/LTA* (short-term average versus long-term average) method [Allen, 1978]. This *STA/LTA* filter acts over a characteristic function (CF), in this case, the data point value is used. Allen [1978] also used a CF that uses the time derivative of the seismic trace, giving weights based on SNR.

In this methodology, both a long and short time window are chosen and are moved along the seismic trace one sample at a time and their ratio is computed (Figure 2.3). When both windows encompass background noise, their ratio will be close to 1. When a high-frequency impulse arrives, the *STA/LTA* ratio is boosted, which indicates the possible presence of a microseismic event (Figure 2.4). The equations used in this method are:

$$STA_i = \frac{1}{l_1} \sum_{j_1=i-l_1}^i CF(j_1), \quad (2.1)$$

$$LTA_i = \frac{1}{l_2} \sum_{j_2=i-l_2}^i CF(j_2), \quad (2.2)$$

$$RATIO_{STA/LTA}(i) = \frac{STA_i}{LTA_i}. \quad (2.3)$$

Where l_1 and l_2 are the lengths of the short and long time window. STA_i and LTA_i and $RATIO_{STA/LTA}(i)$ are the short-term average, long-term average and ratio for the i th test point, respectively. Then, the i th index with the highest increase in the $RATIO_{STA/LTA}(i)$ function is chosen as the most probable onset time for that event. When $0 < i \leq l_1$ and $0 < i \leq l_2$, j_1 and j_2 are negatives, so to the STA and LTA functions must be added l_1 and l_2 null data points at the beginning.

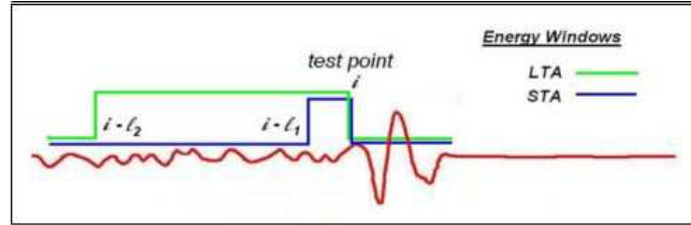


Figure 2.3: Illustration of STA/LTA method. Note the STA time window is positioned at the end of the LTA time window with overlap. Modified from Han [2010].

The STA and LTA window sizes (l_1 and l_2) should be more than a few periods of the recorded microseismic signal and noise, respectively [Akram and Eaton, 2012]. If the STA window is too short, it will likely produce meaningless fluctuations in the STA/LTA values that do not correspond to real microseismic events. A long STA window might not be sensitive to the sudden increase of amplitude in the trace. A very long LTA window results in the obscuring of weak arrivals following the strong microseismic arrivals [Earle and Shearer, 1994]. Wong et al. [2009] recommends the STA window size to be 2-3 times the dominant period of the seismic signal and LTA window size to be 5-10 times longer than STA window size. The threshold for event detection is another important parameter in this stage. It can be dynamic or kept constant for the whole data set. A constant value is usually used, although it is not recommended for recording with varying SNRs. In either case, it should be higher than noise fluctuations and lower than the expected amplitude signal. Another

approach is to establish a threshold that is dependent on the noise level. The *STA/LTA* method is appropriate when microseismic energy is high, but it may fail to detect weak events, which are usually obscured by the background noise.

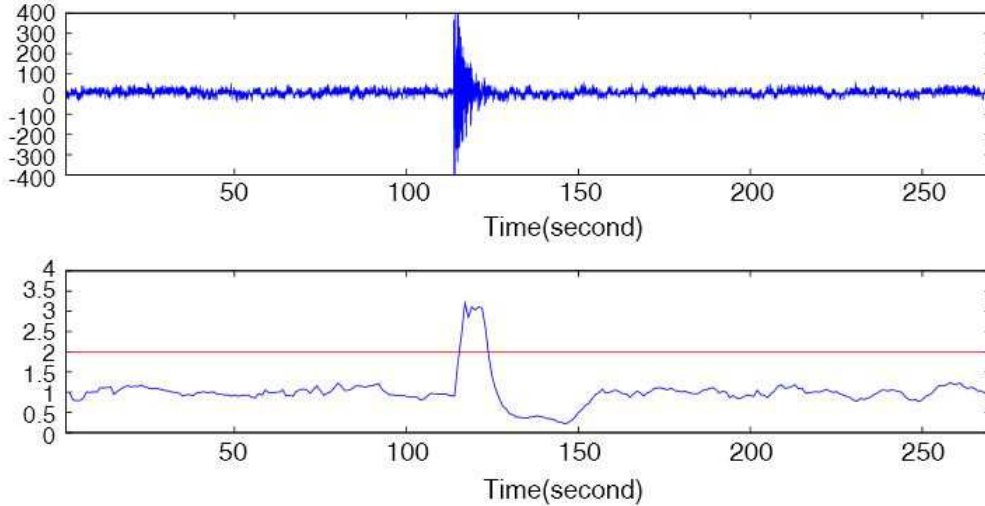


Figure 2.4: Example of *STA/LTA* event detection algorithm. Top: synthetic seismogram containing one event. Bottom: *STA/LTA* ratio curve. The red line denotes the event triggering threshold=2

Another automatic picking methodology, although not used in this thesis, is the modified energy ratio (*MER*) [Wong et al., 2009]. They are based on:

$$RATIO_{MER}(i) = \frac{\sum_{j=i}^{i+L} CF(j)^2}{\sum_{j=i}^{i-L} CF(j)^2}, \quad (2.4)$$

where $RATIO_{MER}(i)$ is the value of the *MER* function in the i th test point, $CF(j)$ is the data point value of the seismogram at time index j , and L is the length of the collecting window preceding and trailing the test point (Figure 2.5). In this case, the peak of the *MER* function ($RATIO_{MER}(i)$) is very close to the onset time of the arrival. Thus, the main difference between the *STA/LTA* and the *MER* method is that the former is performed over windows that precede the sample tested, whereas the latter combines windows that precede and trail the test point. According to Wong et al. [2009], in noise-free seismograms, both methods yield similar results, but the *MER* is more consistent on noisy microseismic traces.

For the purposes of event detection, in this thesis the *STA/LTA* method is used.

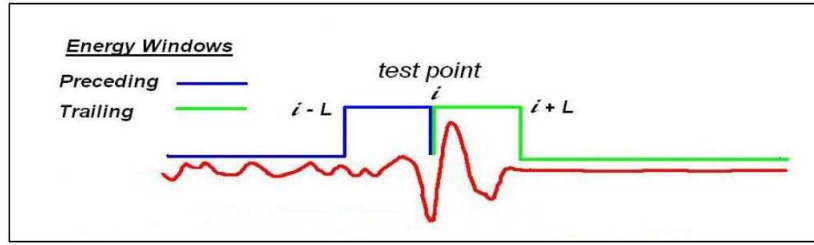


Figure 2.5: Illustration of the *MER* method. Note the *STA* time window is followed by the *LTA* time window with no overlap. Modified from Han [2010].

2.4 Arrival time picking

In the previous section it is mentioned that methods such as *STA/LTA* and *MER* allow to detect microseismic events. In noise-free seismograms and using a sufficiently short *STA* window, they could detect the arrival onset accurately. However, in real data, background noise and the common *STA* windows do not provide accurate time picks. As a result, after the microseismic event has been detected, a more specific time pick should be defined. Manual picking is extremely time consuming and subjective, as different experienced microseismologists might pick onsets at different times, either before or after the true onset arrival. This is because seismic signals have unknown shape and are usually affected by noise. Several additional techniques exist for detecting and picking the arrivals in one- and three-component data. Current methods include energy analysis, polarization analysis and autoregressive techniques [Vidale, 1986, Earle and Shearer, 1994, Sleeman and van Eck, 1999]. Autoregressive techniques are based on the assumption that a time series (a seismogram) can be divided into autoregressive (AR) processes with the intervals before and after the onset as two different stationary segments [Sleeman and van Eck, 1999]. In this thesis, the methodology developed by [Sleeman and van Eck, 1999], based on a criterion named the autoregressive Akaike Information criteria (AR-AIC), is used to pick P-wave arrivals.

In each segment $i = 1, 2$, the one preceding and the one including the phase onset, a model window is defined in which the data are fitted to an autoregressive model of order M with coefficients $a_m^i (m = 1, \dots, M)$:

$$x_t = \sum_{m=1}^M a_m^i x_{t-m} + e_t^i, \quad (2.5)$$

with $t = 1, \dots, M$ for interval 1 and $t = N - M + 1, \dots, N$ for interval 2. The model assumes a non-deterministic part e_t^i being the noise, which is assumed to be Gaussian, with zero mean

and variance σ_i^2 , which is uncorrelated with the deterministic part (source waveforms). The maximum of the logarithmic likelihood function for the two models as function of the K th sample point becomes:

$$AIC(K) = -2 \left[\frac{1}{2}(K - M)\log(\sigma_{1,max}^2) - \frac{1}{2}(N - M - K)\log(\sigma_{2,max}^2) + C_1 \right] + 2P, \quad (2.6)$$

where C_1 is a constant and P is the number of independently estimated parameters and equals the AR order M in the model. This expression is the core of AIC [Sleeman and van Eck, 1999]. For more details, we refer to Sleeman and van Eck [1999]. Figure 2.6 exemplifies this technique where it clearly differentiates between background noise and waveforms, based on their uncorrelated statistical properties.

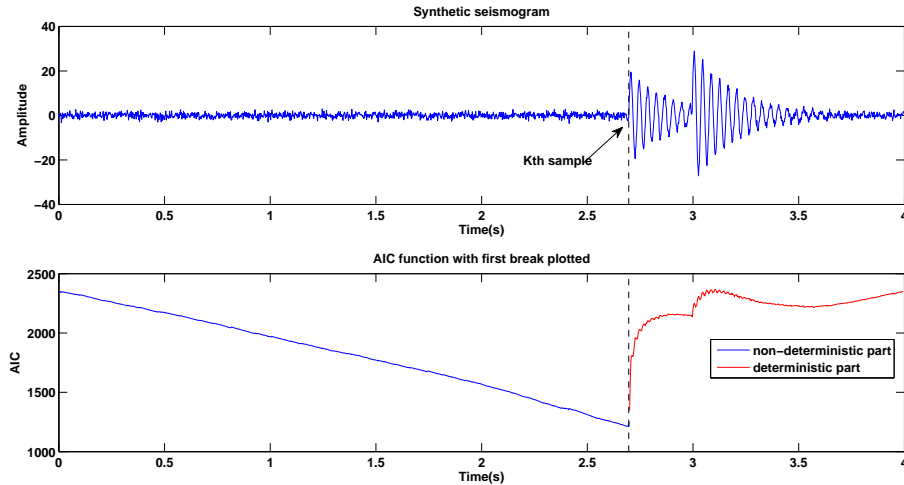


Figure 2.6: Top: A synthetic seismogram showing a microseismic event. The separation point K delimits two adjacent time series with different statistical properties. From sample 1 to K , the time series is random noise. From sample $K+1$ to the last sample, the time series shows source waveforms. The added background noise in this synthetic seismogram is less than typical noise levels in microseismic data. Bottom: AIC function that shows the non-deterministic (noise) and deterministic part (source waveforms).

2.5 Velocity model building

An accurate and geologically relevant velocity model is critical for computing reliable microseismic event locations. As previously stated, an erroneous velocity model represents one

of the sources of uncertainty. In most cases, the velocity model is constructed using well logs (Figure 2.7). The issue is that these logs measure vertical seismic velocities whereas microseismic events recorded in boreholes propagate predominantly horizontally, so velocity models based on well logs are less sensitive to horizontal velocity variations. Moreover, in hydraulic fracturing stimulations these velocity measurements are usually run open-hole and may be perturbed by stress concentrations induced by drilling the well, mud invasion, pore-pressure changes and other drilling-induced damage or changes [Warpinski et al., 2003]. In cases of oil production, if the reservoir has been produced since the log was run, the depletion-induced pressure drop may alter the velocities. Even more importantly, this measurement represents localized measurements which may not be indicative of velocity changes away from the well. As a result, the velocity model needs to be updated to account for these effects. One solution for calibrating velocities is to use arrival times of perforation shots, where receiver locations, perforation or string locations and arrival times are assumed to be known. Then, a velocity inversion is done to calibrate the current velocity model as part of a velocity building workflow (Figure 2.8).

Some papers have shown how to estimate velocity models using perforation data. For instance, Block et al. [1994] describe a joint hypocenter velocity inversion and obtain a solution for a 3-D velocity model for S-waves in a fractured zone of a hydraulic fracturing stimulation. Warpinski et al. [2003] uses a least squares velocity inversion using perforation shots and with known origin time. To evaluate the accuracy in the velocity model, it is necessary to review errors in the locations of perforation shots against signal quality. Large errors in perforation locations are direct indications of errors in the implemented velocity model. Unfortunately, accurate perforation shot locations does not always assure an appropriate velocity model for all arrivals due to the large variety in raypaths.

Figure 2.9 shows an example of artifacts in the fracture mapping due to errors in the velocity profile. Inspection of event patterns identified apparent processing artifacts, i.e. a high number of events located above the target zone and isolated from the in-zone events. The velocity structure in this example was far more complex than initially anticipated, due to different degrees of anisotropy. Correcting the velocity model removed the processing artifacts, thus obtaining more reliable event locations.

In the next chapter the event location methods are discussed.

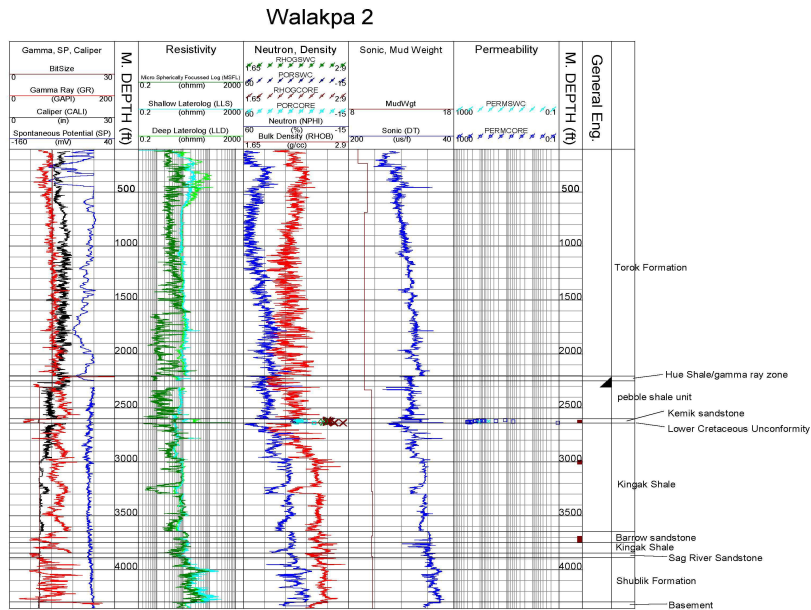


Figure 2.7: Common sonic log (fourth log) in microseismic monitoring. Taken from <http://www.energy.cr.usgs.gov/OF00-200/wells/walakpa2/las/wa2log.jpg> .

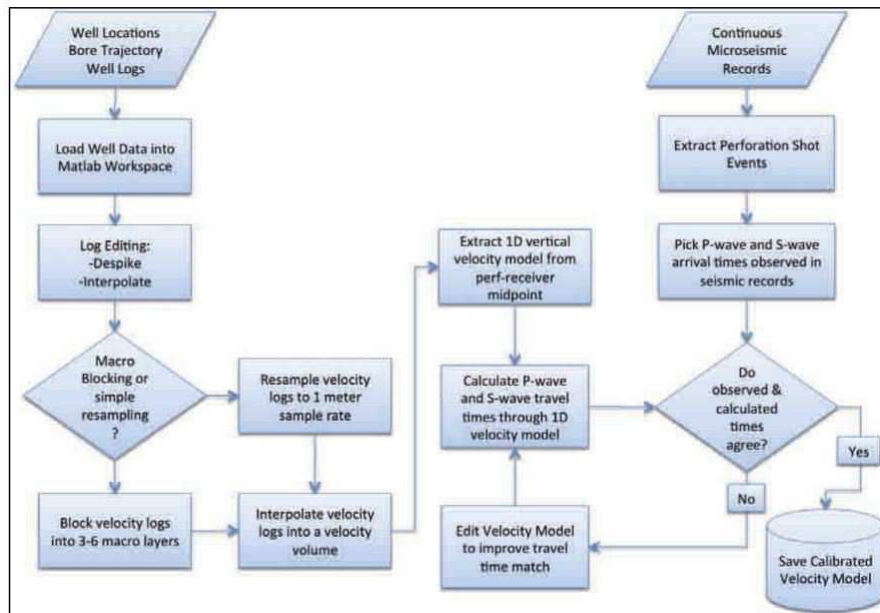


Figure 2.8: Conventional workflow for velocity model building. Taken from Pike and Eaton [2012] .

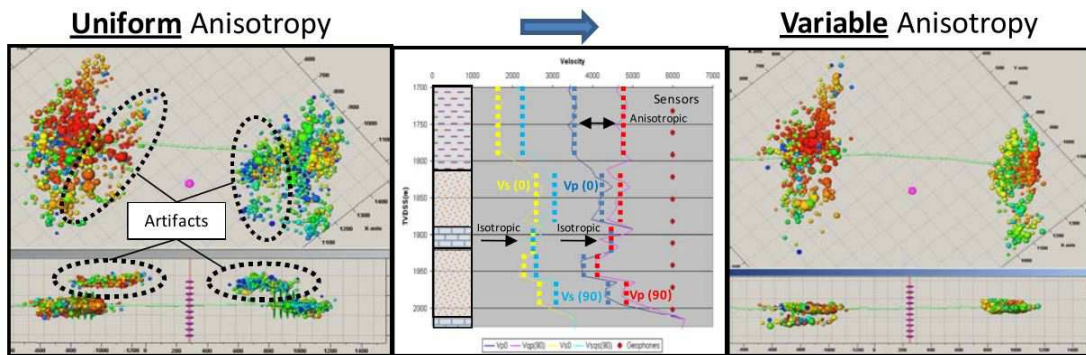


Figure 2.9: Artifacts due to erroneous velocity model. Perforations were accurately located with uniform anisotropy in all layers, but clear artifacts were present in the event patterns (left graph). Reviewing the lithology revealed a wide variation in anisotropy in the velocity model, with an isotropic carbonate, highly anisotropic shale, and moderately anisotropic tight sand. Using the correct velocity structure (center graph) removed the artifacts and resulted in more reliable event locations (right graph). Modified from Jones and Parker [2010].

CHAPTER 3

Location techniques in microseismic monitoring: Theory.

3.1 Introduction

Microseismic event locations can be considered the basics of microseismic monitoring. Common location methods range from linearized to probabilistic techniques, using direct-searches, single event locations, or joint event locations, or from absolute to relative locations. Each technique relies on specific assumptions and has certain advantages and disadvantages, so it is important to understand the scenario of the specific microseismic data, type of data, phases available, receiver array, complexity of velocity structure and computer resources so the optimal location technique is chosen. When we deal with real data, they may be affected by random and systematic errors, as well as possible artifacts, due to, for example, an erroneous velocity model. Thus, it is very important to be able to quantify location uncertainties and identify biases which can complicate subsequent interpretations of the final microseismic locations.

3.2 Direct-Search Methods

From earthquake seismology, we have learned that the location of an earthquake can be found by comparing the observed travel time (with its specific errors) versus the theoretical travel time (predicted assuming a velocity model). The goal is to determine the hypocentral parameters (three spatial coordinates and origin time). A common method to determine event locations is to perform a grid search approach. It consists of generating a grid of possible hypocenters, calculating theoretical travel times from each node to the receiver and then comparing these with the actual observed arrival times. In other words, the

forward model is solved using loops over possible origin times and hypocenters. This yields maximum likelihood estimates of the hypocentral parameters. For receivers distributed in several boreholes, a good azimuthal coverage is obtained, thus, hypocenters can be well resolved using a single phase (assuming a velocity model) with the following equation:

$$\rho_D(t_{obs}) = \exp\left(-\sum_{k=1}^{nsta} \left\{ (t_{obs}^k - t_{cal}^k - t_o)^2 / (2\sigma_t^2) \right\}\right), \quad (3.1)$$

equation 3.1 is used in this thesis to determine initial event locations. t_{obs} is the observed arrival time for a single phase (P- or S-wave), t_{cal} are the corresponding theoretical travel times, t_o is the origin time, $nsta$ is the number of receivers, σ_t is the time pick uncertainty and $\rho_D(t_{obs})$ the probability density of hypocenter location. Though not normalized, equation 3.1 is sufficient to provide a relative probability density of any location, being the best estimate of the event location given the available data measurements. In microseismic monitoring, the receiver distribution is usually restricted, such as in a single vertical borehole. In that case, not only the distance but also the azimuth is needed to determine the locations accurately [Pearson, 1981, Fischer et al., 2008]. After adding the backazimuth observations to equation 3.1, it becomes:

$$\begin{aligned} \rho_D(t_{obs}, Az_{obs}) = & \exp\left[-\sum_{k=1}^{nsta} (tp_{obs}^k - tp_{cal}^k - t_o)^2 / 2\sigma_p^2\right] \times \\ & \exp\left[-\sum_{k=1}^{nsta} (ts_{obs}^k - ts_{cal}^k - t_o)^2 / 2\sigma_s^2\right] \times \\ & \exp\left[-\sum_{k=1}^{nsta} w(\sin(Az_{obs}^k) - \sin(Az_{cal}^k))^2 / 2\sigma_{Az}^2\right]. \end{aligned} \quad (3.2)$$

Where tp_{obs} , ts_{obs} and Az_{obs} are the observed arrival times of P- and S-waves and backazimuth, respectively, whereas tp_{cal} , ts_{cal} and Az_{cal} are the theoretical travel time of P- and S-waves and backazimuth, respectively. σ_p , σ_s and σ_{Az} are the standard deviations of P-, S-waves travel times and backazimuth, respectively. w is a trade-off factor. Summation of equation 3.2 are done over all receivers where P- and S-waves arrival times and backazimuth information is available. Given that the grid is defined using a binning of ΔX , ΔY , ΔZ and a set of origin times spaced ΔT , equation 3.2 is evaluated at each node of the grid for all possible origin times T_o , thus having a final probability for hypocenter location at each node. The most likely hypocenter location is the node with the highest probability density. The uncertainties σ_p , σ_s and σ_{Az} represent a measure of the quality of the data; smaller values indicating more focalized event locations. These parameters need to be carefully chosen as they should be truly linked to the quality of the measurement. For instance, the SNR is a common measure of the quality of the time picks. Eisner et al. [2010] suggest that the

standard deviation of an observed arrival time can be related to the maximum frequency in the observed waveforms, as long as noise levels are constant among all arrivals. At this point it is assumed that data errors are independent, identically distributed normal variables.

Equation 3.2 is based on least squares, which tends to give the optimal answer when the misfit between theoretical and observed values are caused by non-correlated Gaussian noise. However, data errors can be interdependent. For example, if the time window chosen for polarization analysis is based on the automatic picker, any bias in an onset or maximum amplitude detection can affect the angle measurements. In addition, there might be instrument-related issues during the acquisition that could affect both observed arrival times and backazimuths. If data errors are correlated, Tarantola and Valette [1982] suggest that probability functions need to be calculated using covariances, which was not done here since it is difficult to establish systematic correlations. If errors are non Gaussian, least squares can give too much importance to outliers. Then, the sum of the differences can be used:

$$\begin{aligned} \rho_D(t_{obs}, Az_{obs}) = & \exp\left[-\sum_{k=1}^{nsta} |tp_{obs}^k - tp_{cal}^k - t_o| / 2\sigma_p^2\right] \times \\ & \exp\left[-\sum_{k=1}^{nsta} |ts_{obs}^k - ts_{cal}^k - t_o| / 2\sigma_s^2\right] \times \\ & \exp\left[-\sum_{k=1}^{nsta} |\sin(Az_{obs}^k) - \sin(Az_{cal}^k)| / 2\sigma_{Az}^2\right]. \end{aligned} \quad (3.3)$$

Using equation 3.3 is based on the *L1 norm* misfit calculation. This is considered more robust than the *L2 norm* (least squares from equation 3.2). Another approach to reduce the effect of outliers when applying the *L2 norm* could be to use an iterative process where outliers are downweighted with number of iterations [Waldhauser and Ellsworth, 2000].

If infinite computer resources were available, a straightforward solution would be to define a very small spacing ΔX , ΔY , ΔZ , and ΔT , such that the most likely hypocenter location with the highest resolution is obtained. Unfortunately, that is not possible, so a method to speed up the computing processing times is required. A way to save computing time is by designing a lookup table where all theoretical travel times and backazimuths are previously stored for each node in the 3-D grid (see Figure 3.1). With this, repeated calculations of theoretical variables in the same node are avoided. Another option to speed up processing times is to do a lower resolution search first using a larger spacing followed by a second search within the most likely coarser grid block using a smaller spacing. This is based on the neighborhood algorithm [Sambridge, 1998] and can considerably reduce computing times.

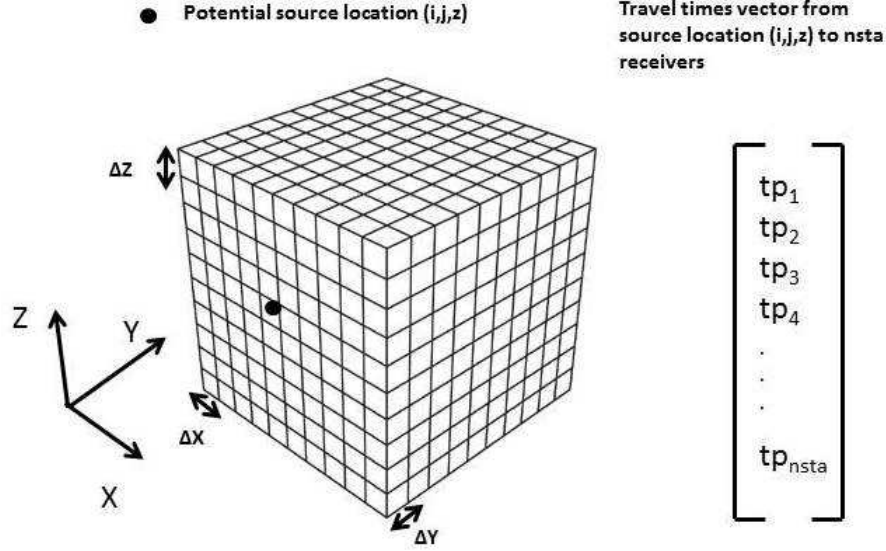


Figure 3.1: Illustration of lookup table where theoretical travel times corresponding to $nsta$ receivers are stored for each potential source location (node) in the 3-D grid. The spacing is defined as ΔX , ΔY and ΔZ . Since the origin time is linearly related to the observed arrival time, an outer loop with a spacing of ΔT is done to obtain the best origin time t_o .

3.3 Linearized Methods

3.3.1 Single Event technique

In the previous section it is stated that microseismic event location could be determined by searching over all possible source locations within a three dimensional space. However, it uses large computation times for smaller data volumes, so another approach is to use a quicker method for individual events that linearizes this inverse problem [Shearer, 1999, Stein and Wysession, 2003]. The first step is to estimate an initial guess of the hypocentral parameters $\mathbf{m}_o = (\mathbf{X}_o, \mathbf{Y}_o, \mathbf{Z}_o, \mathbf{T}_o)$. To linearize the problem, it is assumed that initial locations are close to the true hypocenter location, so it considers small perturbations to a target hypocenter $\mathbf{m} = \mathbf{m}_o + \Delta\mathbf{m}$. Here \mathbf{m}_o is the initial guess and \mathbf{m} is the new location so that the travel time residual evaluated at the initial guess is linear with respect to the correction needed in the hypocentral parameters. In other words:

$$t_i(\mathbf{m}) - t_i(\mathbf{m}_o) = \frac{\partial t_i}{\partial m_j} \Delta m_j, \quad (3.4)$$

where $t_i(\mathbf{m})$ is the observed arrival time for the i th receiver, $t_i(\mathbf{m}_o)$ the theoretical travel time assuming a velocity model and $\frac{\partial t_i}{\partial m_j}$ is the partial derivative of the i th travel time with respect to the four hypocentral parameters evaluated at \mathbf{m}_o . The residuals at the new location \mathbf{m} are:

$$\begin{aligned} r_i(\mathbf{m}) &= t_i - t_i(\mathbf{m}), \\ r_i(\mathbf{m}) &= t_i - t_i(\mathbf{m}_o) - \frac{\partial t_i}{\partial m_j} \Delta m_j, \\ r_i(\mathbf{m}) &= r_i(\mathbf{m}_o) - \frac{\partial t_i}{\partial m_j} \Delta m_j. \end{aligned} \quad (3.5)$$

The condition to minimize these residuals is:

$$r_i(\mathbf{m}_o) = \frac{\partial t_i}{\partial m_j} \Delta m_j. \quad (3.6)$$

Since arrival times are picked at several receivers, a system of equations is built:

$$\mathbf{r}(\mathbf{m}_o) = \mathbf{G} \Delta \mathbf{m}, \quad (3.7)$$

where \mathbf{r} is the residual vector, \mathbf{G} contains the partial derivatives $G_{ij} = \frac{\partial t_i}{\partial m_j}$, $i = 1, 2, \dots, nsta$, $j = 1, \dots, 4$. and $\Delta \mathbf{m} = (\Delta X, \Delta Y, \Delta Z, \Delta T)$ is the solution vector. Equation 3.7 can be solved using a technique based on least squares to determine the perturbation vector $\Delta \mathbf{m}$. Then, $\mathbf{m} = \mathbf{m}_o + \Delta \mathbf{m}$ is updated and the process is repeated until the location converges or a stopping criteria is reached.

Equation 3.6 uses travel times only. If the receiver distribution does not allow for a good azimuthal coverage, backazimuth measurements can also be incorporated into the system of equations 3.7:

$$r_i(\mathbf{m}_o) = \frac{\partial \varphi_i(m - m_o)}{\partial m_j} \Delta m_j. \quad (3.8)$$

This procedure is usually called the single event technique and can sometimes be used after a directed-search approach to find true location. An inconvenience is that this method retrieves accurate hypocenter locations if the problem is well constrained. However, if the problem is ill-conditioned, this method is likely to fail. For instance, when the probability density function (pdf) is irregular, due to complex structures or data outliers, linearized methods may converge to a local maximum, compared to a grid search, which is able to

assess the complete location pdf and find the maximum likelihood hypocenter [Lomax et al., 2008]. An alternative option is to use non-linearized methods which can also provide more reliable locations when the system is ill-conditioned [Scarfì et al., 2005].

3.3.2 Master Event technique

Relative locations between events can be determined with much greater accuracy than absolute locations of individual events [Poupinet et al., 1984, Fremont and Malone, 1987, Deichmann and Garcia-Fernandez, 1992, Got et al., 1994, Waldhauser and Ellsworth, 2000]. This occurs because velocity heterogeneities outside of the source region often lead to uncertainties in the observed travel times for each event, especially at distant stations. By applying a Master event approach, travel time measurements for two collocated events will be affected similarly by these heterogeneities, so their impact will be canceled out. In this technique, one event is designated as the master event, and then arrival times of other events are computed relative to the master event times:

$$t^{rel} = t^{slave} - t^{master}, \quad (3.9)$$

and the master event location can be set to \mathbf{m}_o . Then, the relative location $\Delta\mathbf{m}$ is given as the best fitting solution

$$t_i^{rel} = t_i(\mathbf{m}) - t_i(\mathbf{m}_o) = \frac{\partial t_i(m - m_o)}{\partial m_j} \Delta m_j. \quad (3.10)$$

Again, for the solution to be valid, the perturbations have to be small enough so that the linear approximation is held. An advantage of this technique is that if the absolute location of the master event is known accurately, then the relative locations of the slave events can be converted to absolute locations.

This approach has been used widely, especially when families of repeating earthquakes called doublets are found [Poupinet et al., 1984, Fremont and Malone, 1987]. Since the doublet definition assumes that these events are collocated, their path effects will cancel out. For instance, Agh et al. [2012] used a similar technique to relocate slave events relative to master events by stacking of crosscorrelation along differential moveouts. A master event generally should have a high SNR and strong energy. Arrowsmith and Eisner [2006] developed an automated scheme where waveforms corresponding to the current event are compared with a library of master events to determine if that event is a doublet or a new master event, assigning the event to the corresponding multiplet group or setting it in the library as a new master event. A main advantage of relative location methods is that more accurate arrival time differences can be achieved through crosscorrelation [Poupinet et al., 1984,

Slunga et al., 1995, Waldhauser and Ellsworth, 2000]. Since similar events often occur very close to each other, their waveforms will have a relative time difference which is proportional to their separation offset. This time difference can be calculated taking the lag that corresponds to the maximum peak of the crosscorrelation function.

3.3.3 Double-Difference technique

This is a relative location technique initially developed for earthquake seismology and is gaining popularity in microseismic analysis [Waldhauser and Ellsworth, 2000]. In this thesis, a method based on this technique is implemented for multiplet relocation. The theory is described in detail in chapter 4.

3.3.4 Other techniques

There have been several techniques developed for MS monitoring, some of them being more suitable for certain source-receiver geometries and model complexities. For instance, for the case of surface monitoring, migration-based approaches have been used, which involve downward continuation by beamforming, followed by event detection and event localization. Beamforming is done by a search of potential source locations in the subsurface. For each node, the data recorded across the array are summed along diffraction curves, forming a beamformed trace, which is a continuous estimate of the potential source history at the subsurface over the course of the recording. Chambers et al. [2010] presented another example of location technique based on migration. This procedure basically consists of computing a semblance trace for each image point and origin time, using the following equation:

$$S(x, \tau) = \frac{\left[\sum_{i=1}^{i=N} u_i(t = T_i(x) + \tau) \right]^2}{\sum_{i=1}^{i=N} [u_i(t = T_i(x) + \tau)]^2}. \quad (3.11)$$

Here $u_i(t)$ is the preprocessed trace for receiver i , $T_i(x)$ is the P-wave travel time from the image point to the receiver and $nsta$ the number of stations. Then, S is smoothed, and the maximum value at each image point is taken, reducing the results to a 3-D data cube.

Time-reversal imaging techniques have also been used. It consists of propagating a wavefield through a velocity model after reversing the time axis, i.e. time-reversed data are injected into the model domain as sources at recording stations and propagation causes events to focus at the source location [Artman et al., 2010].

3.4 Synthetic Example

Synthetic examples are done to test different aspects of the grid search algorithm for absolute event location. First, the effect of the implementation of a lookup-table is assessed when using two common velocity models (1-D isotropic velocity model and an homogeneous velocity model). Then, the effects of the main sources uncertainty aforementioned, namely, time picking errors, poor source-receiver array and an erroneous velocity model are shown.

3.4.1 Lookup-table

To assess the influence of a lookup-table, the event location algorithm is run to locate one single event for several bin sizes as well as different velocity models (1-D isotropic velocity model and constant layering) and the processing times are computed. The results are shown in Table 3.1. Note that when using a 1-D layered velocity model and no lookup-table is implemented, the computing time is significantly longer (approximately 80 and 230 times longer when using a binning space of 100 and 20 m, respectively). Consequently, these differences in time will be more pronounced with smaller binning spacing. On the other hand, when using a homogeneous velocity model, the effect of using a lookup-table does not reduce the computing times; in fact, the performance time increases (Table 3.1). This indicates the advantage of including such table when theoretical travel times are computed by time consuming algorithms such as a ray tracer. These results from Table 3.1 are plotted in Figure 3.2.

Bin size (m)	1-D vel.model		Constant vel.model	
	lookup table (s)	no lookuptable (s)	lookuptable (s)	no lookuptable (s)
20	14.2	3260.7	14.88	7.36
25	7.3	1724.8	7.61	3.72
30	4.4	977.5	4.46	2.37
35	2.97	640.6	3.01	1.56
40	2.13	437	2.15	1.23
45	1.62	312.4	1.67	0.93
50	1.37	248.6	1.35	0.84
55	0.99	161.46	1.01	0.62
60	0.89	144.53	0.99	0.64
80	0.62	60.16	0.59	0.47
100	0.53	40.63	0.56	0.42

Table 3.1: This table shows the effect of using a lookup-table during the grid search performance. Note the computing times are significantly reduced when theoretical travel times are computed for a layered 1-D isotropic velocity model.

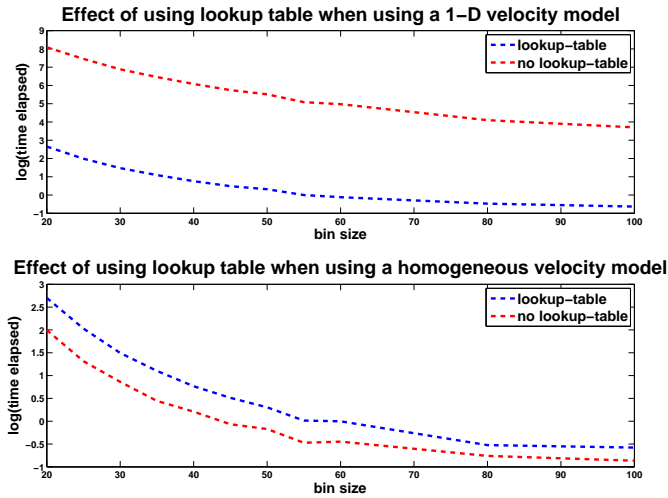


Figure 3.2: Effect of using a lookup-table, using the data from table 3.1. Top: 1-D velocity model. In this case, the implementation of the lookup-table reduces the computing time. Bottom: Homogeneous velocity model. The use of a lookup-table increases the computing time.

3.4.2 Effect of time picking errors

In this test, synthetic travel times are perturbed by different percentages of random time picking errors, in order to simulate errors in arrival time readings when picking waveform onsets, and their corresponding location errors are computed. A multiple borehole receiver array is assumed and half of the receivers are randomly active with time picks available. Figure 3.3 shows the probability density maps when adding Gaussian perturbations of 0, 10 and 20 % to synthetic travel times to simulate time picking errors in real data. As expected, when no perturbation is added to synthetic travel times, the true event location is obtained (top of Figure 3.3), despite that the receiver geometry can bias the output location. However, as the perturbation percentages increase (middle and bottom of Figure 3.3), the source nodes corresponding to the highest probability density do not match the true event location. This can also be observed in Figure 3.4, where the location error as a function of perturbation percentages is displayed. As expected, the higher the time picking error, the more inaccurate the final location in each plane, hence, the importance of measuring arrival times accurately.

In Figure 3.5, the effect of using different σ values (using equation 3.1) is shown. Measurements with higher fidelity provide probability density maps with more focalized solutions, allowing for more accurate microseismic event mapping.

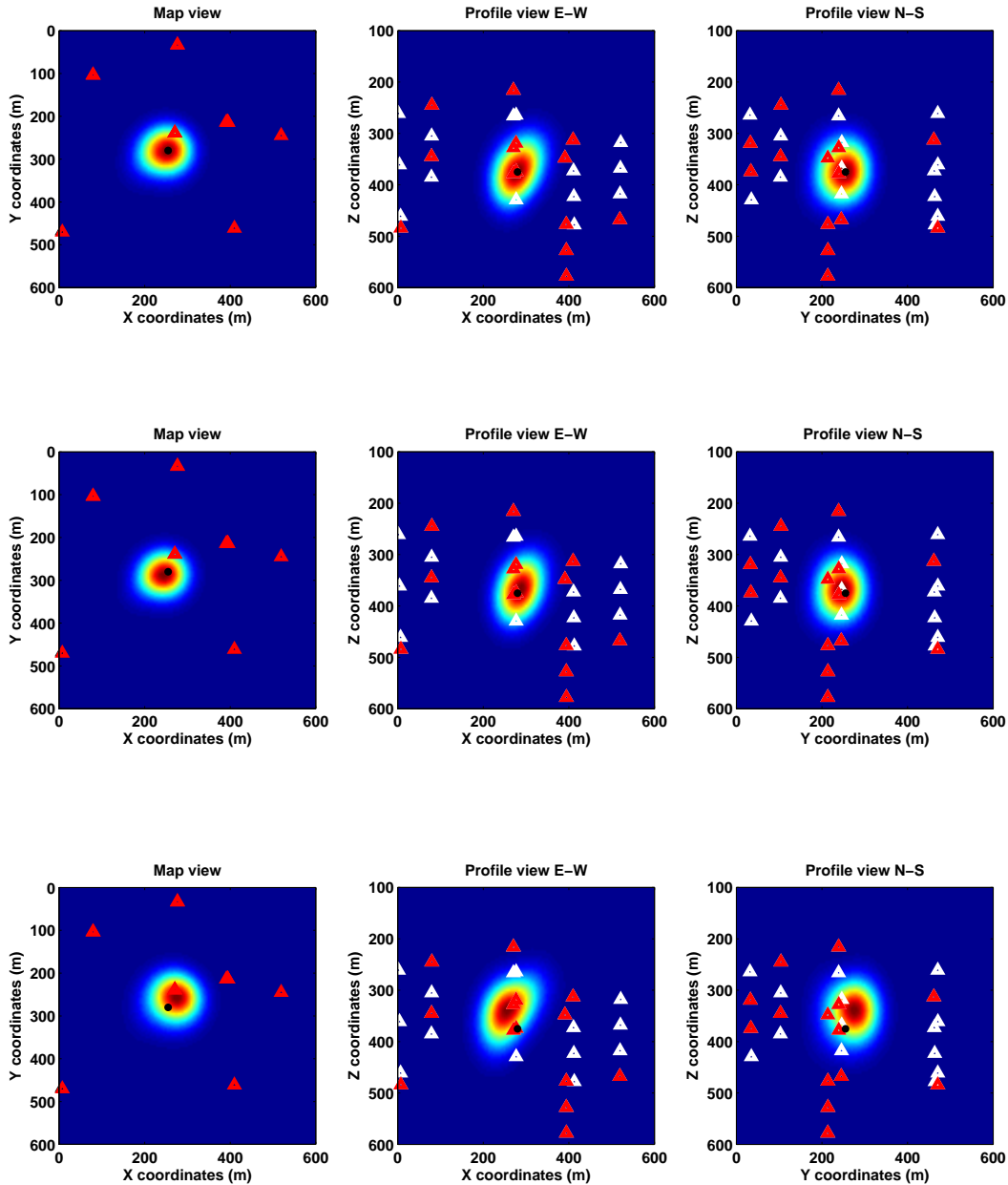


Figure 3.3: Illustration of probability density maps for different percentages of random errors added to synthetic travel times. Top: no errors added. In this case the algorithm obtains the true event location, despite this receiver geometry is not regular. Middle: 10 % errors added. Bottom: 20 % errors added, time picking errors, combined with asymmetric receiver distributions produce errors in final event locations. Red areas: high probability. Blue: low probability. Red Triangles: receivers used. White triangles: receivers skipped. Black solid circle: True event location.

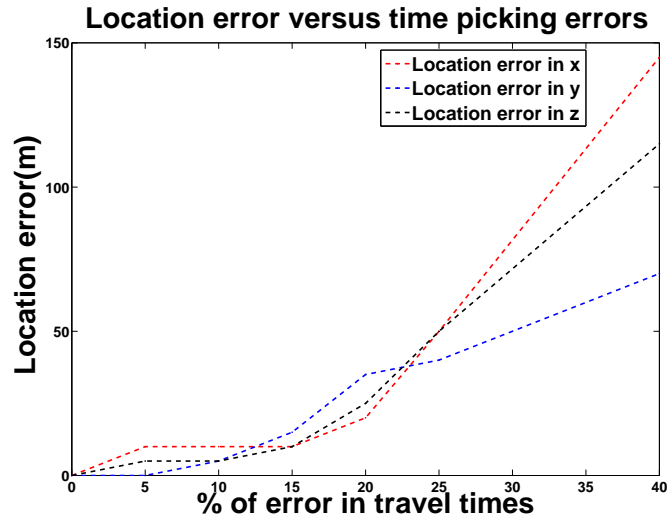


Figure 3.4: Location error as a function of percentage error added to synthetic travel times. As expected, the higher the time perturbation, the higher the location error in each direction.

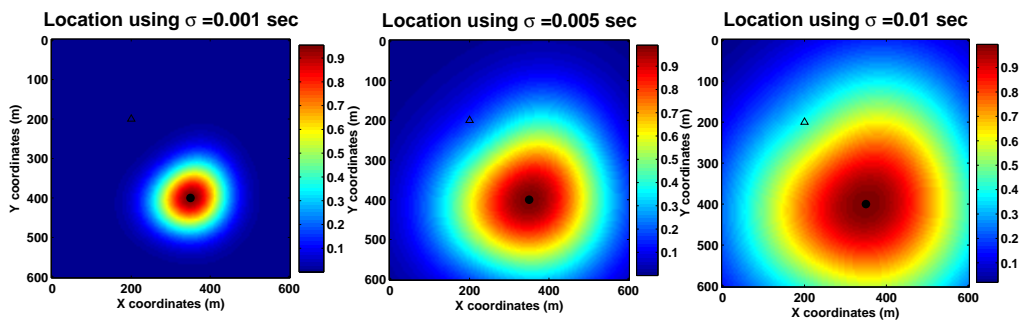


Figure 3.5: Illustration of probability density maps for different σ values. Left: $\sigma=0.001$ sec. Middle: $\sigma=0.005$ sec. Right: $\sigma=0.01$ sec. As σ becomes larger, the image becomes less focalized. Red areas: high probability. Blue: null probability. Black solid circle: true event location.

3.4.3 Effect of velocity model

The chosen velocity model for event location always represents an approximation to the true velocity structure, so it usually produces errors in the predicted travel times. Numerous studies show that velocity errors (such as approximately 5% velocity changes or modest dip perturbations) can cause significant bias and mislocations in microseismic events [Jansky et al., 2010]. This test consists of locating a synthetic microseismic event assuming underestimated, correct and overestimated velocity models in a receiver distribution similar to the real case study. The results are shown in Table 3.2.

Vel. perturb.(%)	ΔX (m)	ΔY (m)	ΔZ (m)
-40	-30	25	30
-30	-25	20	25
-20	-15	10	15
-10	-5	5	5
0	0	0	0
10	5	-5	-5
20	5	-5	-5
30	15	-5	-30
40	65	-15	-140

Table 3.2: This table shows the effect of velocity errors when obtaining event locations. A homogeneous velocity model was used for simplicity

Figure 3.6 shows probability density maps when using a correct, underestimated (-40 %) and overestimated (+40 %) velocity model, respectively. The likelihood distributions are elongated along the depth profile, especially using overestimated velocities, suggesting more ambiguity in constraining the event depth. When using an underestimated velocity model (40 % lower), the area with maximum probability density has been collapsed when compared with the results for the correct velocity profile; nevertheless, its position is biased. These results are best summarized in Figure 3.7. Note that for this receiver configuration, location errors are significantly higher when the velocity is overestimated.

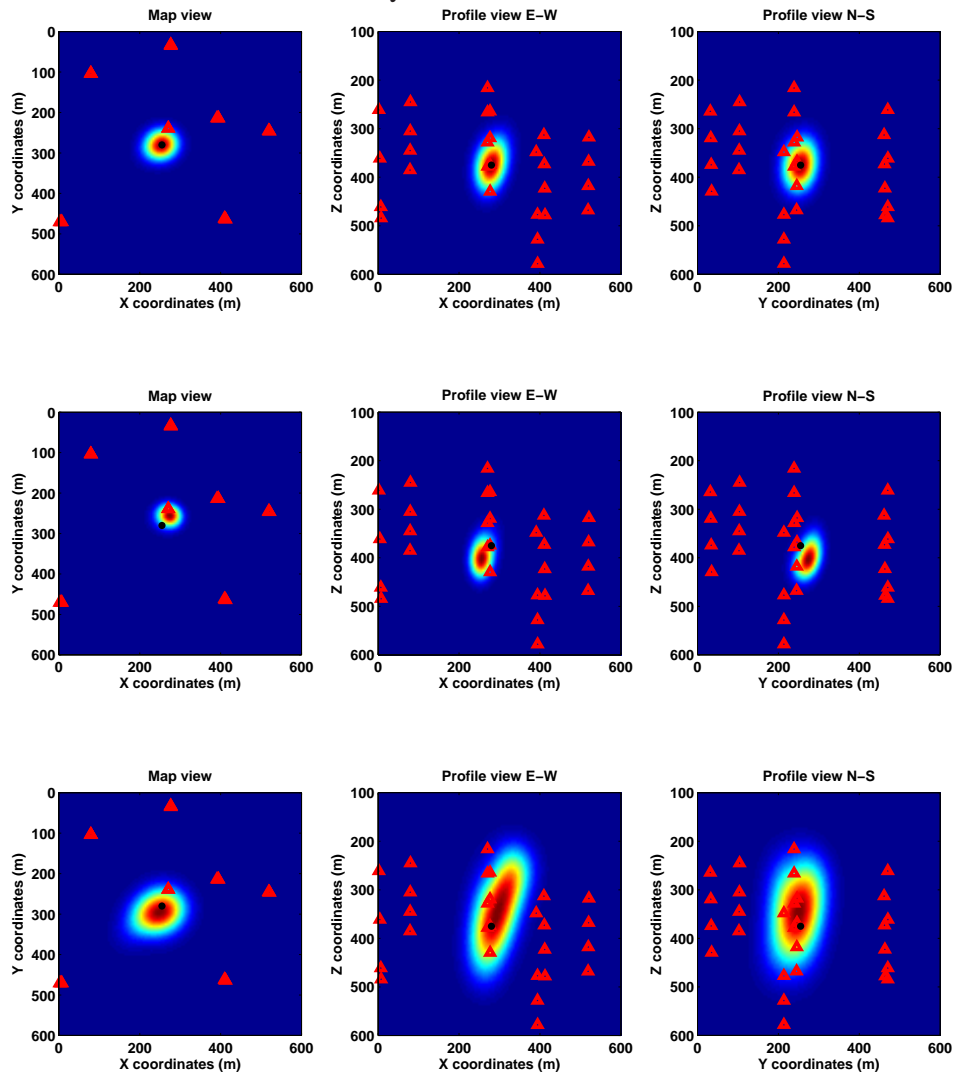


Figure 3.6: Illustration of probability density maps when using correct (top), underestimated (middle) and overestimated (bottom) velocity model. 28 receivers distributed in seven boreholes are used. Red areas: high probability. Blue: null probability. Red triangles: receivers used. White triangles: receivers skipped. Black solid circle: true event location.

3.4.4 Effect of receiver array

In this part, the effect of receiver setup on event locations is shown. Receiver distributions are particularly important when inverting travel times only. Top Figure 3.8 shows that

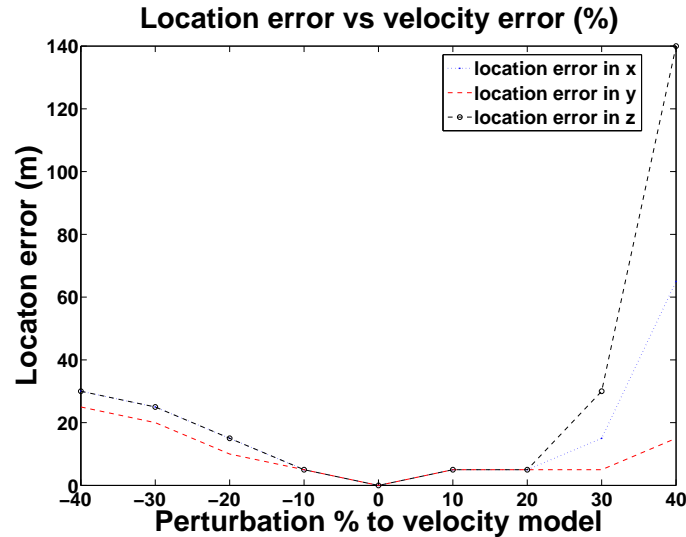


Figure 3.7: Location error as a function of different velocity perturbations. Given this receiver setup, location errors are higher when the velocity model is overestimated.

inverting travel times only when the receiver distribution is poor does not provide correct results, since it mainly constrains the distance. As a result, backazimuths measurements are also included in common microseismic processing workflows with two or less receiver boreholes. On the other hand, when receiver locations provide a good azimuthal coverage, as shown in the middle of Figure 3.8, the event location is well constrained using travel times only despite usage of fewer receivers. If a larger number of receivers surround the event source location, this redundancy contributes to a more focalized image of the event location (bottom of Figure 3.8).

Since the pre-processing workflow is developed and the location technique has been tested, next chapter will describe the theory and synthetic examples for the double-difference relative event location method.

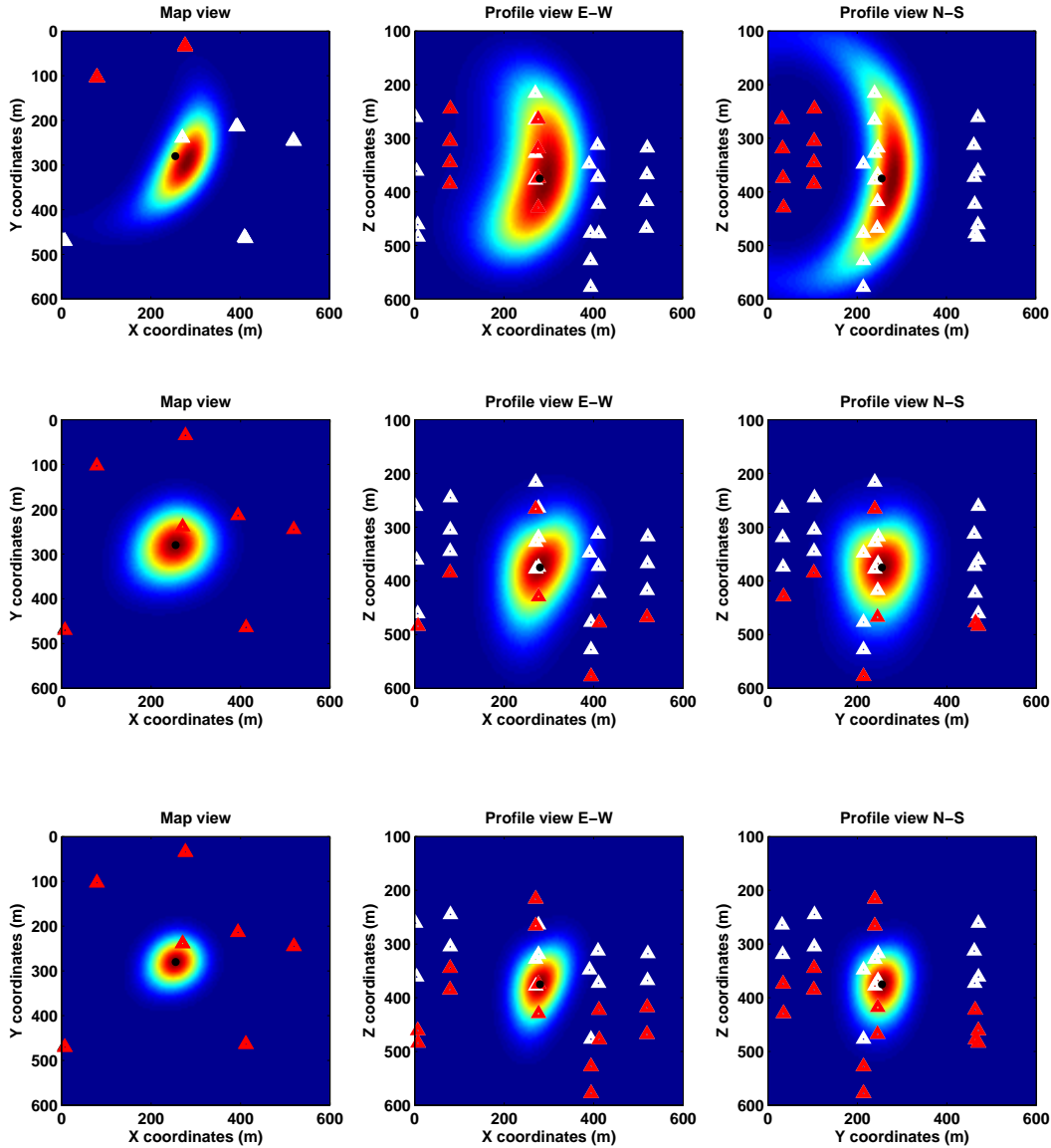


Figure 3.8: Probability density maps when using different numbers and distribution of receivers. Top: A poor receiver setup (eight receivers). In this case, backazimuth and angle of incidence measurements should be used to constrain the event location. Middle: One receiver per borehole (seven receivers). Given the good azimuthal coverage, the obtained event location matches the true event location, despite of using less receivers than in the top Figure. Bottom: Two receivers per borehole (14 receivers). As more receivers are used, the shape of the image is more focalized, compared to middle Figure. Red areas: high probability. Blue: null probability. red Triangles: receivers used. White triangles: receivers skipped. Black dot: true event location.

CHAPTER 4

Multiplets and Double-difference technique: Theory. ¹

4.1 Introduction

As previously stated, accurate hypocenter locations are of paramount importance because they allow for a better understanding of the process under study (e.g., hydraulic fracturing and EOR stimulations, mining and volcano activities). However, three factors add uncertainties in the final locations: i) a poor source-receiver geometry, ii) errors in time picks and iii) errors in the velocity model [Pavlis, 1992]. A 1-D velocity model is commonly used in microseismic projects but it only represents an approximation to the true velocity structure. The impact of unanticipated velocity structures can be reduced by applying relative location methods [Poupinet et al., 1984, Fremont and Malone, 1987, Got et al., 1994]. For that reason, a procedure that combines identification of similar microseismic events and a relocation method based on the double-difference algorithm is introduced in this chapter. Since microseismic events coming from similar locations and source mechanisms show nearly-identical waveforms at common stations, the first technique uses crosscorrelation methods to detect similar events, i.e. doublets, which share a correlation level higher than a certain threshold, as events within a multiplet group are linked in a chain-like fashion. The double-difference method assumes that if the inter-event distance for two events is very small compared to the source-receiver distance, then raypaths are similar for both events, so the relative travel time difference in a common receiver is mainly related to the spatial offset between both events. That is because the velocity heterogeneities for these two events are similar, except in the source region where raypaths may differ. The double-difference technique works better for dense seismic clouds, the reason why multiplet groups are first detected. In addition, a weighting scheme is used to emphasize highly correlated/collocated events, which has a

¹A version of this chapter has been presented ([Castellanos and van der Baan, 2012]).

major impact in the final locations.

This procedure I apply in this thesis has an advantage over the master event approach, another relative location method, because the linking is not only with one master event, but with all event pairs in the multiplet group [Waldhauser and Ellsworth, 2000]. Time picking errors is another source of uncertainty for the final event locations and its effect is usually overlooked. As a result, in this work relative travel time differences between similar events are improved using waveform crosscorrelation methods. To show the performance of the algorithm, it is applied to synthetic data at the end of this chapter.

4.2 Event similarity

4.2.1 Crosscorrelation method

Two microseismic events originating from similar source regions produce similar waveforms at common stations if their separation distance is small. Thus, two similar events, often called doublets, have highly correlated waveforms and multiplets as more than two highly correlated microseismic events [Arrowsmith and Eisner, 2006].

By using an analogy to the convolution theorem, the normalized crosscorrelation can be evaluated in the frequency domain. Consequently, for any two traces $x_1(t)$ and $x_2(t)$, the crosscorrelation function is evaluated as:

$$C_x(\tau_i) = \frac{F_D^{-1}(X_1^*(f)X_2(f))}{\sqrt{\sum x_1^2(t) \sum x_2^2(t)}}, \quad (4.1)$$

where F_D^{-1} is the inverse Fourier transform, $X_1^*(f)$ is the complex conjugate Fourier transform of $x_1(t)$ and $X_2(f)$ the Fourier transform of $x_2(t)$, f is frequency, and t is time. In microseismic data, each receiver usually has three components, so the crosscorrelation value in each component is weighted based on their corresponding maximum amplitudes, assuming they reflect the SNR in each trace:

$$C_{Ri}(\tau_i) = \frac{A_x C_x(\tau_i) + A_y C_y(\tau_i) + A_z C_z(\tau_i)}{A_x + A_y + A_z}, \quad (4.2)$$

where C_x , C_y and C_z , are the crosscorrelation coefficients for each component and A_x , A_y and A_z are the maximum amplitudes for each component, whereas τ is the time lag between both events at the i th receiver. To find the peak crosscorrelation coefficient for all receivers m , the peak crosscorrelation coefficients for each separate receiver are averaged:

$$CC(\tau_i) = \frac{\sum_{i=1}^m C_{Ri}(\tau_i)}{m}. \quad (4.3)$$

The crosscorrelation coefficient depends on the length of the correlation window. To illustrate it better, a synthetic test done by Baisch et al. [2008] is shown in Figure 4.1. It shows that in general, the trend of decreasing crosscorrelation with increasing source separation is most pronounced if the correlation window is large, i.e. including P- and S-wave onsets, and a significant part of the S-wave coda (open circles). When using smaller time windows the correlation values are higher, this occurs because for smaller correlation lengths, it is more likely that some arbitrary wave trains from two different seismograms match almost perfectly. In addition, when using shorter correlation windows (e.g. covering a small portion of the S-wave coda), the crosscorrelation values exhibit more variety, especially at larger separation distances (crosses and triangles). It seems thus more appropriate to select a correlation time window that encompasses both phases, always trying to avoid a very long time window that may include pre or post-event background noise and other arrivals [Baisch et al., 2008].

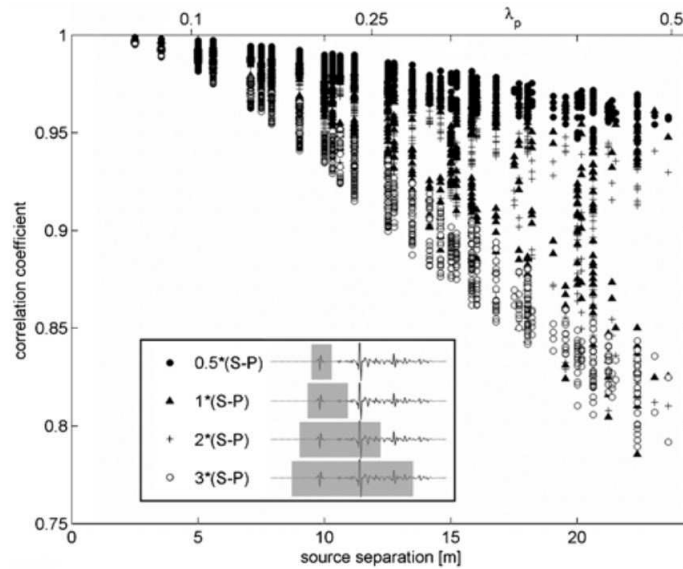


Figure 4.1: Crosscorrelation coefficients at a common receiver as a function of separation distance between synthetic source events spread in a grid (bottom axis) and as multiples of the dominant P-wave length (top axis). Crosscorrelation coefficients have been determined for all possible pairs of hypocenter combinations resulting from the grid. The window length for which the crosscorrelation coefficient has been computed is denoted by the legend and is stated in multiples of the differential time between the S- and P-phase onsets. Time windows are positioned dynamically such that 20% of the total time window length is ahead of the P-phase onset, as illustrated by the gray boxes. Taken from Baisch et al. [2008].

4.2.2 Clustering doublets into multiplets

After calculating the averaged peak crosscorrelation coefficient for all event pairs, an $N \times N$ crosscorrelation upper triangular matrix is generated, where N is the number of events. Once this is done, the crosscorrelation level needs to be defined to consider two events as highly correlated. Noise is always present in real data, so this doublet definition is qualitative, i.e. two events will never be 100 % similar. Several studies have used low values as 0.68 [Moriya et al., 2003, De Meersman et al., 2009], relatively high 0.8 [Arrowsmith and Eisner, 2006] or very high 0.95 [Baisch et al., 2008]. Naturally, the lower the threshold, the higher the number of events considered as similar. The linking between similar events can be done in two ways. First, each event needs to be highly correlated with all other events within the same multiplet group [De Meersman et al., 2009]. Another approach is to allow events to be linked in a chain-like fashion, so they can belong to the same multiplet group even if there is limited mutual similarity among all event pairs [Arrowsmith and Eisner, 2006]. The latter approach is illustrated in Figure 4.2, where event 1 is connected to events 2, 3 and 4, but not with events 5, 6 and 7; however, they all belong to the same multiplet group. For this research, the latter approach is selected for its more natural/less strict definition than the requirement of all events being correlated with each other.

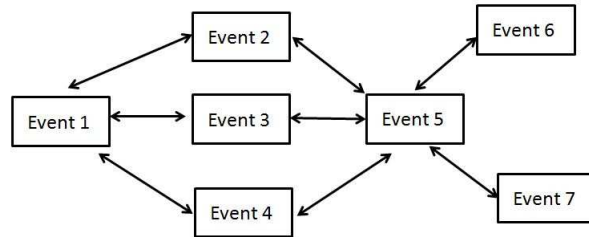


Figure 4.2: Scheme showing the chain-like concept of the clustering algorithm used to identify families of doublets (multiplets). Each box represents a seismic event, and the lines connecting events represent identified doublets. Adapted from Arrowsmith and Eisner [2006].

The definition of a multiplet is subjective and can depend on the application but it is a reasonable approach to gather events that come from the same source region.

4.3 P-wave time repicking method

Errors when picking phase arrivals can affect absolute locations [Pavlis, 1992]. Therefore, assuming waveform similarity between doublets, their relative arrival time readings can be improved through a crosscorrelation procedure. If two microseismic events i and j are doublets, their corresponding time picks at the k th station should be at the same time onset. This P-wave pick refinement consists of extracting two time windows that encompass both P-wave phases and perform crosscorrelation. Then, the time lag corresponding to the maximum peak of the crosscorrelation function represents the shift dt that needs to be corrected to remove any inconsistency in the picks (equation 4.5). This is done in all three components and weighted by each crosscorrelation value. This can also be used to repick S-waves independently:

$$\tau = t_{ik} - t_{jk}, \quad (4.4)$$

$$\tau' = t_{ik} - t_{jk} + dt. \quad (4.5)$$

Where t_{ik} and t_{jk} are the picking times for the i th and j th event recorded at the k th station and dt the time correction needed to align both picks to the same position. τ and τ' are the initial and final relative arrival time difference, respectively. A synthetic example is shown in Figure 4.3.

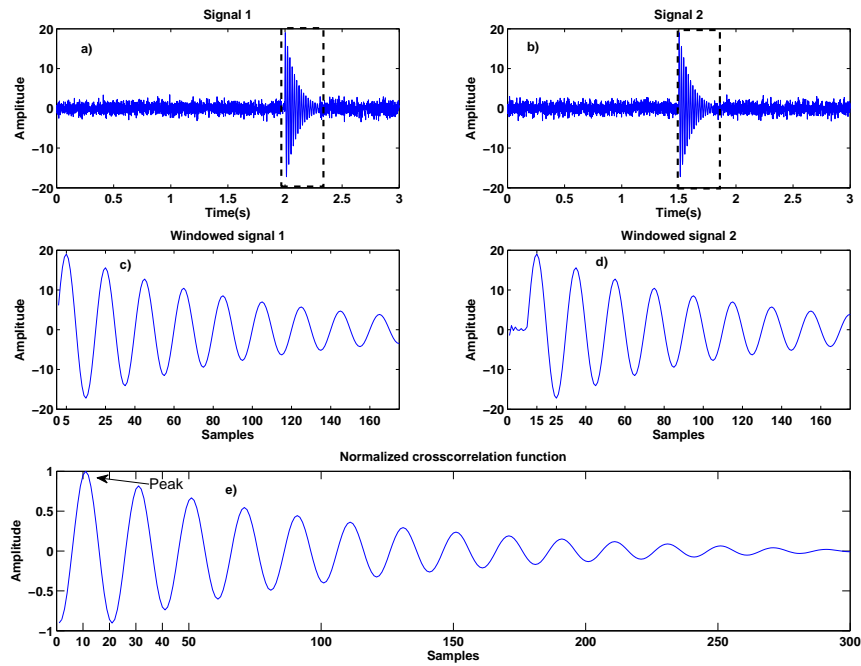


Figure 4.3: Illustration of repicking method using crosscorrelation. a) and b) two synthetic signals representing waveforms from similar events with a 10 samples relative delay. Black dashed rectangles show the time windows taken for crosscorrelation analysis, based on the corresponding initial time picks. c) and d) the two windowed signals zoomed in. Note the delay between the two arrivals is clearly visible, especially clear when first lobe is taken as a reference. e) Normalized crosscorrelation function for these two windowed signals. The lag corresponding to the maximum peak in this function is the time delay between these two signals. This is the dt variable in equation 4.5.

4.4 Double-difference method

The double-difference method (DD) is a relative location method first developed for earthquake seismology [Waldhauser and Ellsworth, 2000] but has much promise in microseismic data analysis. As any relocation method, it works better with dense clustering of events, hence the emphasis on detecting multiplets. The main assumption in the DD method is that ray paths between two events are very similar if their hypocentral separation is small compared to the source-receiver distances; therefore, the relative travel-time difference at a common station will be due to the spatial offset between both events. In other words, the effects of most velocity heterogeneities cancel out, such that only knowledge of the velocities in the source region is required (Figure 4.4). The double-difference residuals for pairs of events at each station are minimized, with the locations and partial derivatives being updated after each iteration, solving the relative hypocentral parameters for each event.

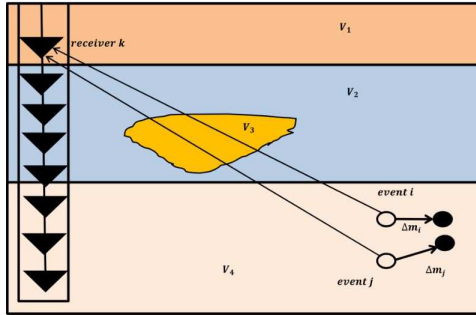


Figure 4.4: Illustration of the double-difference algorithm for microseismic event relocation. For two events, i and j , the initial locations (open circles), relocations (solid circles) and corresponding ray paths to a station k are shown. Thick arrows (Δm_i and Δm_j) indicate the corresponding relocation vectors. Adapted from Waldhauser and Ellsworth [2000].

Since the relationship between the travel times and the location of an event is not linear, a truncated Taylor expansion similar to equation 3.4 is applied to linearize it. Thus, travel time residuals for the i th event are linearly related to perturbations of the hypocentral parameters Δm for each observation:

$$\frac{\partial t_k^i}{\partial m} \Delta m^i = (t_k^{obs} - t_k^{cal})^i. \quad (4.6)$$

Where t_k^{obs} and t_k^{cal} are the observed and theoretical travel times of the i th event at the

k th station and $\Delta m^i = (\Delta x, \Delta y, \Delta z, \Delta t_o)^i$ the changes in the hypocentral parameters that needs to be applied to the spatial coordinates x, y, z and origin time t_o of the i th event to better fit the data. Next, the difference of equation 4.6 for a pair of events i and j can be taken to calculate the relative hypocentral parameters, as suggested by Fréchet [1985]:

$$\Delta t_k^{ij} = (t^{obs} - t^{cal})_k^i - (t^{obs} - t^{cal})_k^j = \frac{\partial t_k^i}{\partial m} \Delta m^i - \frac{\partial t_k^j}{\partial m} \Delta m^j. \quad (4.7)$$

Equation 4.7 is the so-called double-difference equation [Waldhauser and Ellsworth, 2000]. Note that to compute $(t^i - t^j)_k^{obs}$ crosscorrelation methods can be used to determine travel time differences. Waldhauser and Ellsworth [2000] assume constant velocities if the events are sufficiently close together, which can be assured by detecting multiplets. For more clarity, the right-hand side of equation 4.7 can be expanded for a given station k into:

$$\frac{\partial t_k^i}{\partial m} \Delta m^i - \frac{\partial t_k^j}{\partial m} \Delta m^j = \frac{\partial t_k^i}{\partial x} \Delta x^i + \frac{\partial t_k^i}{\partial y} \Delta y^i + \frac{\partial t_k^i}{\partial z} \Delta z^i + \Delta t_o^i - \frac{\partial t_k^j}{\partial x} \Delta x^j - \frac{\partial t_k^j}{\partial y} \Delta y^j - \frac{\partial t_k^j}{\partial z} \Delta z^j - \Delta t_o^j. \quad (4.8)$$

Equation 4.8 shows the partial derivatives evaluated at the current hypocenters, which are calculated for both microseismic events i and j at the station k , where $\Delta x^i, \Delta y^i, \Delta z^i, \Delta t_o^i$ and $\Delta x^j, \Delta y^j, \Delta z^j, \Delta t_o^j$ are the eight unknown hypocentral parameters or perturbations required for both events to make the model better fit the data. In the appendix I explicitly describe how I calculated the partial derivatives.

For example, a small multiplet group with three events and $nsta$ receivers will have the following equations in matrix form:

$$\begin{bmatrix} \Delta t_1^{12} \\ \Delta t_1^{13} \\ \Delta t_1^{23} \\ \vdots \\ \vdots \\ \Delta t_{nsta}^{23} \end{bmatrix} = \begin{bmatrix} \frac{\partial t_1^1}{\partial x} & \frac{\partial t_1^1}{\partial y} & \frac{\partial t_1^1}{\partial z} & 1 & -\frac{\partial t_1^2}{\partial x} & -\frac{\partial t_1^2}{\partial y} & -\frac{\partial t_1^2}{\partial z} & -1 & 0 & 0 & 0 & 0 \\ \frac{\partial t_2^1}{\partial x} & \frac{\partial t_2^1}{\partial y} & \frac{\partial t_2^1}{\partial z} & 1 & 0 & 0 & 0 & 0 & -\frac{\partial t_2^3}{\partial x} & -\frac{\partial t_2^3}{\partial y} & -\frac{\partial t_2^3}{\partial z} & -1 \\ 0 & 0 & 0 & 0 & \frac{\partial t_3^2}{\partial x} & \frac{\partial t_3^2}{\partial y} & \frac{\partial t_3^2}{\partial z} & 1 & -\frac{\partial t_3^3}{\partial x} & -\frac{\partial t_3^3}{\partial y} & -\frac{\partial t_3^3}{\partial z} & -1 \\ \vdots & \vdots \\ \vdots & \vdots \\ 0 & 0 & 0 & 0 & \frac{\partial t_{nsta}^2}{\partial x} & \frac{\partial t_{nsta}^2}{\partial y} & \frac{\partial t_{nsta}^2}{\partial z} & 1 & -\frac{\partial t_{nsta}^3}{\partial x} & -\frac{\partial t_{nsta}^3}{\partial y} & -\frac{\partial t_{nsta}^3}{\partial z} & -1 \end{bmatrix} \begin{bmatrix} \Delta x_1 \\ \Delta y_1 \\ \Delta z_1 \\ \Delta t_{o1} \\ \Delta x_2 \\ \Delta y_2 \\ \Delta z_2 \\ \Delta t_{o2} \\ \Delta x_3 \\ \Delta y_3 \\ \Delta z_3 \\ \Delta t_{o3} \end{bmatrix} \quad (4.9)$$

In other words, for all event pairs $i, j = 1, 2, \dots, N$ and all stations $k = 1, 2, \dots, n_{sta}$, a system of linear equations can be written in the following matrix form:

$$\Delta d = G \Delta m. \quad (4.10)$$

Where \mathbf{G} is the partial derivative matrix of size $M \times 4N$, M is the number of double-difference observations, N is the number of microseismic events; Δd is the residual data vector of double-difference $(t^{obs} - t^{cal})_k^i - (t^{obs} - t^{cal})_k^j$ for all event pairs; Δm is a vector of length $4N$ containing the changes in the hypocentral parameters that need to be determined, namely $(\Delta x, \Delta y, \Delta z, \Delta t_o)^i$. To keep valid the main assumption of the method, I add a weighting matrix \mathbf{W} to give more importance to observations from similar events:

$$\mathbf{W} \Delta d = \mathbf{W} \mathbf{G} \Delta m. \quad (4.11)$$

Another step applied during relocation is to keep the cluster centroid (barycenter) fixed since this technique improves relative locations but not necessarily the absolute ones. The following constraint is applied:

$$\sum_{i=1}^N \Delta m_i = 0. \quad (4.12)$$

4.4.1 Matrix structure

As seen in the previous DD equations, the matrix \mathbf{G} is highly sparse since each equation relates only two events, there are only eight non-zero elements out of the $4N$ columns in each of the M rows. In order to enhance the numerical stability of the solution, the partial derivative matrix \mathbf{G} is scaled by normalizing the $L2$ – *norm* of each column of \mathbf{G} . This also allows solving for problems brought by differences in orders of magnitude between spatial hypocenter parameters and origin times, whose different contributions might bias the final solution. After the solution vector Δm is obtained, the scaling factor is removed.

\mathbf{G} can be ill-conditioned due to a poor event linking between events, making the solution unstable [Waldhauser and Ellsworth, 2000]. Thus, a way to regularize this system is damping the solution:

$$\mathbf{W} \begin{bmatrix} \mathbf{G} \\ \lambda \mathbf{I} \end{bmatrix} \Delta \mathbf{m} = \mathbf{W} \begin{bmatrix} \Delta \mathbf{d} \\ \mathbf{0} \end{bmatrix}. \quad (4.13)$$

Where λ is the damping factor. This is an empirical value that depends on the data, in general, a trade-off curve can be implemented to select the most appropriate damping factor.

4.4.2 Solution

In order to solve equation 4.11, the normal equations can be used:

$$\Delta \hat{\mathbf{m}} = (\mathbf{G}^T \mathbf{W}^{-1} \mathbf{G})^{-1} \mathbf{G}^T \mathbf{W}^{-1} \Delta \mathbf{d}. \quad (4.14)$$

That allows solving the problem in a weighted least-squares sense, i.e., minimizing the L_2 -norm of the double-difference vector $\Delta\mathbf{d}$.

For small and well-constrained systems, equation 4.11 can be solved using the method of singular value decomposition (SVD) [Waldhauser and Ellsworth, 2000]. For larger systems, the solution $\hat{\Delta\mathbf{m}}$ can be found by using the conjugate gradient algorithm by Paige and Saunders [1982]. The latter is used in this thesis. The damped least-squares problem becomes:

$$\left\| \mathbf{W} \begin{bmatrix} \mathbf{G} \\ \lambda \mathbf{I} \end{bmatrix} \Delta\mathbf{m} - \mathbf{W} \begin{bmatrix} \Delta\mathbf{d} \\ \mathbf{0} \end{bmatrix} \right\|_2 = 0 \quad (4.15)$$

to solve for $\Delta\mathbf{m}$.

The initial solution is the a priori knowledge, e.g. the set of initial locations determined by any other conventional absolute location algorithm. In this thesis, the grid search algorithm is used.

4.4.3 Weighting scheme

The weighting scheme design is another major step in any inversion process, especially when relocating correlated and uncorrelated events simultaneously, since it controls which observations will impact more the final locations. The correlation value is an appropriate measure of event similarity between events situated close together; therefore, waveform similarity represents an appropriate variable of weight [Got et al., 1994]. However, for events located farther apart, the correlation coefficient is less indicative of event separation due to wavefield scattering and variations in source mechanisms [Menke, 1999, Waldhauser and Ellsworth, 2000]. As a result, it is necessary to include a weight based on inter-event distance. Both weights are combined in the technique presented here. Although not applied in this research, another option is to apply a residual-based weighting to reject/downweight observations with large residuals caused by data outliers [Waldhauser and Ellsworth, 2000]. The equation used for correlation-based weighting is

$$W_{CC}^i = \alpha \times CC^d, \quad (4.16)$$

where W_{CC}^i is defined as the correlation-based weighting that corresponds to the i th event pair, CC is the crosscorrelation coefficient between any two microseismic events defined in equation 4.3, α and d are the scaling factor and exponential value, respectively, which control the shape of the weighting curve to emphasize correlated over uncorrelated event pairs. Next, for distance-based weighting I use

$$W_{dist}^i = \max\left(0, 1 - \left(\frac{s_i}{dmax}\right)^a\right)^b, \quad (4.17)$$

where W_{dist}^i is defined as the weighting based on the separation distance for the i th event pair. s_i is the separation distance between two microseismic events, $dmax$ is the maximum inter-event separation to be included, and a and b are exponents that shape the weighting curve [Waldhauser and Ellsworth, 2000]. This weight is applied to downweight pairs with larger separation distances that do not meet the main assumption of the method.

In this inversion problem, I choose as initial solution m_o the set of initial absolute locations and weights of the events. Then the process is as follows: with the initial solutions of the events and weights for each event pair within each multiplet group, the partial derivative matrix \mathbf{G} as well as the theoretical travel time differences are calculated, whereas the observed travel time differences can be calculated through cross-correlation or by measured arrival times. Then the system of linear equations is solved, the vector Δm is computed, the scaling is removed and the solution is updated $m = m_o + \Delta m$. These steps are repeated in an iterative way until some stopping condition is met such as the number of iterations, a minimum threshold in the residual vector or if the change in the solution between successive iterations is below a specific number.

A disadvantage of the method is that a considerable number of events recorded at several common receivers can produce a significant system of observations whose solution is slow and computationally inefficient. For example, a dataset containing 1000 microseismic events recorded at a conventional single borehole with 10 receiver stations would result in almost five million double-difference observations. To avoid that, other parameters are included to restrict the number of observations in the system: maximum number of neighbors per event, minimum number of links between event pairs. A higher minimum of these variables do not necessarily assure a stable solution, as there are other more important factors, e.g., receiver array geometry, SNR. Finally, other approaches such as increasing the minimum correlation level between neighbors, or decreasing the maximum separation between uncorrelated events

can also speed up computing times, however; they will have more influence in the final solution since more emphasis will be given to even higher-correlated events.

4.5 Application to synthetic data

Before applying the algorithm to real data, it is recommended to apply it on synthetic data. The main steps to recreate this test are the following:

- Assume a set of microseismic event locations (21 events), surrounded by a receiver array (four boreholes containing four receivers each).
- Assume the velocity of a single phase (P-wave velocity of 3800 m/s), source and receiver locations are perfectly known, then the travel times of the seismic waves to all receiver stations are computed.
- Computed travel times are perturbed by adding randomly distributed noise.
- Perturbed travel times, an assumed velocity model, receiver and starting event locations are inputs to the relocation algorithm. In other words, equation 4.11 is solved. For simplicity, equal quality weights are assigned to all observations.
- Compare final event relocations with true event locations to test accuracy of the method and impact of factors such as noise, velocity and receiver geometry.

Figure 4.5 shows that when using noise-free arrival times, the technique determines the 21 seismic locations accurately. For simplicity, the initial locations are located at the center of the array. If initial locations are randomly distributed (around the same barycenter as the true locations), the method continues to retrieve the true solution, as shown in Figure 4.6. This demonstrates the technique is independent of the starting locations. In reality, catalog locations can be used as starting locations as they usually are close to the true hypocenters (Figure 4.7), while keeping the barycenter fixed after relocation if no consistent errors are affecting the absolute locations [Waldhauser and Ellsworth, 2000]. If consistent errors are present in initial locations, then final locations are affected, as shown at the bottom of Figure 4.8, where a shift of 20 m to West produces accurate relative locations but incorrect absolute locations. This shows that the method does not necessarily improve absolute locations. As a result, the barycenter should remain fixed before and after relocation (equation 4.12).

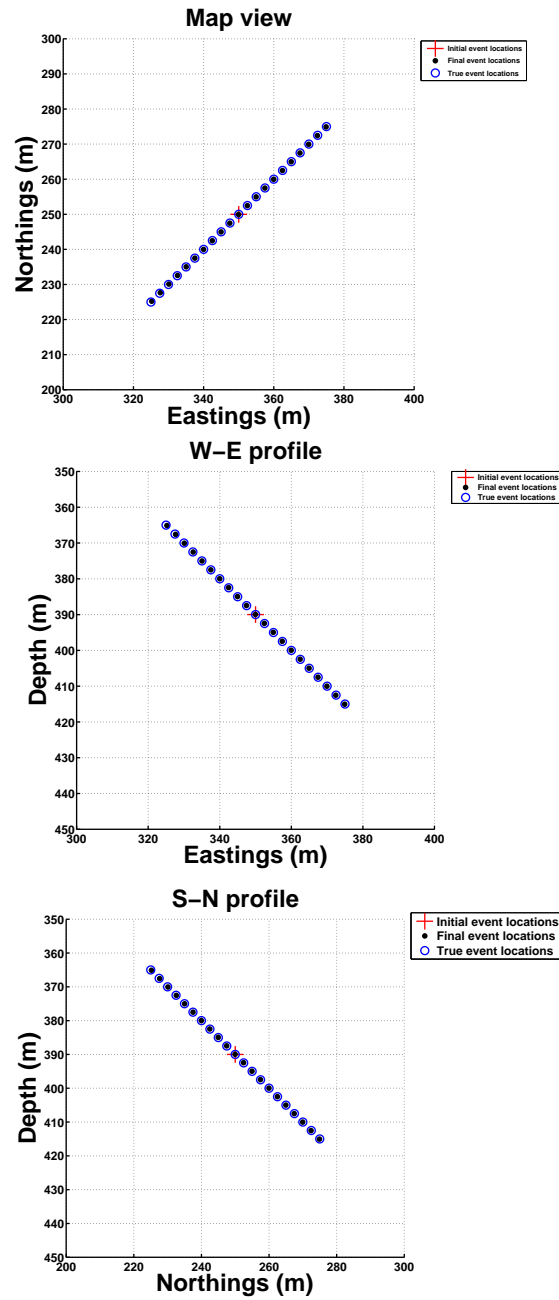


Figure 4.5: Location with noise-free time readings. Top: Map view. Middle: W-E profile. Bottom: S-N profile. Source locations are all initialized at the barycenter of the true location. Blue circles: true locations. Red crosses: Initial locations. Black circles: Final locations.

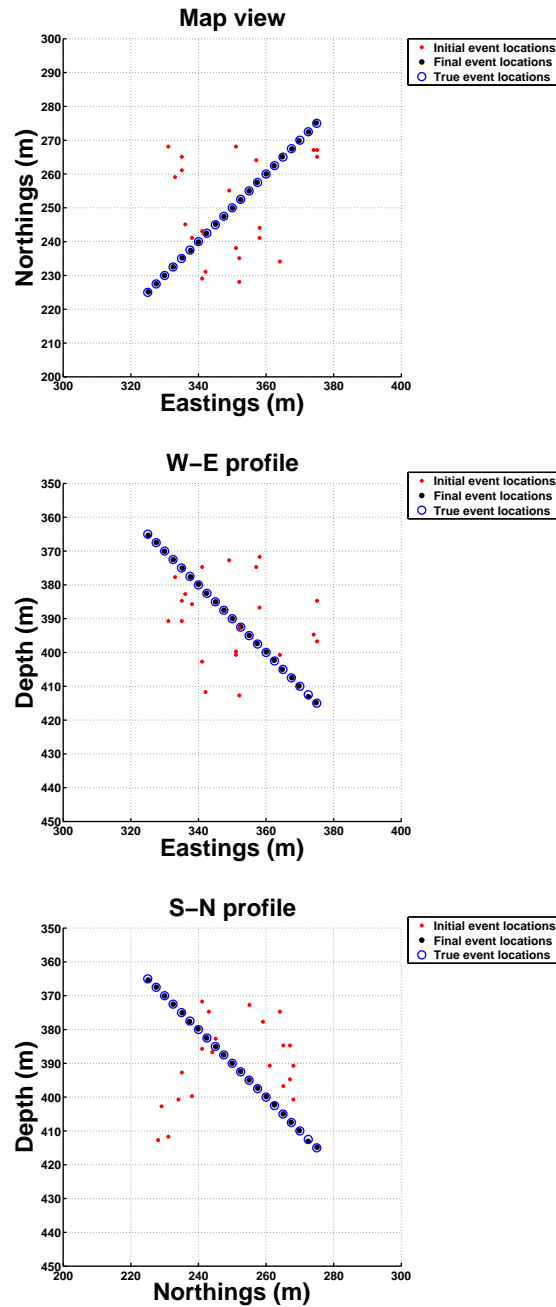


Figure 4.6: Location with noise-free time readings. Top: Map view. Middle: W-E profile. Bottom: S-N profile. Initial locations are randomly distributed with the barycenter matching the true barycenter. Blue circles: true locations. Red circles: Initial locations. Black circles: Final locations.

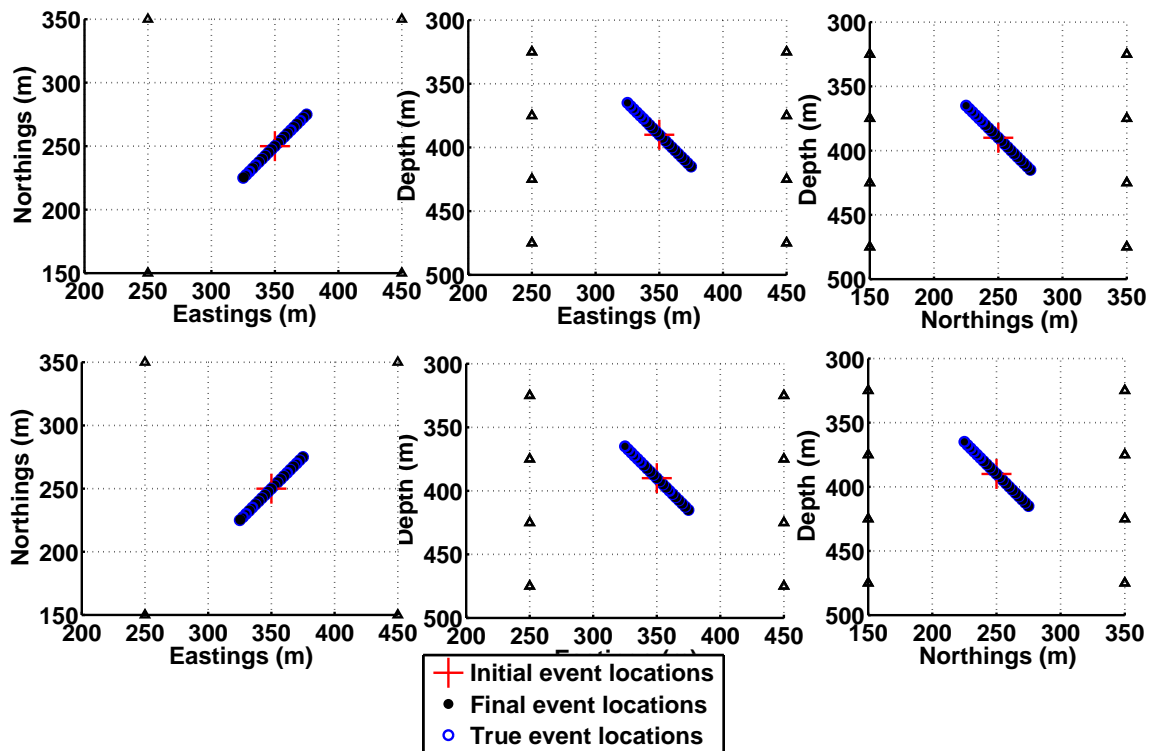


Figure 4.7: Comparison of event locations when using the true barycenter as initial locations. Top row: final barycenter constrained to true barycenter. Bottom row: barycenter unconstrained. Even when the final barycenter is not constrained, the final locations virtually coincide with the true locations, as the initial locations start at the true barycenter. Black solid circles: Final locations. Open blue circles: True locations. Red crosses: Initial locations.

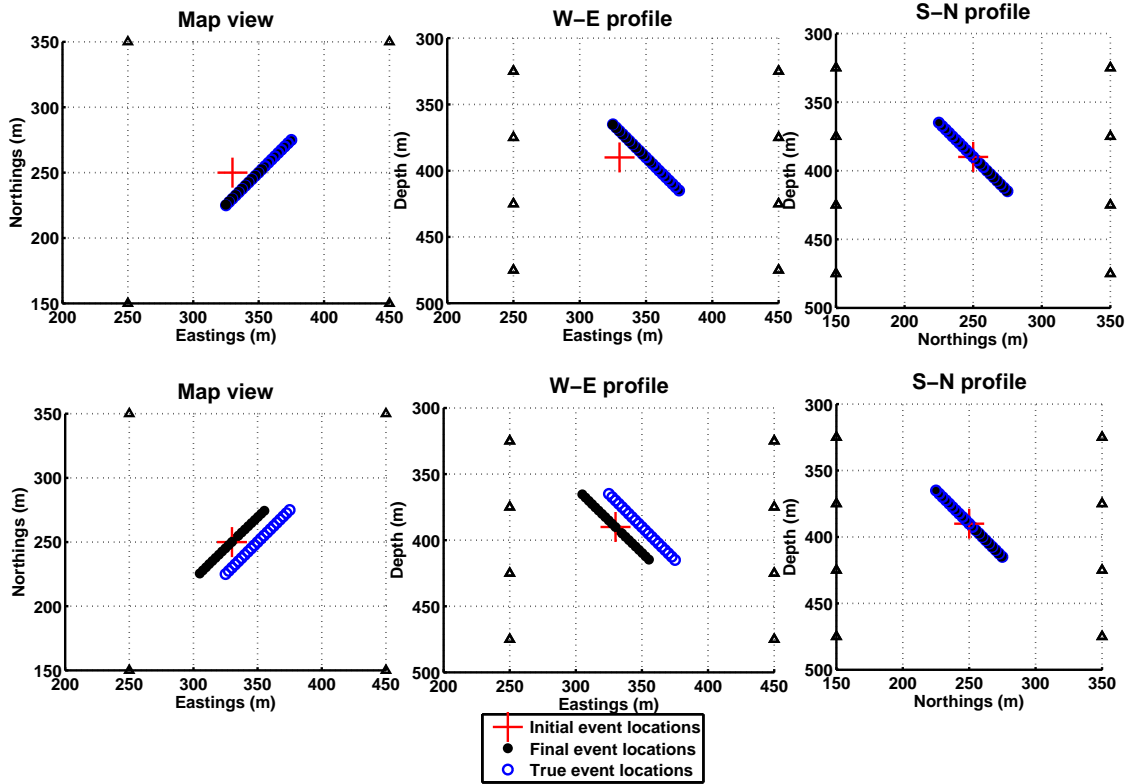


Figure 4.8: Comparison of event locations when using initial locations shifted 20 m to West and no added errors to travel times. Top row: final barycenter constrained to true barycenter: the final locations retrieve the true locations. Bottom row: Barycenter unconstrained. The final locations virtually coincide with the correct relative locations but the absolute barycenter remains shifted 20 m to West. A systematic error in all initial locations (20 m to West) does not allow the technique to recover the true event locations. Black solid circles: Final locations. Open blue circles: True locations. Red crosses: Initial locations.

4.5.1 Effect of noise

To simulate better a real case scenario, random errors are added to computed travel times, since it is well known that picking errors have an impact on the subsequent final locations. Figure 4.9 shows as an example the locations using arrival times with 10% of added noise. Each location is not retrieved perfectly; nevertheless, the linear trend is still obtained. The more noise is added, the less accurate the final locations are. Several noise percentages are tested with the results displayed in Figure 4.10, which shows that noise affects less the epicentral locations, compared to the depth (in this specific receiver array). It shows how the discrepancy (relative error between the final and true locations) increases with the noise percentage in arrival times. This is linked to SNR, therefore, to have more reliable locations, events with high or relatively-high SNR should be used.

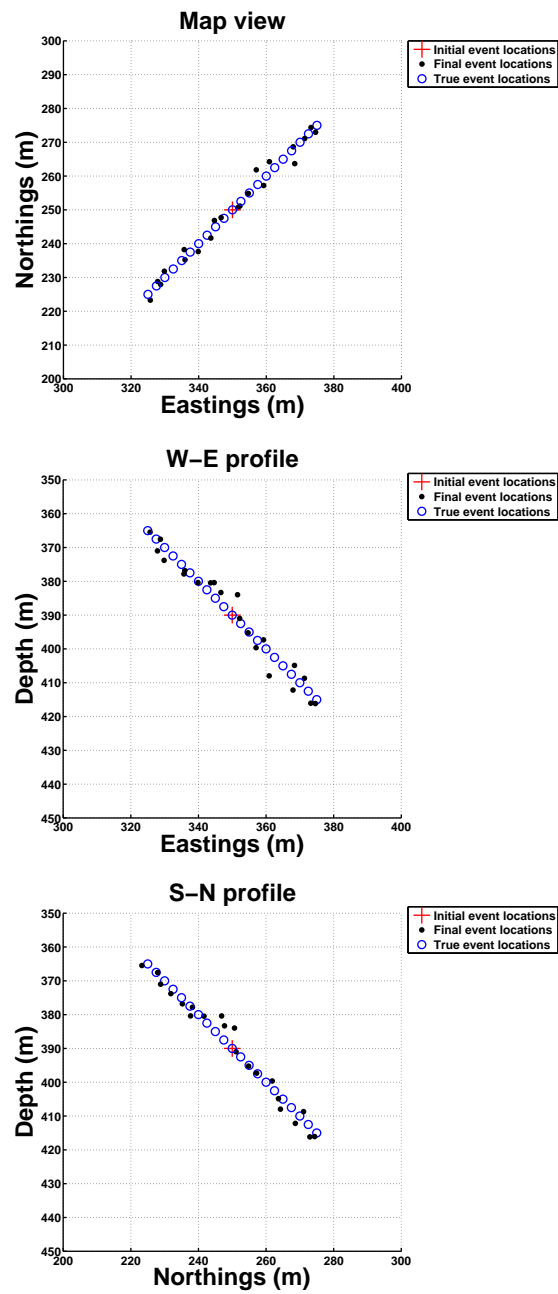


Figure 4.9: Location using travel times with 10% of added random noise. Top: Map view. Middle: W-E profile. Bottom: S-N profile. Blue circles: true locations. Red crosses: Initial locations. Black circles: Final locations.

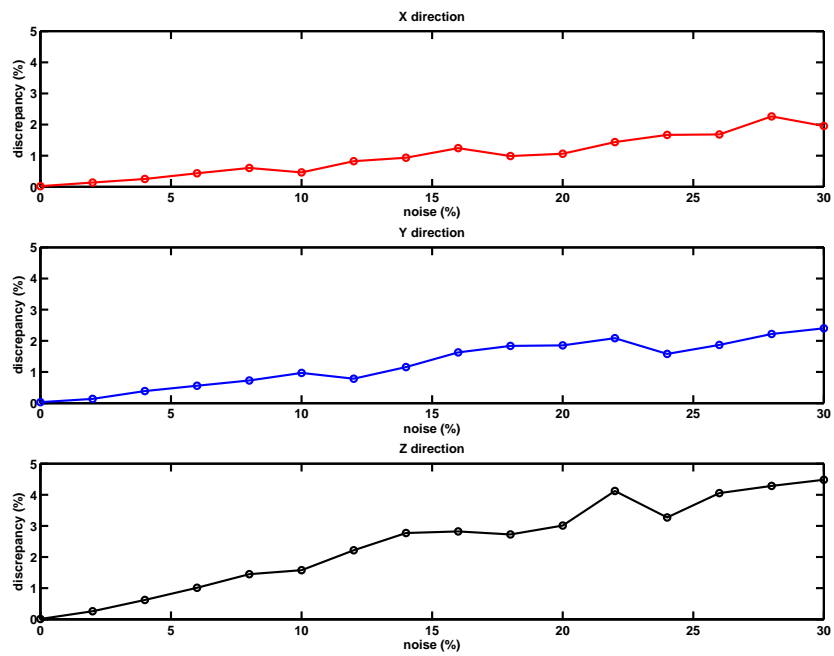


Figure 4.10: Percentage of location discrepancy (using true location as reference) as a function of noise present in time readings. For this array, the horizontal locations are less affected by noise than the depth locations.

4.5.2 Effect of velocity

It was previously mentioned that the velocity model used in microseismic monitoring is only an approximation to the true velocity structure, so it is important to know the effect of an underestimated and overestimated velocity model. For simplicity, a constant layering is assumed in this test. Figures 4.11 and 4.12 shows the final locations using a velocity model 20% lower and higher than the true velocity structure, respectively. In the former, the spatial separation between events is reduced; whereas in the latter spatial separations are enlarged. Nevertheless, in both cases, the linear shape of the cluster remains. A similar test was done by Kocon and van der Baan [2011], obtaining similar results. In this test I also invert for the 21 origin times, but they are not affected by the under/over estimation of the velocity model, since the results coincide.

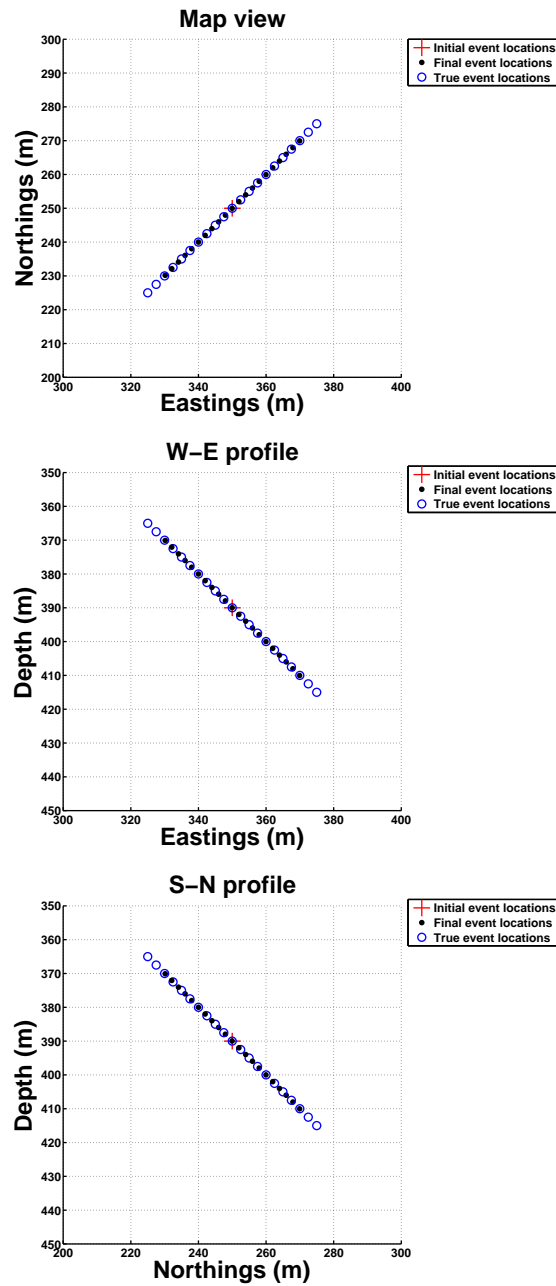


Figure 4.11: Location with noise-free time readings and underestimated velocity model (-20%). Top: Map view. Middle: W-E profile. Bottom: S-N profile. The events have shortened inter-event distances. Blue circles: true locations. Red crosses: Initial locations. Black circles: Final locations.

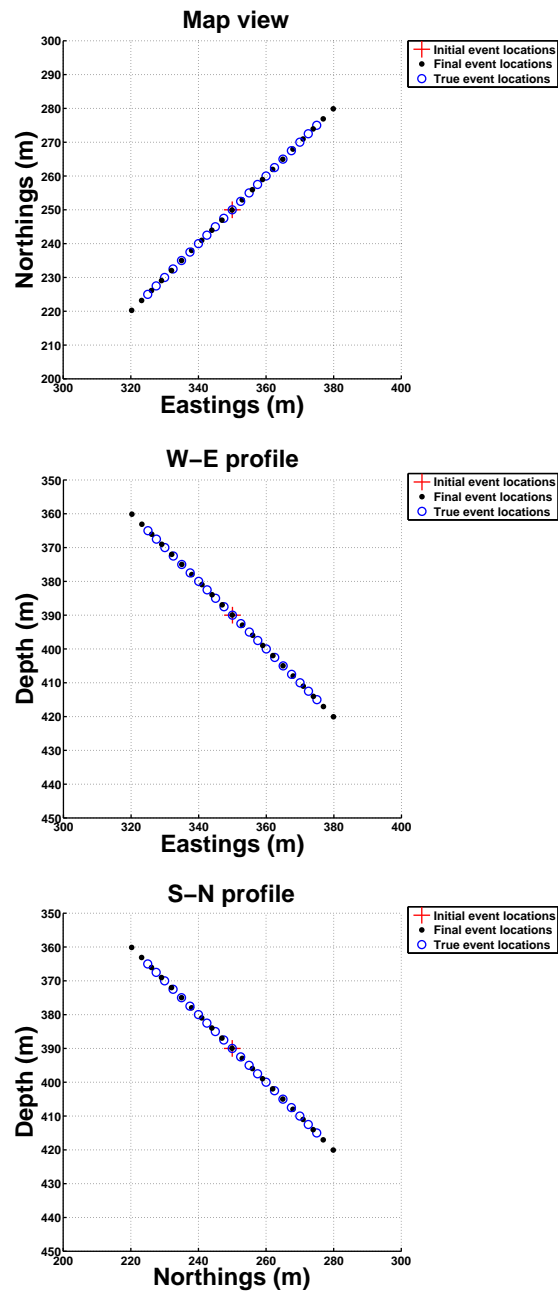


Figure 4.12: Location with noise-free time readings and overestimated velocity model (+20%). Top: Map view. Middle: W-E profile. Bottom: S-N profile. The events have enlarged their inter-event distances. Blue circles: true locations. Red crosses: Initial locations. Black circles: Final locations.

4.5.3 Effect of receiver array

In this case, two receiver arrays are shown. The first consists of two vertical boreholes aligned to the strike of the cluster. In this case the locations are retrieved accurately (see Figure 4.13). However, the second case involves two vertical boreholes aligned perpendicular to the strike of the cluster; as a result, the locations are erroneous as the technique is not able to constrain the inter-event distances along the main direction of the cluster (see Figure 4.14). The quality of the final relocations thus improves with the completeness in the azimuthal coverage, highlighting the importance of the acquisition geometry on the final results.

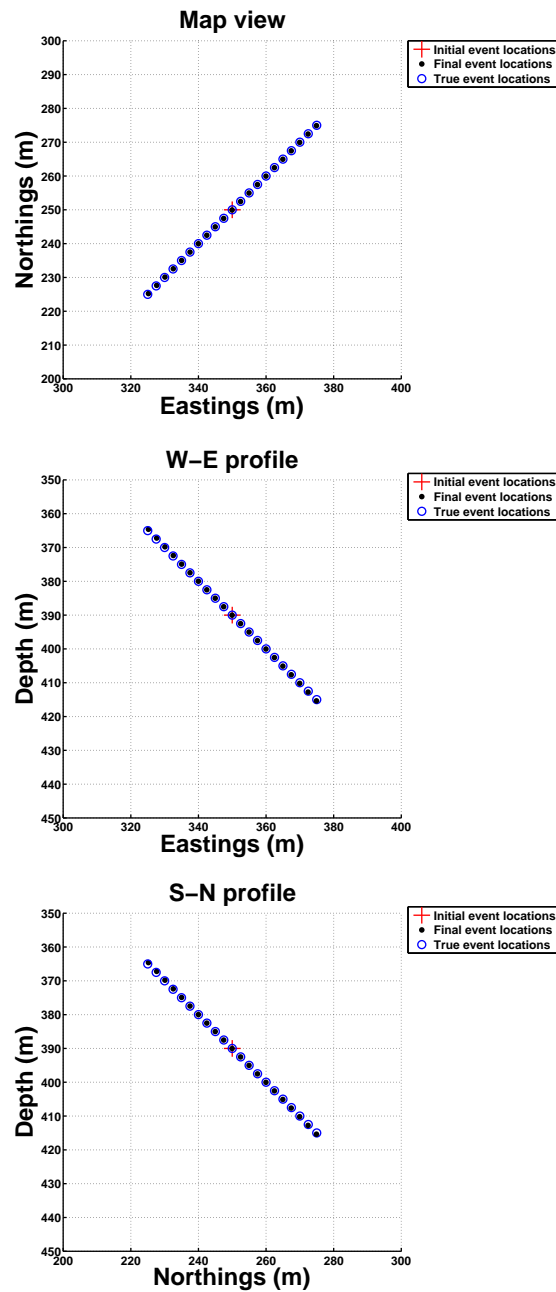


Figure 4.13: Location with noise-free time readings and two boreholes (four receivers each) aligned with the cluster strike. Top: Map view. Middle: W-E profile. Bottom: S-N profile. This configuration constrains the locations accurately, as the inter-event distance is in the same direction. Blue circles: true locations. Red crosses: Initial locations. Black circles: Final locations. The two boreholes are located at epicentral coordinates [Eastings:200 m, Northings:100 m] and [Eastings:500 m, Northings:400 m] respectively, at depths from 325 m to 475 m equally spaced.

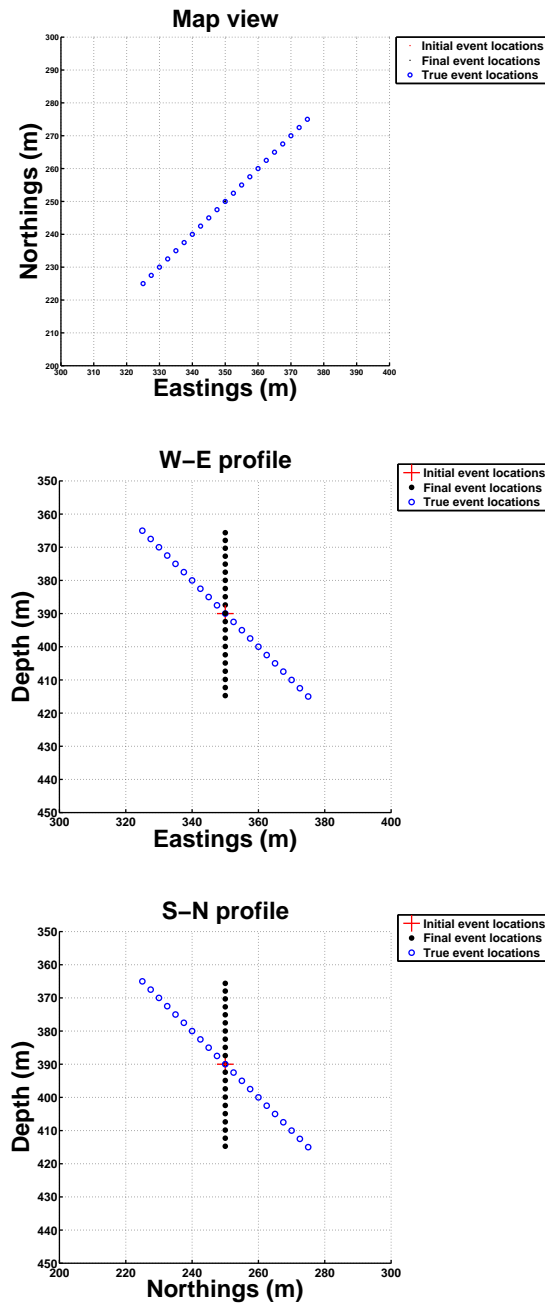


Figure 4.14: Location with noise-free time readings and two boreholes (four receivers each) orthogonal to the cluster strike. Top: Map view. Middle: W-E profile. Bottom: S-N profile. This configuration does not constrain the locations accurately, as the direction of the receiver boreholes is orthogonal to the cluster strike, thus the array is not sensitive to the main events direction. Blue circles: true locations. Red crosses: Initial locations. Black circles: Final locations. The two boreholes are located at epicentral coordinates [Eastings:200 m, Northings:400 m] and [Eastings:500 m, Northings:100 m] respectively, at depths from 325 m to 475 m equally spaced.

CHAPTER 5

Case study: Background.

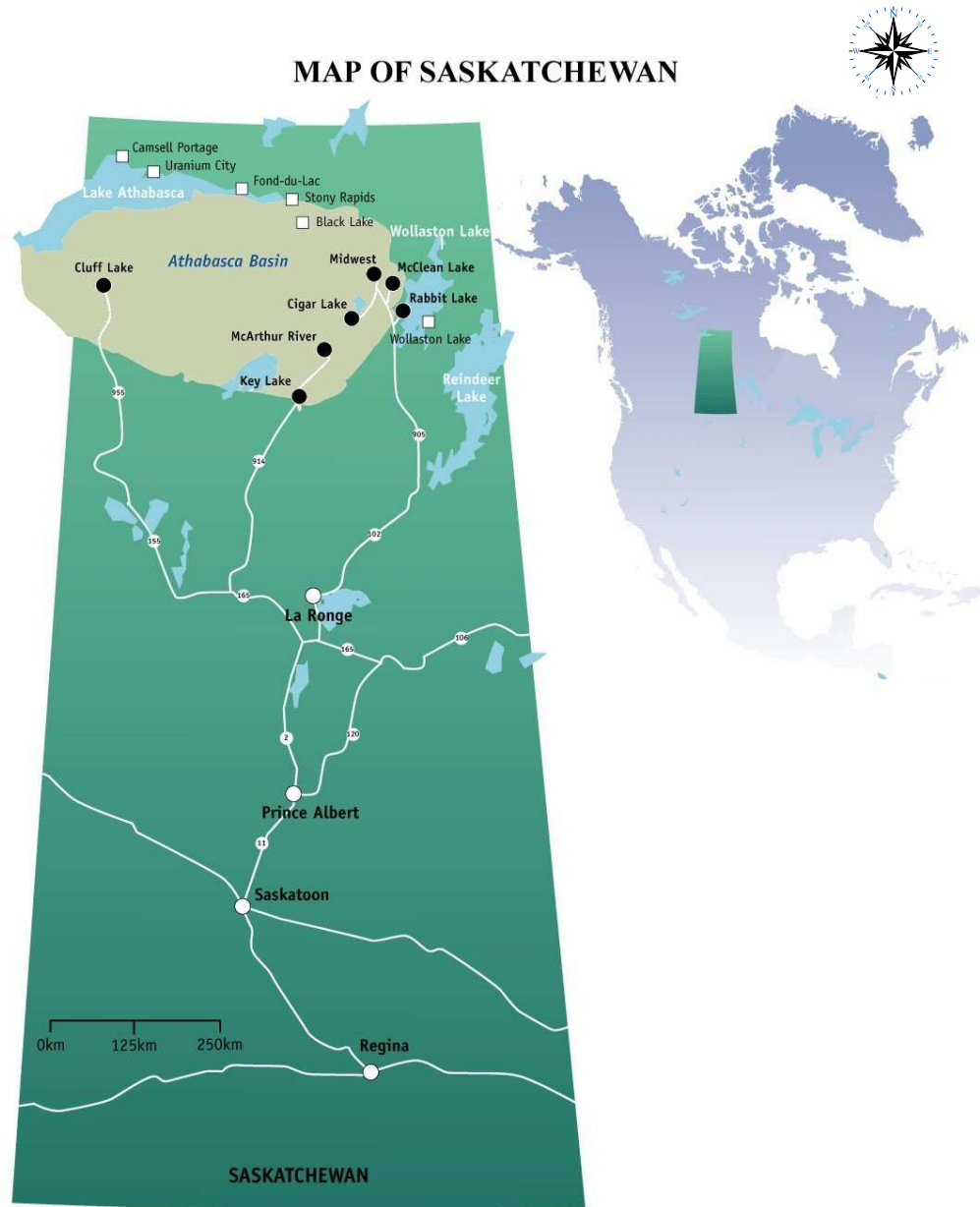
5.1 Introduction

This case study involves the passive monitoring of the Cigar Lake mine, located near Waterbury Lake, approximately 660 km north of Saskatoon (Figure 5.1). With an estimate of 537000 tonnes of U_3O_8 at a typical grade of 18.3%, it is considered the second largest known high-grade uranium deposit and its uranium grades are over 100 times the world average in uranium deposits [Bishop et al., 2012]. It was discovered in 1981 by a program of diamond drill testing of geophysical anomalies and since then, several drilling campaigns have been carried out as well as geotechnical and geophysical programs. Sandstones surrounding the deposit contain large volumes of water at significant pressure. Due to water-inflow incidents that flooded the underground mine, a microseismic system has been installed, as part of a mine remediation process and to further investigate this deposit and assess potential zones of seismicity.

This chapter introduces the geological background at Cigar Lake and presents the microseismic monitoring installation and problems encountered during acquisition and processing.

5.2 Geological setting

The Cigar Lake uranium deposit is located approximately 40 km within the eastern part of the Athabasca Basin of northern Saskatchewan, Canada. It is located at the unconformity contact separating the Aphebian metasedimentary gneisses and plutonic rocks from Wollaston Group (Lower Proterozoic) and the Helikian sandstones of the Athabasca Group (Middle



DWG. No. C000-F-096

Figure 5.1: Geographical location of Athabasca Basin and Cigar Lake mine. Taken from Bishop et al. [2012].

Proterozoic), as seen in Figure 5.2. Locally, there are two major lithostructural domains present. First, a southern area with pelitic metasedimentary gneisses (Wollaston Domain) and a northern area with large lensoid granitic domes (Mudjatik Domain). Bishop et al. [2012] have characterized the Cigar Lake deposit as a flat-lying lenticular body at depths between 410 and 450 m. Sizewise, the deposit is approximately 1950 m long, 20-100 m wide and up to 13.5 m of thickness, with an average of 5.4 m. It shows remarkable longitudinal and lateral geological continuity. Its crescent shaped cross sectional outline closely reflects the topography of the unconformity (Figure 5.3). The host sediment is referred as the Manitou Falls Formation, deposited in an intracontinental sedimentary basin filled by fluvial quartz sandstones and conglomerates. To the east side of the basin, sandstones from Athabasca Group and metamorphic gneisses that form the unconformity host most of the uranium mineralization.

Previous geochronological studies suggested two main periods of uranium mineralization in northern Saskatchewan [Cumming and Rimsaite, 1979, Philippe and Lancelot, 1993]. One related to the Hudsonian orogeny (1800 Ma), which generated vein-type deposits. The second period produced unconformity-type uranium deposits in the Athabasca Basin (1300 to 1100 Ma), where migration of hot hydrothermal brines concentrated and remobilized the deposits. Subsequent tectonics in the zone produced northeast trending fault structures and mylonitic corridors, where secondary uranium mobilization has occurred. These are currently located above the main deposit and are classified as perched mineralization, with no economic interest (Figure 5.3). Later studies also suggest more control by paleohydrology, basement topography and reactivated basement structures [Fayek and Kyser, 1997].

5.3 Geological challenges

5.3.1 Water inflow incidents

Over the period 2006 through 2008, the project suffered several setbacks as a result of three water inflow incidents that affected both shafts, affecting mine workings done at that point in time. Remediation plans were carried out to restore the underground workings. This included rehabilitating lower risk areas of the mine, such as the 480 and 500 m levels, preparing areas to resume construction activities, replacing electrical components damaged due to flooding, re-establishing the mine ventilation circuit and the start of a freezing program in shaft No. 2 [Bishop et al., 2012]. The installation of a freezing infrastructure, the

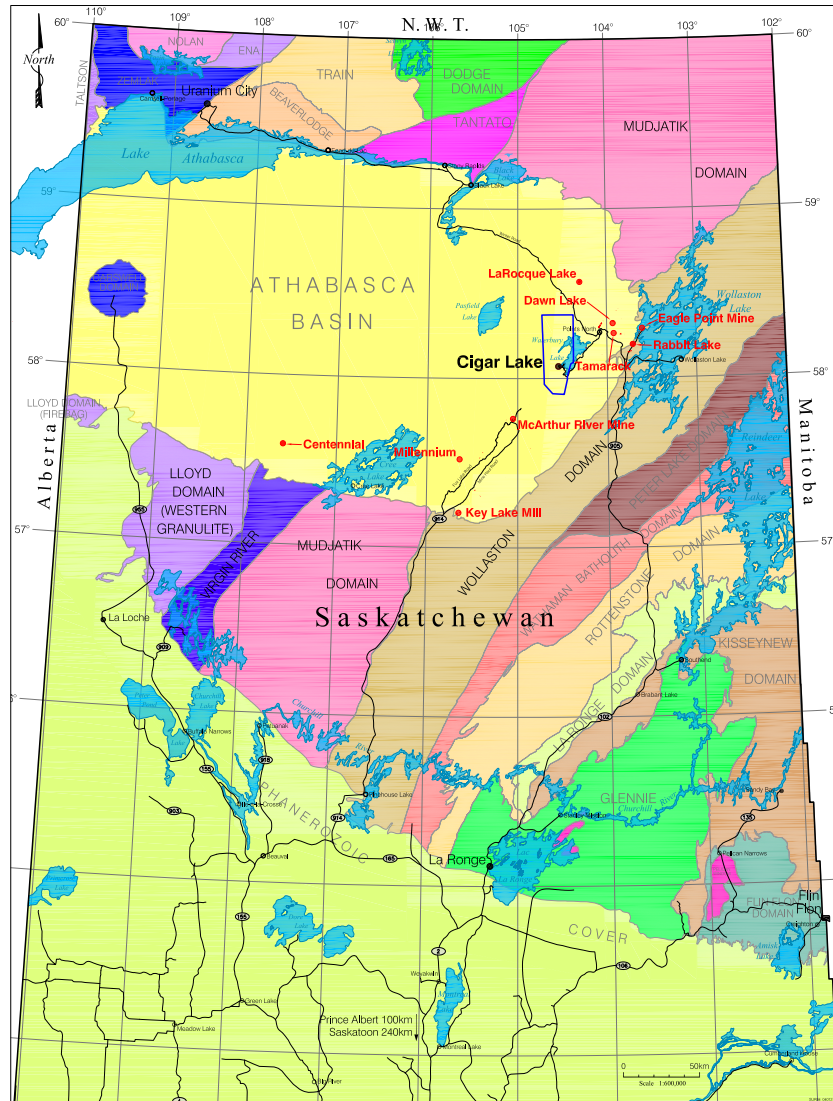


Figure 5.2: Geological map of Northern Saskatchewan. Cigar Lake mine is located at the unconformity between Wollaston Group and the Athabasca Group. Each color represents a lithostructural domain. Taken from Bishop et al. [2012].

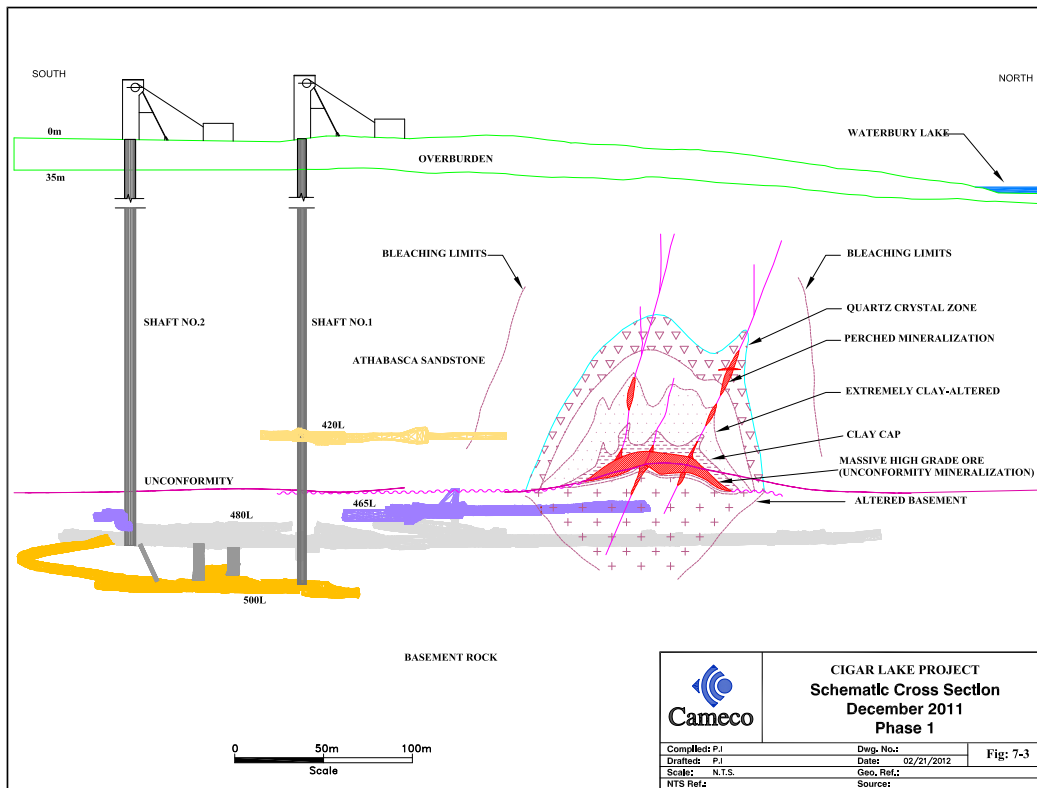


Figure 5.3: South-North cross-section of the Cigar Lake mine. Important features are displayed: the deposit with its lenticular shape (towards the north) and the 465 and 480 m level (gray and purple colored crosscuts). Taken from Bishop et al. [2012].

forefront strategy, was completed in early 2011 and the freeze system activated, whose aim has been to minimize the risk of water inflow and increase rock stability.

5.4 Microseismic installation

A microseismic system was installed at the Cigar Lake project in October 2008, in order to monitor zones of potential instabilities and possible water inflows during the mine remediation process. The first phase involved the deployment of six boreholes containing four three-component geophones each which surround the mine workings, covering an area of approximately 600 m x 600 m. Next, an additional eight geophones were installed in a seventh borehole (labeled as BH-7) near the center of the monitoring network. The receiver array is displayed in Figure 5.4. The main tunnels and shafts illustrate the complexity of the structure in the area of study, complicating the wave propagation. For instance, Maxwell and Young [1998] studied the propagation effects during underground excavation, finding delays in the P-wave travel times due to tunnels present in the area that produced diffraction. Nevertheless, this installation represents a rare opportunity to monitor seismic and mining activities, since most projects use a single borehole or array of receivers near the surface, mostly due to economic constraints or because microseismic events are usually too weak to be recorded by more than two receiver boreholes. However, as shown in chapter 3, even with time picks available in half of the receivers, microseismic events can be located accurately in this case study.

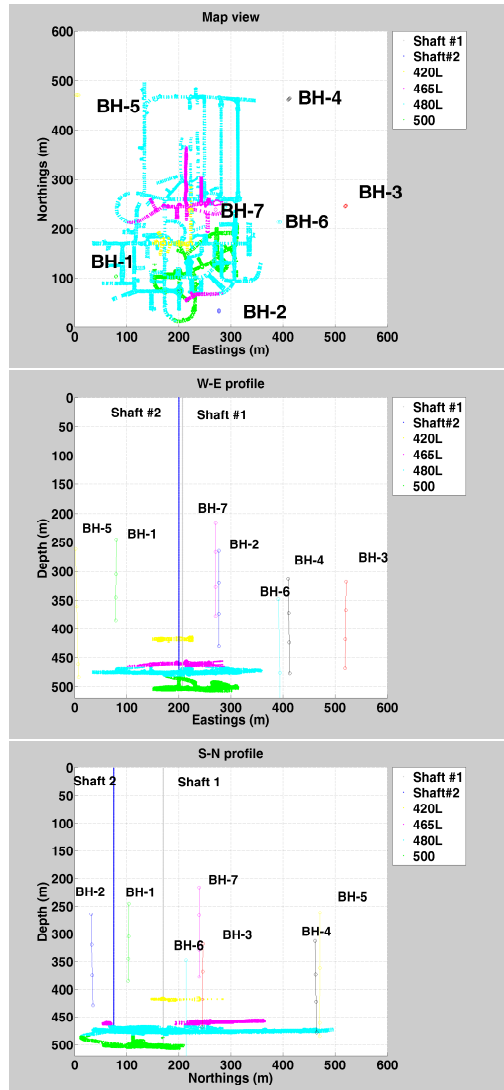


Figure 5.4: Receiver setup at Cigar Lake project. Top: Map view. Middle: W-E cross section. Bottom: S-N cross section. Seven boreholes containing four receivers each (colored open circles). The tunnels at depths of 420, 465 480 and 500 m are visible. Note the latter two located below the unconformity).

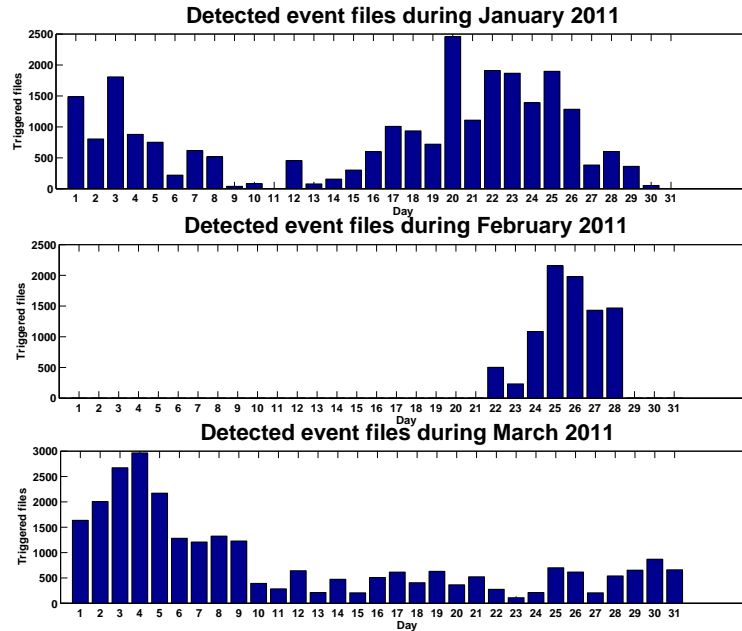


Figure 5.5: Number of triggered event files from January to March 2011. There is a high number of files recorded, false alarms in most cases. In February, the recording system went down except at the end of the month.

5.5 Problems encountered

The recording system implemented generates event files capturing the time frames when high-energy arrivals are detected. Initially, thousands of triggered files recorded from January to March 2011 are under investigation in this thesis (Figure 5.5). During some days at least 2500 event files are recorded, suggesting the presence of a considerably high number of false alarms, possibly due to acquisition parameters set too sensitive to noise levels. Figure 5.6 shows a common triggered file recorded due to noisy arrivals; as a result, a quality control is performed during the pre-processing stage (see chapter 6) to discard such files.

Another acquisition issue is the bad synchronization between receivers, an example is shown in Figure 5.7. Two similar events are displayed, since they have nearly-identical waveforms, it is assumed they originated in a similar region, so they should have similar relative travel time differences between receivers; however, note that the seismic energy of event 1 in bore-hole BH-1 is arriving considerably later when compared to the second event at the same station. These receivers anomalously out of synchrony lead to erroneous time readings, producing mislocated events. The recorded data had similar issues during two months. These

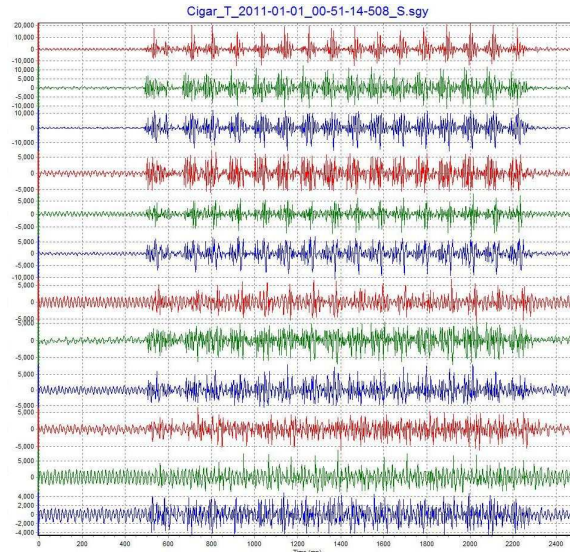


Figure 5.6: Seismogram file triggered by noisy arrivals. These noisy arrivals triggered the recording system very frequently. Four receivers from borehole BH-1 are shown. Components: Horizontal (red and green) and vertical (blue).

problems are also summarized in Figure 5.8, where residual times (arrival time pick minus average arrival time) at each station for all detected events are displayed. For example, note that in February (middle Figure) the first four receivers reflect large arrival time differences (up to 600 ms) compared to the average arrival time, especially during the first 90 events. In addition, these time shifts seem to vary with day, as highlighted by the arrows. In other words, these arrivals have no physical meaning as they do not nearly represent consistent travel times. Similar issues occurred in March, where in general, receivers 1-4 and 9-12 (boreholes 2 and 3) are the most affected. Unfortunately, these delays are not constant and they also vary within the same day, so the data affected by this issue (February and March 2011) is removed during the pre-processing stage, to prevent systematic biases in event locations.

Next I describe the pre-processing and absolute event locations.

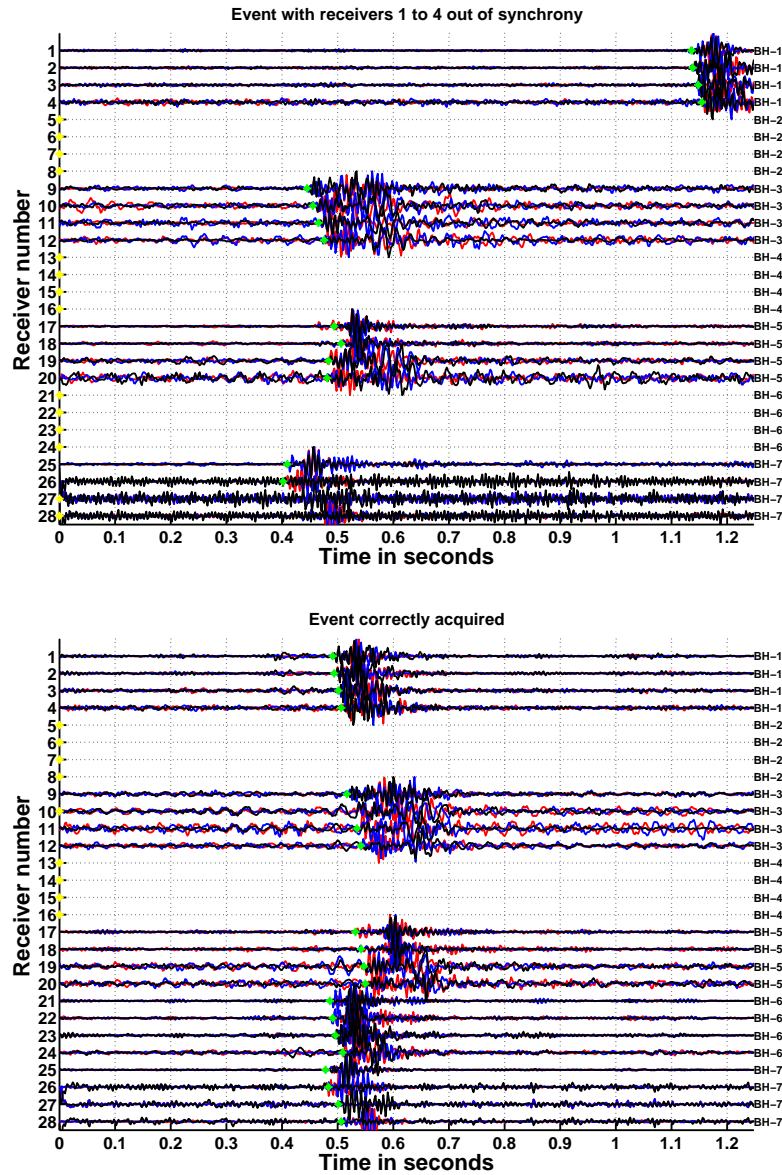


Figure 5.7: Comparison of two similar microseismic events, one of them shows evident synchronization problems. Top: Recorded seismogram showing arrival waveforms with a time delay in receivers 1-4. The relative arrival times in receivers 1-4 is significantly long compared to the remaining receivers. Bottom: Recorded seismogram showing seismic energy arriving at similar times. Both seismograms show receivers with dead traces. Green dots: Initial time picks. Yellow dots: Inactive picks.

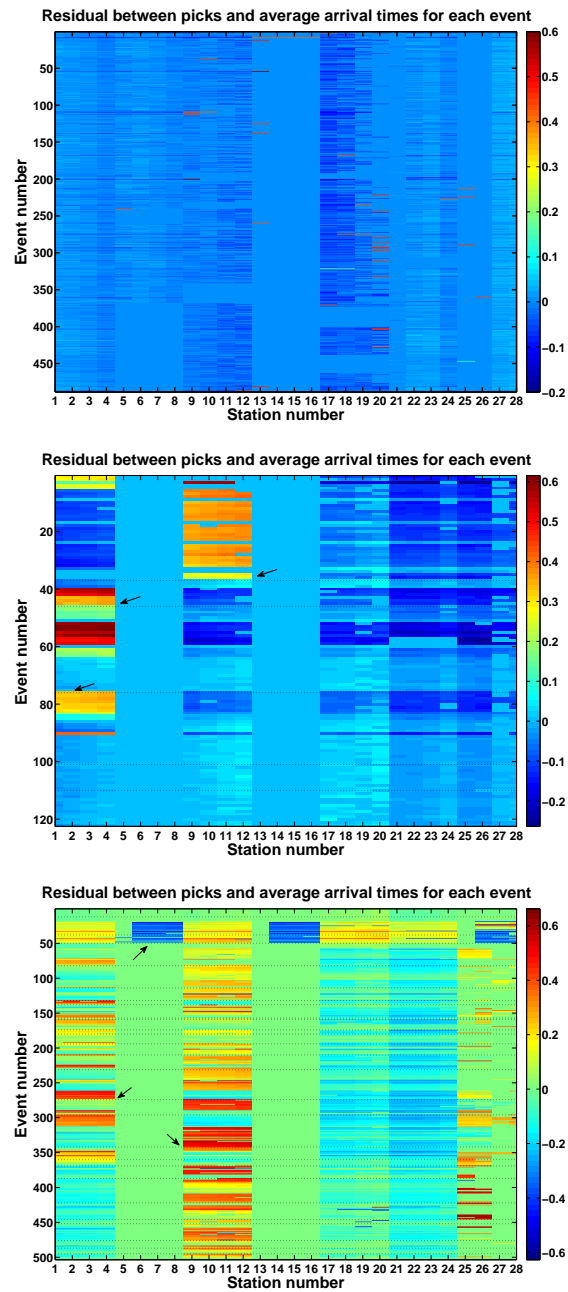


Figure 5.8: Residual between time picks and average arrival times at each station for all detected events in January (top), February (middle) and March 2011 (bottom). Black dotted lines: separation between days of acquisition. Note that for the seismograms recorded in February and March, anomalous arrival times change with day, showing time shifts as long as 600 ms, suggesting synchronization issues between receivers. These delays vary each day, highlighted by arrows. Picked arrival times during February and March are not reliable, as they would produce mislocated events. As a result, the recorded data during those two months are discarded prior to the event location stage.

CHAPTER 6

Case study: Pre-processing.

6.1 Introduction

As mentioned in the previous chapter, a microseismic monitoring system was installed at Cigar Lake mine to continuously detect zones of potential hazards and instabilities. Data recorded from January to March 2011 by 28 three-component geophones are used to investigate microseismic events recorded in seven boreholes. Due to acquisition issues already shown in Figure 5.8, only the data recorded during the January is used, a total of 24821 triggered files. The vast majority of these files contain no useful events but solely noise, possibly due to a very sensitive detection threshold in the equipment installed. As a result, a quality control is performed in order to detect microseismic events and a subsequent pre-processing workflow is applied in order to determine absolute event locations prior to the relocation algorithm under investigation in this thesis.

6.2 Bandpass filter

After loading each microseismic triggered file into a Matlab environment, a trapezoidal bandpass filter is applied after several tests are done. Figure 6.1 shows the effect of the final bandpass filter, where frequency corners [65 80 170 180] Hz are used. The frequency range varies within data set, but this represents the most appropriate filter coefficients and is not so harsh, keeping only desired frequencies as much as possible. It is important to remove frequencies associated with noise, since errors due to correlation of noise can substantially

affect the identification of similar events and impact the final microseismic locations.

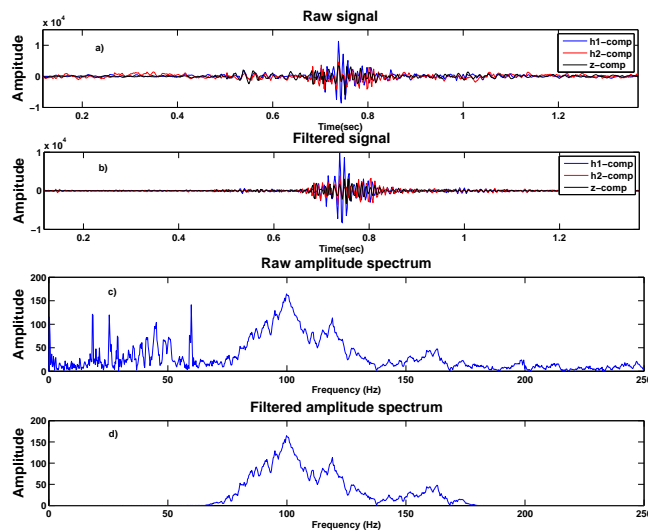


Figure 6.1: Effect of bandpass filter in one of the microseismic events. a) and b) seismogram for raw and filtered waveforms, respectively. The raw data is highly contaminated by peaks below 65 Hz (mainly electrical noise) and noisy arrivals around 0.55 s. After applying this filter [65 80 170 180] Hz, the P-wave is clearly the first strong arrival observed in the seismogram. c) and d) amplitude spectrums of raw and filtered data, respectively. The filter preserves the desired bandwidth, attenuating noisy peaks below 65 Hz.

6.3 Automatic event detection and onset picking

Using the conventional *STA/LTA* method stated in equation 2.3 [Allen, 1978], the triggered files are re-analyzed to reduce the large number of false alarms. Akram and Eaton [2012] suggested that the *STA* window size should be three or more times the dominant period of the signal and *LTA* to be 10 or more times larger than the *STA* window. Since the signal in general have a dominant period of 8 ms, a short and long time window of 30 and 300 ms is used, respectively. Figure 6.2 shows a three-component seismogram containing a microseismic event and corresponding *STA* and *STA/LTA* functions. Note that the P-wave arrival (black dashed line) picked in the seismogram as reference, coincides with the most pronounced change in the *STA/LTA* curve (bottom of Figure 6.2). However, this curve overcomes the threshold earlier, so this method might not be considered appropriate for onset picking but for event detection purposes only. With regards to the minimum threshold, a constant threshold of 3 is used as it reasonably meets most events and receiver stations tested. The minimum number of stations where the threshold is overcome is set to 16 to make sure the events arrive at least in four different boreholes. Finally, a quality control is done manually to discard high-energy noisy arrivals that meet the parameters set for the *STA/LTA* method.

The autopicker developed by Sleeman and van Eck [1999] is applied using an AR model order = 2, followed by a quality control to interactively repick incorrect time readings for all 488 detected microseismic events. At this stage automatic picks are added, removed or edited, as shown in Figure 6.3. Only traces whose arrivals show clear onsets are picked to reduce time picking errors.

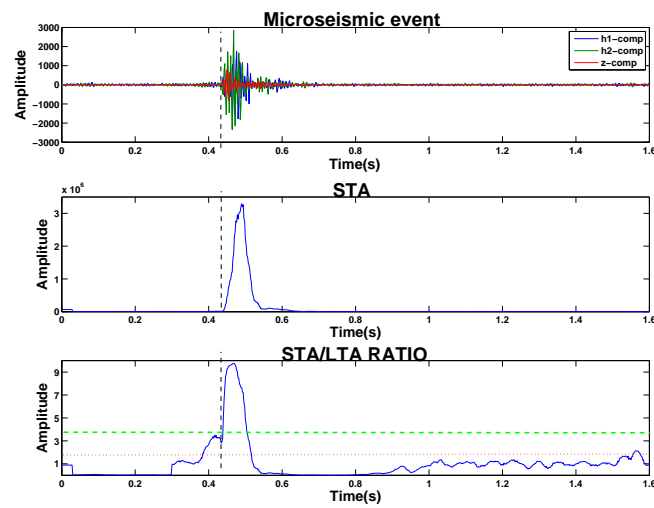


Figure 6.2: *STA/LTA* method to detect microseismic signals. Top: three-component seismogram containing a microseismic event. Middle: Short term average of seismogram. Bottom: *STA/LTA* ratio of the seismogram. This microseismic event shows a *STA/LTA* curve that overcomes the specified threshold (Green dashed line). Red dotted line: Reference value when *STA* and *LTA* windows have equal length. Black dashed line: P-wave pick used as reference.

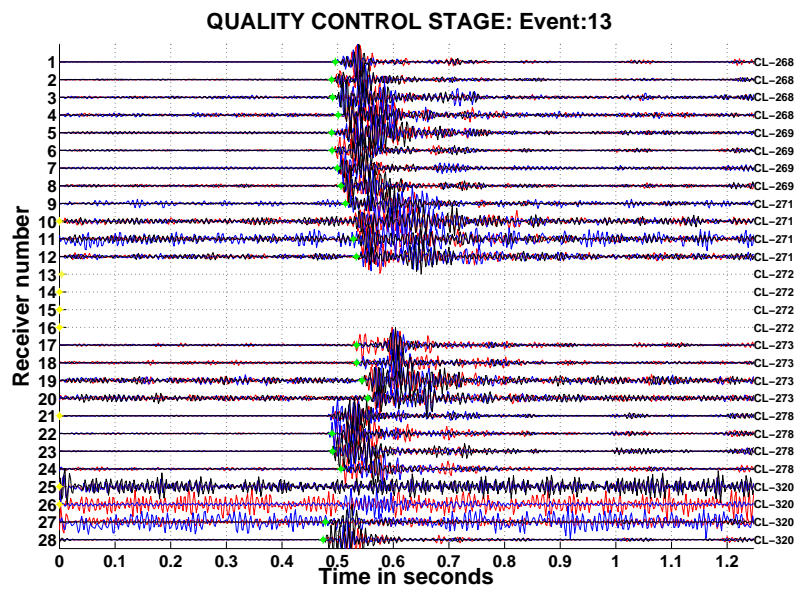


Figure 6.3: Interactive procedure to activate, deactivate or edit P-wave time picks. Each four consecutive traces belong to a receiver borehole. Green points: receivers with arrival times picked. Yellow dots: receivers with no picks, due to dead traces or insufficient signal-to-noise ratios. Receivers 13-16 show dead traces.

Figure 6.4 provides information on amount of picks available in every station. Receivers are designated from #1 to #4 where #1 is the deepest station and #4 the shallowest station in each borehole. The top of the figure shows the percentage of events picked per receiver in each borehole. Some information can be deduced, for instance, borehole BH-4 does not record sufficiently strong waveforms in each of its receivers. Borehole BH-7 is affected by acquisition issues because receivers #1 and #2 have a minimal contribution, compared to receivers #3 and #4 that exhibit more than 95% of picks available. Additionally, the bottom of Figure 6.4 shows the percentage of picks in each receiver borehole, where six out of the seven boreholes have picks at least in 50% of the events, with borehole BH-1 with 97% of picks available, as opposed to borehole BH-4 where only 0.5% of events are picked. This suggests a relatively good receiver patch to apply the relocation technique.

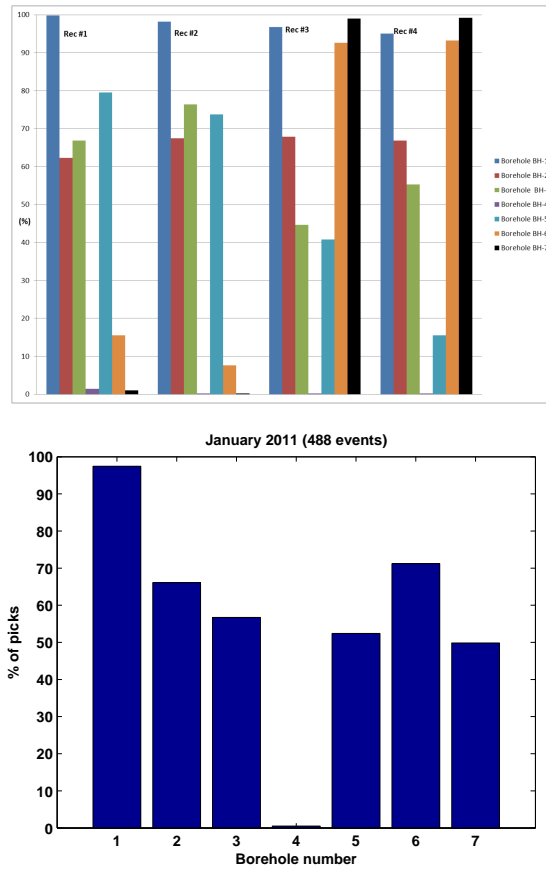


Figure 6.4: Top: Percentage of events picked per receiver in each borehole. Each borehole is represented by a different color. Borehole #6 show receivers with clear signals (receivers 3 and 4) compared to receivers 1 and 2, suggesting also issues in the receiver stations. Boreholes #1, #2 show more consistent waveforms in every receiver, inferred by the amount of picks. Bottom: Total percentage of time picks in each borehole. Most boreholes are picked at least 50%. Borehole #4 does not contribute significantly, due to its far location from the center of the mining activities.

6.4 Velocity model used

A calibrated 1-D velocity model is provided (left of Figure 6.5). This model was done by the data owner after analyzing calibration shots. This consisted of finding the velocity model that generates theoretical travel times that best fit the observed travel times from a source with known location. Seven layers are clearly defined. Unfortunately, these calibration shots are not provided to confirm this final velocity model. To avoid mislocated events along velocity boundaries, the velocity model was smoothed (right of Figure 6.5). Most receivers are located within 350 and 500 m of depth, encompassing the main crosscuts at the 420, 465 and 480 m levels. At this depth range, there are several layers defined between 3500 and 4000 m/s. As a result, in the relocation stage, where constant layering is assumed, the chosen velocity structure is 3700 m/s.

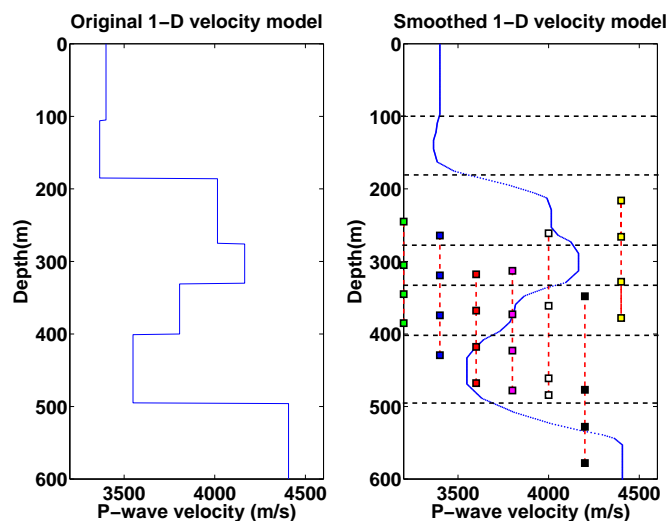


Figure 6.5: Left: Initial 1-D velocity model. The abrupt velocity changes usually produce artifacts, i.e., events located along defined boundary layers. Right: Smoothed 1-D velocity model. Black dashed lines are the layer boundaries. Colored squares: Depth of seven receiver boreholes.

6.5 Absolute event location

A grid search approach is used to determine initial event locations. The grid volume is defined as $600 \text{ m} \times 600 \text{ m} \times 600 \text{ m}$ using a 5 m node spacing, which covers the area of interest. Since only observed arrival times are available, equation 3.1 is used to determine

microseismic locations. The 1-D isotropic velocity model (Figure 6.5) is first tested and results are shown in Figure 6.6. Note that events are scattered within the center of the array, as a possible cluster is seen in the S-N profile of Figure 6.6. There are also some horizontal features at approximately 200 and 280 m depth, which might be artifacts due to sharp velocity changes in the model. There are other depths with sharp velocity changes, but there are no clear lineations associated with those depths, e.g. around 330, 400 and 500 m. In addition, the located seismicity is closer to boreholes BH-4 and BH-5, which is suspicious because most waveforms do not arrive earlier than in the rest of the boreholes. Since a relative location is used further in the post-processing stage, a constant velocity can be assumed for the initial locations in a second test using $V_p=3700$ m/s and the results are shown in Figure 6.7. Most events are located at the center of the array (top of Figure 6.7), and the barycenter is moved closer to boreholes BH-1 and BH-2 and BH-7. This is expected since they have recorded the most clear and strong waveforms (top of Figure 6.4). Also note, a large number of events (75%) are initially located between 400 and 500 m deep. A few events are located at the edge of the grid, suggesting events originated below the grid defined, where the receiver array does not resolve locations well. The assumption of constant velocity can be applied when using relative methods, instead of using more complex velocity models, since relative location approaches assume that the events are closely clustered.

Figure 6.8 shows the corresponding residuals for the 1-D isotropic and homogeneous velocity models. The residual is the difference between observed and theoretical travel times in each station available. Using $V_p=3700$ m/s generates smaller residual values (standard deviation of 0.0136 s), hence providing a better data fitting, compared to the 1-D isotropic model (standard deviation of 0.0415 s).

Figure 6.9 displays a histogram of the seismicity depths, with a mean of 460 m and 73 % within 400-500 m deep. There are also events located below 500 m of depth, whose locations are not constrained by the receiver array.

Since the absolute locations have been determined for all microseismic events, I proceed to find groups of similar events and apply the relocation algorithm based on the double-difference. These results are described in the next chapter.

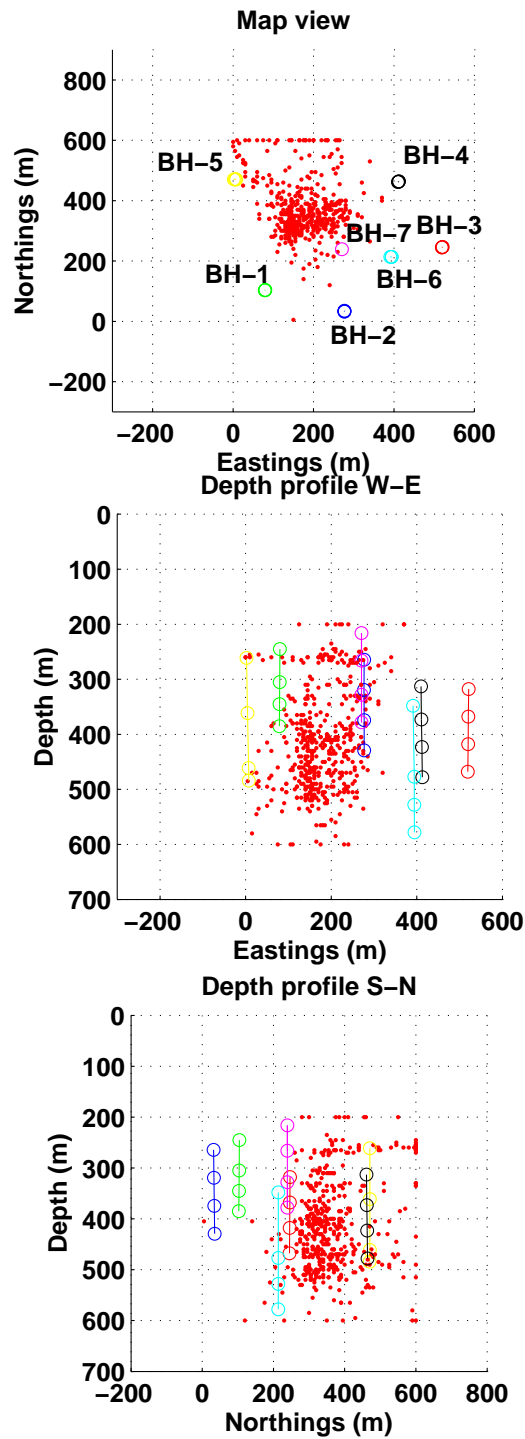


Figure 6.6: Absolute locations of 488 events assuming a 1-D isotropic velocity model shown in Figure 6.5. From top to bottom: Map view, West-East and South-North cross-sections, respectively. There are some horizontal lineations at some depths with sharp velocity changes e.g. 200 and 280 m. There are no visible horizontal lineations around 330, 400 and 500 m depth.

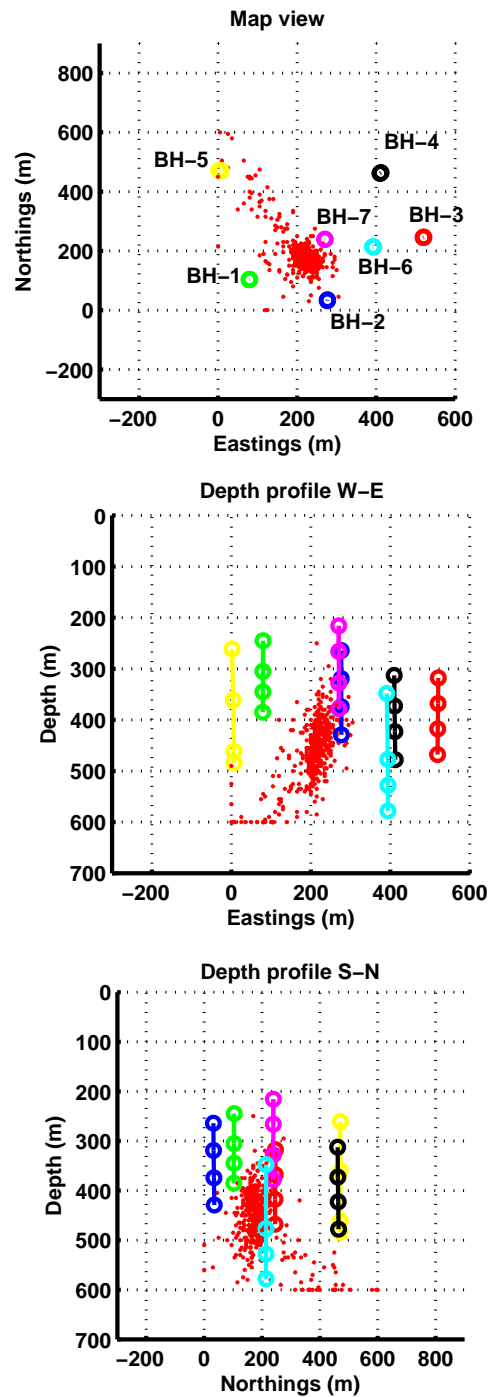


Figure 6.7: Absolute locations of 488 events assuming homogeneous velocity model $V_p=3700$ m/s. From top to bottom: Map view, West-East and South-North cross-sections, respectively. Most events are located at the center of the array at depths between 400 and 500 m.

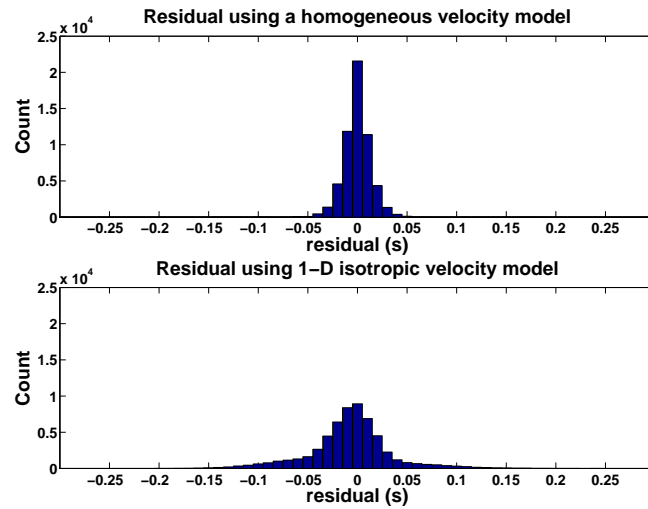


Figure 6.8: Histogram of residuals (observed minus theoretical travel times) between pairs of stations available for the 488 microseismic events. Top: 1-D isotropic velocity model. Bottom: Homogeneous velocity model. The constant velocity assumption fits better the observed arrival times.

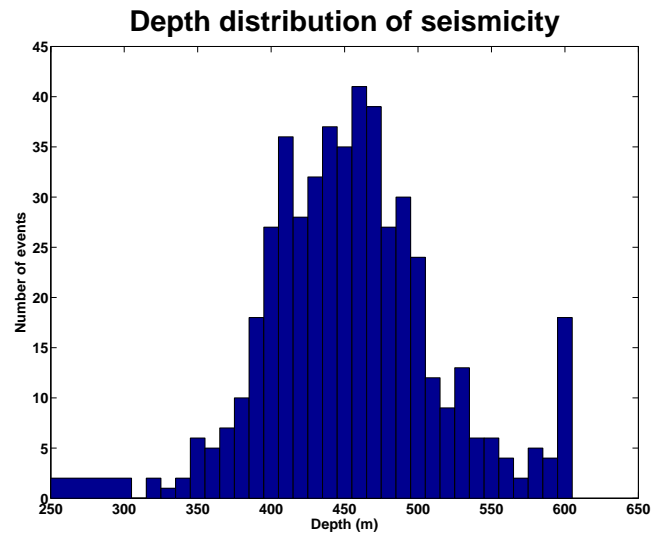


Figure 6.9: Depth distribution of the 488 microseismic events assuming an homogeneous velocity model $V_p=3700$ m/s.

CHAPTER 7

Case study: Multiplets and Double-difference technique. ¹

7.1 Introduction

In this chapter the post-processing stage described in chapter 4 is applied to the case study.

7.2 Event similarity

In the previous chapter I showed the initial locations for all 488 microseismic events, so the identification of similar events using a crosscorrelation procedure described in this chapter [Arrowsmith and Eisner, 2006]. Figure 7.1 shows four highly similar microseismic events recorded at a common station. Also, the time windows based on their corresponding time picks are highlighted. As previously stated, a short length may ignore part of the useful information, giving erroneous correlation values, whereas a longer length may include multiple scattered late-arriving energy which is not useful for this similarity assessment. After visualizing most seismograms, a 170 ms crosscorrelation time window is chosen, as it encompasses both phases.

After setting the correlation time window, the minimum correlation level to detect doublets is considered. Figure 7.2 shows the total number of events in multiplets groups (linking the events in a chain-like fashion) as a function of the minimum correlation level. As expected, the number of multiplets is inversely proportional to the correlation threshold. Note that

¹A version of this chapter has been presented ([Castellanos and van der Baan, 2012]) and published ([Castellanos and van der Baan, 2013]).

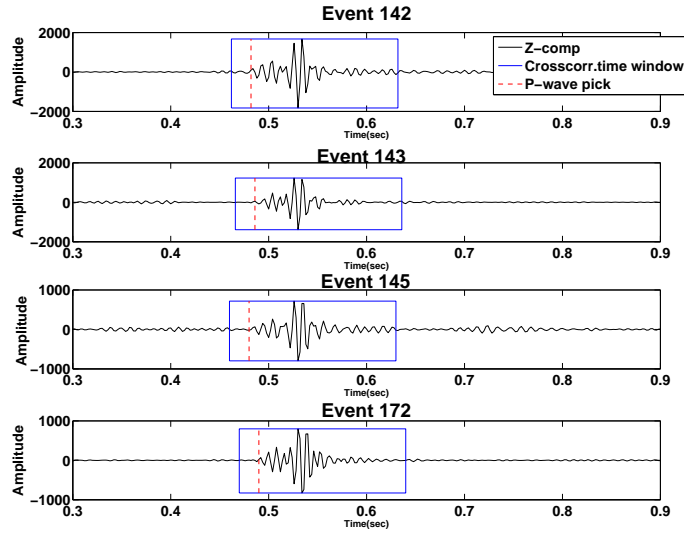


Figure 7.1: Four microseismic events recorded at a common station. Only the vertical component is displayed. Based on the time picks (red dashed line), a time window that only encompasses signal is selected, and the crosscorrelation value is calculated for all three-components and all common receivers, using a weight based on the maximum amplitude for each component. The events shown are at least 80% similar with one another.

for a threshold of 0.55 and lower all events are linked, as opposed to a high correlation condition ≥ 0.9 where less than 2% of events are connected. A threshold of 0.8 is chosen since a considerably high amount of events (58%) is detected as multiplets and is sufficiently high to meet the "similarity" assumption, as demonstrated in Figure 7.1.

Table 7.1 shows the number of similar events detected per multiplet group using 0.8 as a minimum correlation value. The corresponding histogram is also displayed in Figure 7.3.

Number of groups	Number of events
9	2
6	3
3	6
1	10
1	38
1	179

Table 7.1: Number of events per multiplet group found. Two major multiplet groups are found in this data set (38 and 179 events).

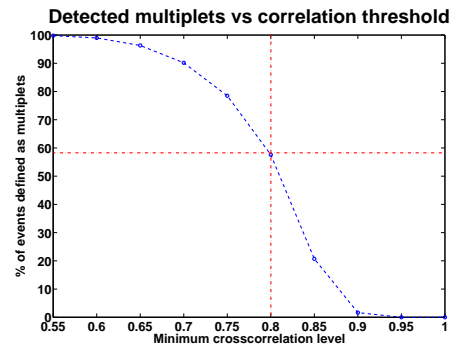


Figure 7.2: Percentage of multiplets identified as a function of minimum correlation level. There is a trade-off, the correlation level must be sufficiently high so events are considerably similar but sufficiently low to identify an useful amount of events. The red dashed line shows 0.8 as chosen threshold and 58% events are detected as multiplets.

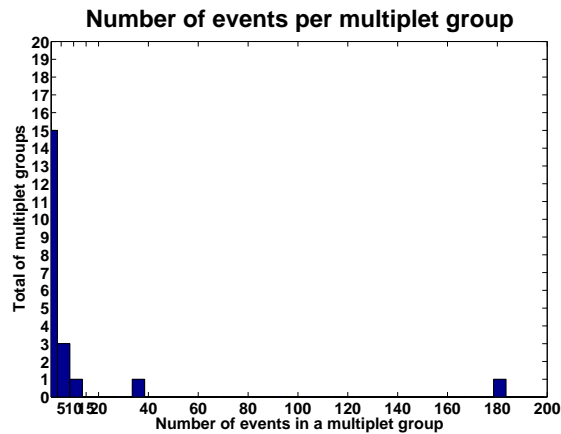


Figure 7.3: Histogram of events per multiplet group. There are two large multiplet groups, having 179 (group 1) and 38 (group 3) events, respectively. Most of the remaining groups are doublets.

Figure 7.4 shows the upper triangular correlation matrix for the 488 detected events, which allows for a quick assessment of the similarity between all event pairs. The left side has the correlation values in chronological order. Note there is no apparent consecutive seismicity in similar areas. Hence, they appear disorganized because similar events often occur randomly. In the right part of Figure 7.4 the correlation values are ordered by multiplet group, where the aforementioned two largest multiplet groups are clearly visible as they appear highly correlated. The remaining smaller groups cover a smaller area in the matrix. This data set has an average correlation of 0.6 (60%), which shows that in general, events that do not belong to the same cluster can still show a considerably medium to high correlation.

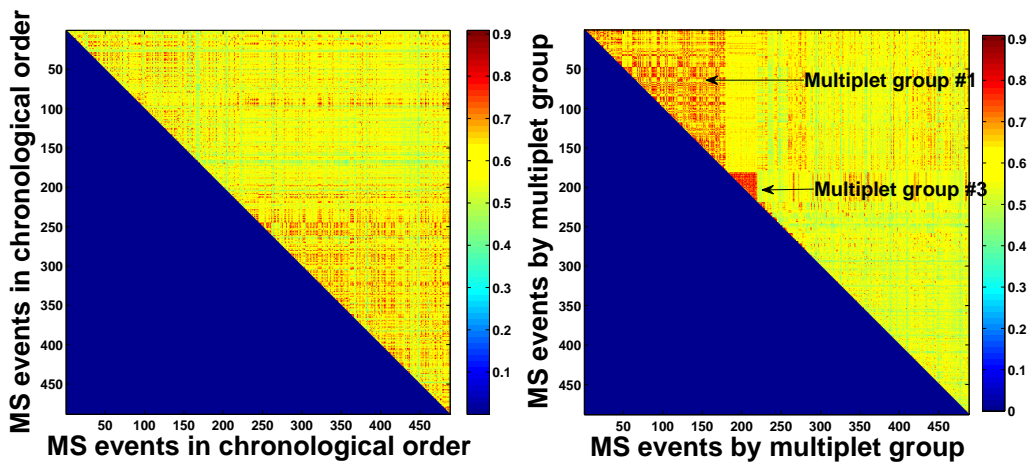


Figure 7.4: Upper triangular crosscorrelation matrix for 488 events detected in January 2011. Each cell gives the crosscorrelation coefficient between any pair of events. Blue: correlation is zero. Red: perfect correlation of one. Left: MS events in chronological order. Right: MS events ordered by multiplet group. The first 179 events correspond to the largest multiplet group (1), the next 38 belong to the second largest multiplet group (3). Note that the mutual similarity is higher for the second group. The remaining 19 groups are smaller, covering a smaller area in the matrix.

7.3 P-wave time repicking

After identification of all multiplet groups, the peak time lag in the crosscorrelation function between doublet pairs reveals relative arrival time inconsistencies, highlighting potential mispicks but also missing picks. In Figures 7.5a and 7.5b, two doublets are shown, with original time picks that visually look correct. However, Figure 7.5c shows both event waveforms extracted from two time windows based on the original P-wave picks. A minor inconsistency in picking is revealed as their onsets should be identical. By determining the time shift corresponding to the maximum peak in the crosscorrelation function I am able to correct these picking errors as shown in equation 4.5 and improve ultimately the event locations. Figure 7.5d displays the alignment of both waveforms after correction.

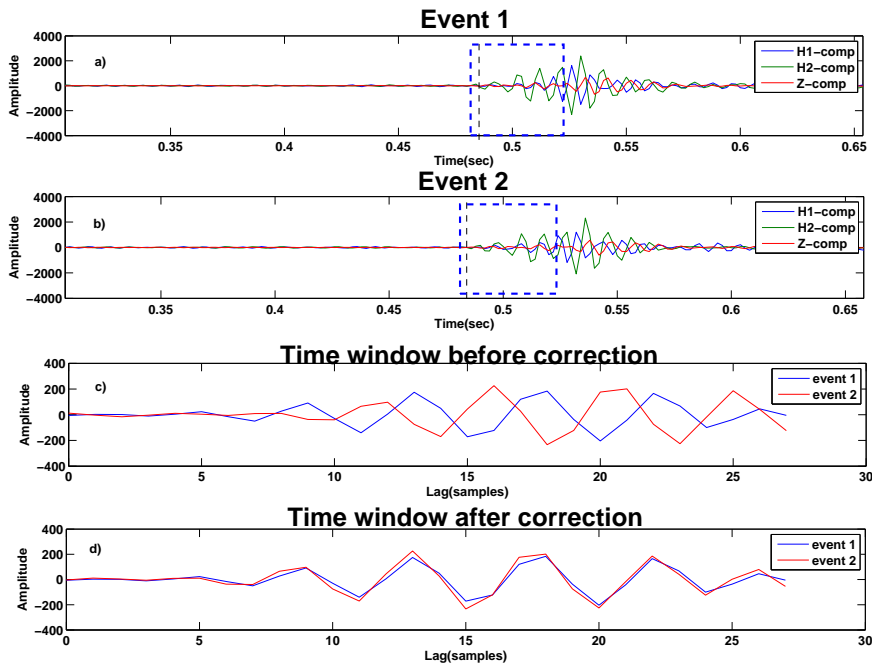


Figure 7.5: P-wave repicking method. a) and b) Two highly similar events recorded at one station. The crosscorrelation window is defined by the dashed blue line. c) Inconsistency in picking between similar events (one component shown). d) Waveform alignment after P-wave picking correction. Black dashed line: P-wave time picks.

Figure 7.6 shows the time delays, expressed as number of samples for doublets in multiplet

group 1. Most inconsistencies are limited to 10 samples (20 ms) which can produce spatial shifts in locations up to 75 m assuming an average P-wave velocity of 3700 m/s. As a result, 20 ms could be used as a default time pick uncertainty σ in equation 3.1. I am using a relative location method which means that I am interested in relative arrival time differences only. As a result, this procedure is applied regardless of which time pick is considered correct/incorrect. Equation 3.1 can not be used for absolute location.

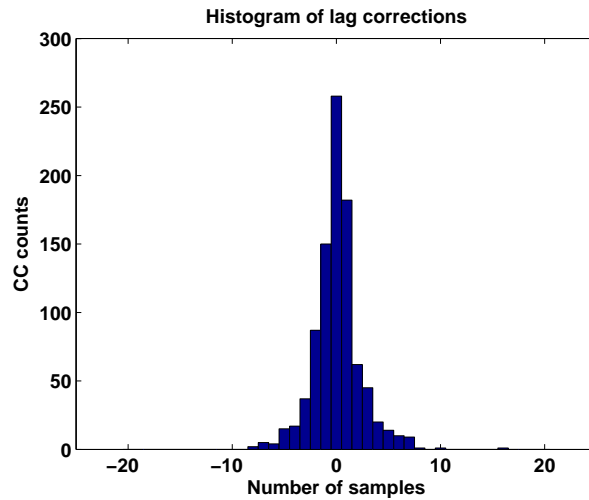


Figure 7.6: Histogram of time lags between doublets in multiplet group 1. A zero lag represents two events with time picks at the same onset. 10 (or -10) -sample represents two similar events whose time picks have a 10 (or -10) -sample shift. Thus, this histogram provides a quality control figure for the range in likely picking errors in a dataset and resulting hypocenter mislocations for a given velocity profile.

7.4 Weighting scheme

After correcting time shifts between doublet pairs, the influence of the various weighting schemes on the resulting event relocations when solving equation 4.11 needs to be assessed. Figures 7.7 and 7.8 show the results after applying different parameters for the distance weighting (equation 4.17). The most influential factors are the exponential a and maximum separation $dmax$. For instance, when $a=1$, there is a rapid decay with distance (Figure 7.7a). This appears very abrupt since only very close events will have high weights. Also, after relocation there are event pairs whose separation distances have been elongated to approximately 600 m (Figure 7.7c and 7.7f). Figure 7.7d shows some events scattered; these can be considered outliers produced by the weight selected. On the other hand, using $a=3$ (Figure 7.8a), doublets with large location errors have been moved closer to each other (Figure 7.8c and 7.8f). In Figure 7.8a, the weighting curve decays negligibly up to 200 m, creating a gentler reweighting. This is justified since Figure 7.8e indicates that events with correlations larger than 85% can be initially located up to 400 m apart. The harsher weighting for $a=1$ prevents accurate relocation of doublets with such large separation distances, yielding relocation artifacts (Figure 7.7d). It is important to set the distance weighting curve to allow for relocation of events mispositioned due to large picking errors (e.g., because of misidentification of the true P- or S-wave arrival). Value $dmax$ is set to 700 m since there are no event pairs that far apart.

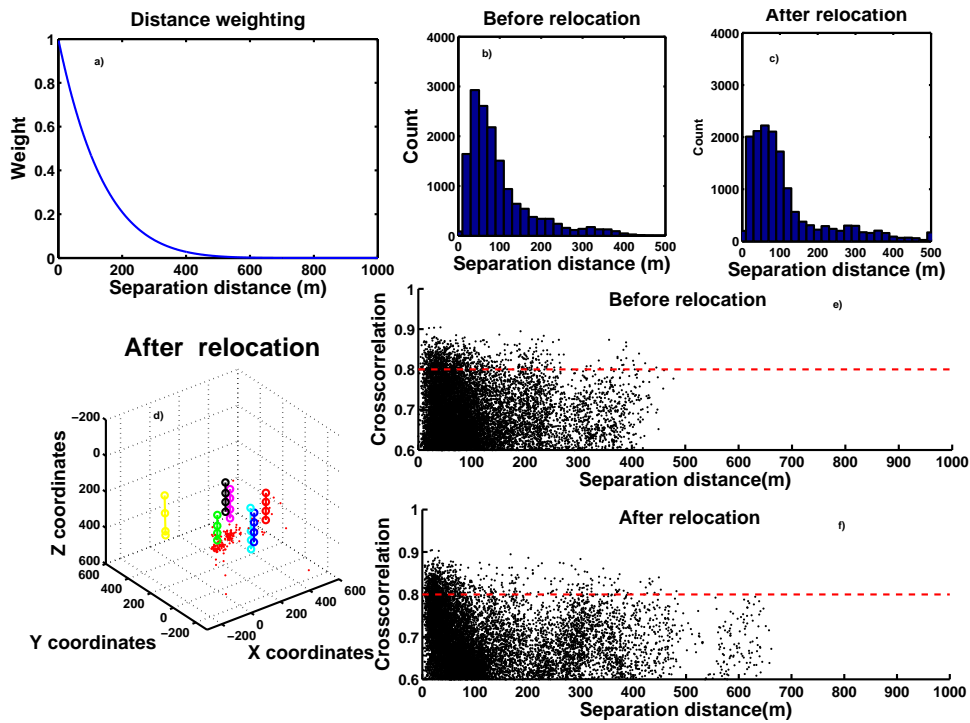


Figure 7.7: Distance weighting using $a=1$, $b=7$ and $d_{max}=700$ m applied to multiplet group 1. a) weighting as a function of inter-event distance. b) and c) histogram of separation distance between doublets before (left) and after (right) relocation, respectively. d) relocation using this weighting. e) Correlation vs distance plot (before relocation). f) Correlation vs distance plot (after relocation). The harsher reweighting scheme introduces relocation artifacts as high correlation doublets with large initial separations are not treated properly.

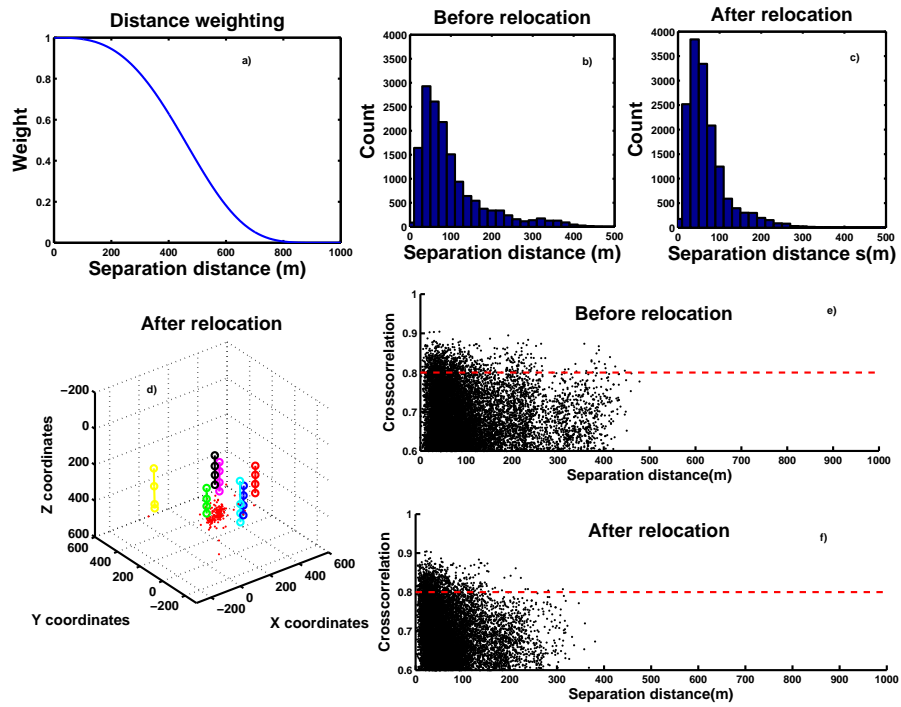


Figure 7.8: Distance weighting using $a=3$, $b=7$ and $d_{max}=700$ m applied to multiplet group 1. a) weighting as a function of inter-event distance. b) and c) histogram of separation distance between doublets before (left) and after (right) relocation, respectively. d) relocation using this weighting. e) Correlation vs distance plot (before relocation). f) Correlation vs distance plot (after relocation). The gentler reweighting scheme prevents relocation artifacts.

Figure 7.9 shows the two different crosscorrelation-based weighting curves using two different values for parameter d while keeping α fixed (equation 4.16). In the top left side, for reference, a simple quadratic relationship is defined as $d = 2$. This curve does not differentiate between highly correlated and less-correlated events; as a result, the assumptions of the method are not satisfied, as evidenced by a group of event pairs that have elongated their separations to 500 m (bottom left of Figure 7.9). In the top right, exponent $d=15$ produces a more appropriate curve since it greatly emphasizes correlation coefficients of 80% and higher. As a result, relocated events with high correlation values are more tightly clustered (bottom right of Figure 7.9). Figure 7.10 shows the microseismic event locations using $d=2$ and $d=15$. Note that for $d = 2$, this single multiplet group is separated into two clusters (left of Figure 7.10). However; one of the clusters has been relocated below 500 m, which is suspicious since the receivers array does not allow for a reasonable location constraint at that depth. Moreover, both clusters are still correlated when increasing correlation level.

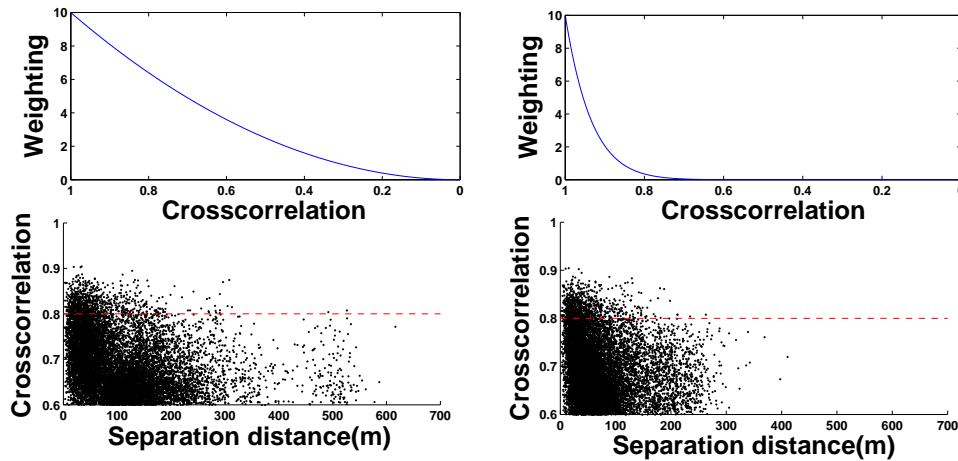


Figure 7.9: Crosscorrelation-based weighting, where $\alpha=10$. Left: Exponent $d=2$ is used. Right: Exponent $d=15$. The latter shows a rapid increase in the weights from event pairs correlated by more than 0.8 (Top right). Bottom row: resulting distance-correlation plots for all doublets in multiplet group 1 after relocation. The larger exponent reduces separation distances between events. Red dashed line: correlation threshold.

The chosen weighting scheme is thus $\alpha = 10$, $d = 15$ for the correlation-based weighting function and $a = 3$, $b=7$ and $d_{max}=700$ m for the distance-based weighting function (equations 4.16 and 4.17). Doublets with distances up to 200 m have approximately uniform weights. Between 200 and 700 m observations are down-weighted. Larger distances are dismissed using null weights. Likewise, doublets with correlations larger than 80% are greatly

emphasized.

Figure 7.11 shows the largest multiplet group (1), containing 179 events before and after relocation using the implemented weighting scheme. Note that the NW-SE cluster has been considerably tightened. Most events at the edges have been brought to the center. This is also observed in the depth profiles, where the seismicity has been collapsed to depths between 420 and 520 m. A few events are farther apart possibly due to poor event linking since mutual similarity is not enforced but a chain-like fashion is used to link event pairs. The final cluster size suggests this chain-like approach does not necessarily allow delineating single fractures or faults for this data set; however, this tightening of events fulfills my objective since similar shaped events should be collocated. Also, it demonstrates that assuming a homogeneous velocity model in the source area is enough to obtain seismic locations despite the complexity of the surroundings.

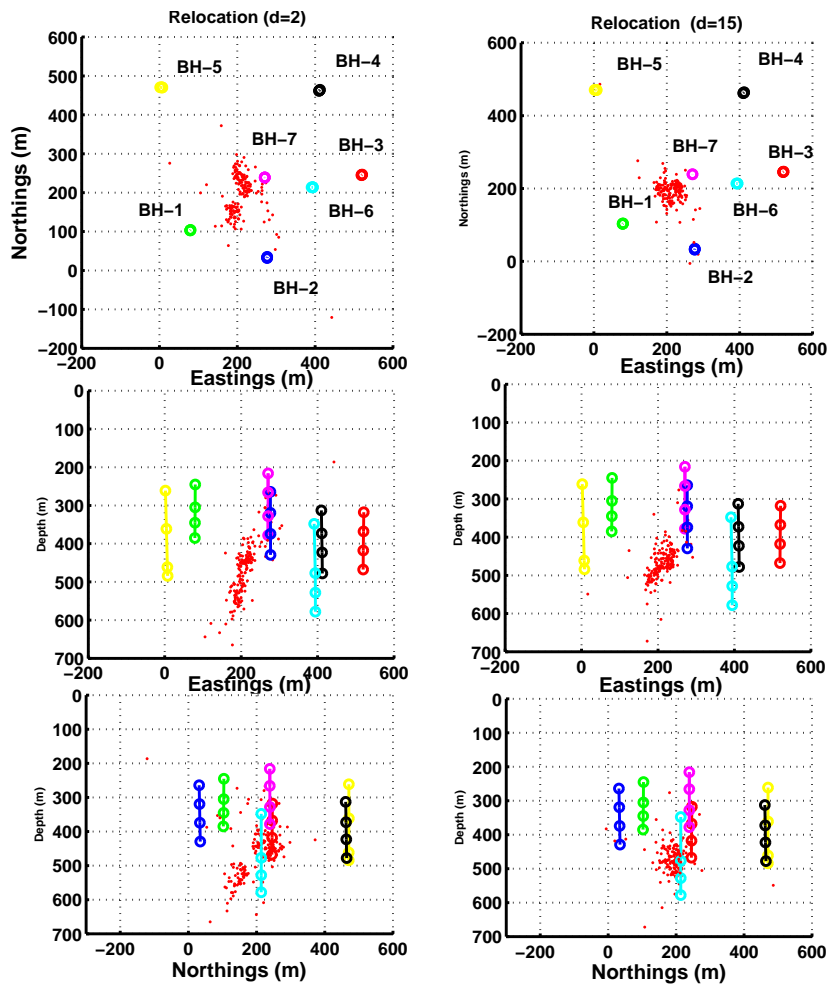


Figure 7.10: Relocation of multiplet group 1 using the exponential $d=2$ (left) and $d=15$ (right) defined in Figure 7.9. Both cases $\alpha=10$. From top to bottom: map view, and cross sections along W-E and S-N directions. When $d=2$ the group is divided into two subgroups which do not have

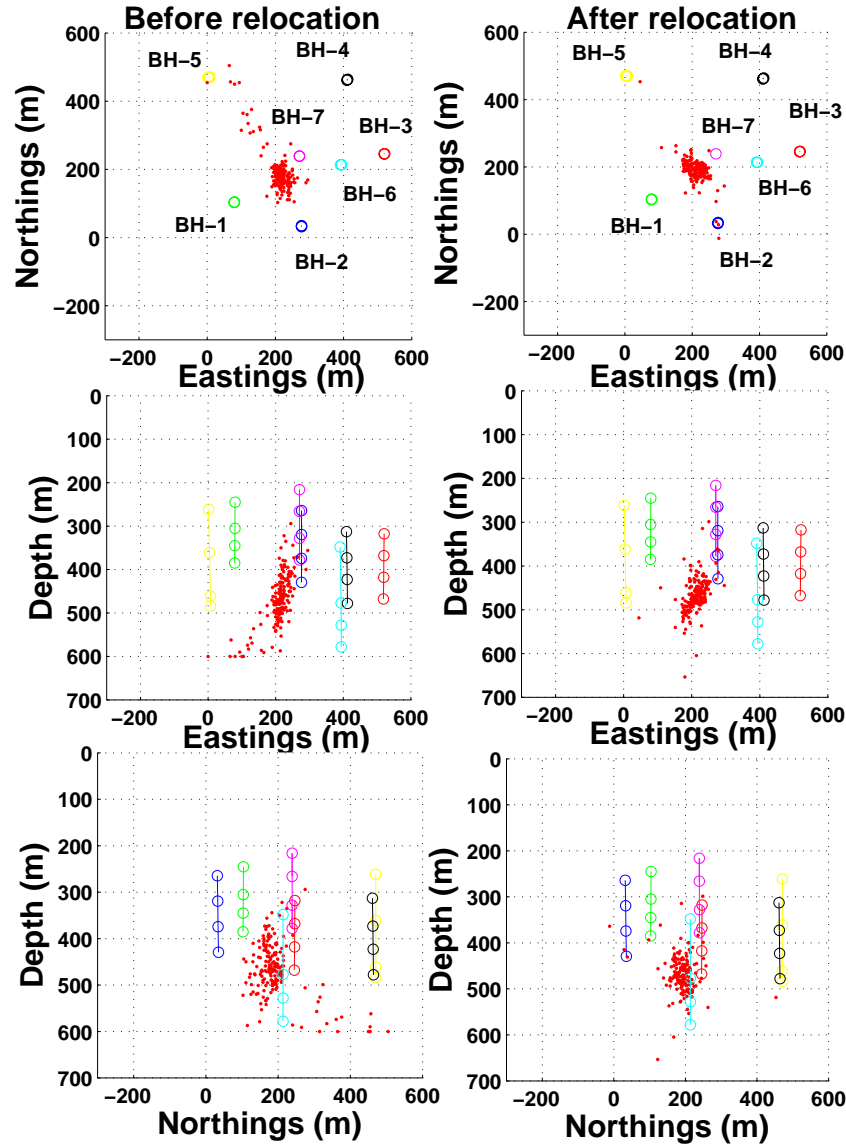


Figure 7.11: 179 events from multiplet group 1 before (left) and after (right) relocation using the double-difference method and the weighting scheme designed. From top to bottom: Map view, West-East and South-North cross-sections, respectively. After relocation, this main event cloud has been collapsed to depths between 420 and 520 m. Some events are farther apart from the cluster, which might be caused by poor event linking.

Figure 7.12 shows the crosscorrelation coefficients as a function of separation distances between event pairs before and after relocation for the multiplet group 1 (using both correlation and distance weights). Large correlation coefficients above 0.8 imply near-identical source locations. This plot can be used to quantify location uncertainty; as a result, highly correlated events with large separation distances suggest errors in the locations, probably due to mispicks. Separation distances for highly correlated events have been significantly reduced after relocation, indicating the success of the method. There are a few event pairs which have increased their separation distance after relocation, most likely due to poor linking between these pairs.

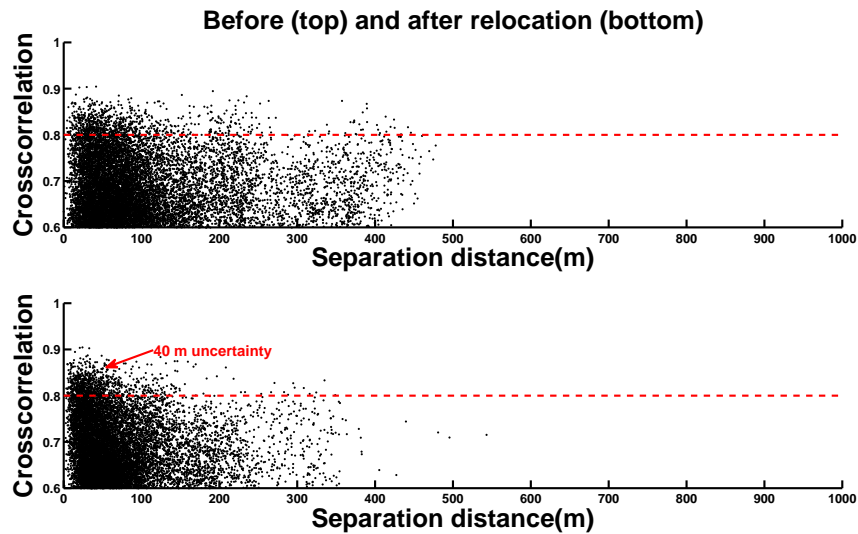


Figure 7.12: Normalized crosscorrelation coefficient versus event separation distance for all event pairs before (top) and after (bottom) relocation in multiplet group 1. A minimum correlation level of 0.8 (80%) was chosen to define multiplets. Note that after relocation, most events have tightened their distances, especially doublets. The red dashed line represents the minimum correlation level to consider two events as similar. The width of the densest doublets allows us to quantify the uncertainty of resulting locations (40 m).

Figure 7.13 shows the relocation vector (starting at initial locations) for multiplet group 1 where it is observed there are a couple of events that have moved at least 200 m closer to the cluster (longer vectors). The barycenter is fixed after relocation, so these vectors are not affected by the likely shift of the cluster after applying multiplet analysis.

Figure 7.14 shows more clearly the collapse of events in multiplet group 1 after relocation. Initially, events are separated on average by 107 m; after relocation, this is reduced to 86

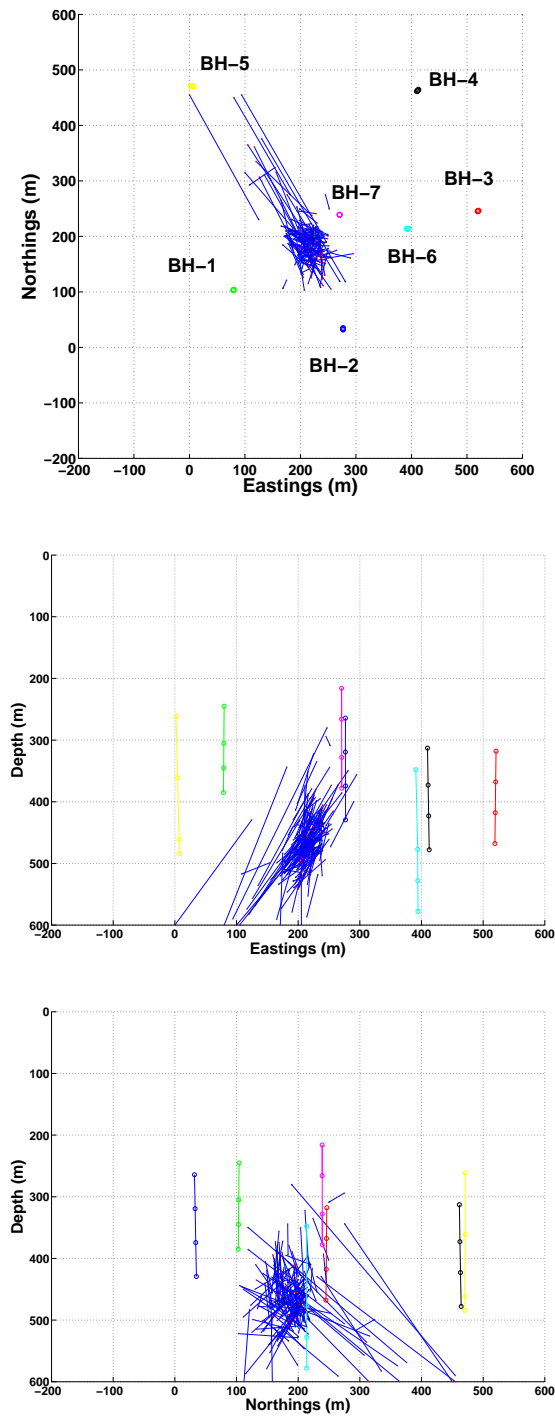


Figure 7.13: Relocation vector for multiplet group 1. Top: Map view. Middle: West-East cross-section. Bottom: South-North cross-section. Colored circles: Receiver boreholes. Blue arrow: Relocation vector for each event. Red points: initial locations. Blue points: relocations.

m. The average correlation within this group is 0.66, well below the threshold used (0.8), mainly due to the chain-like linkage implemented.

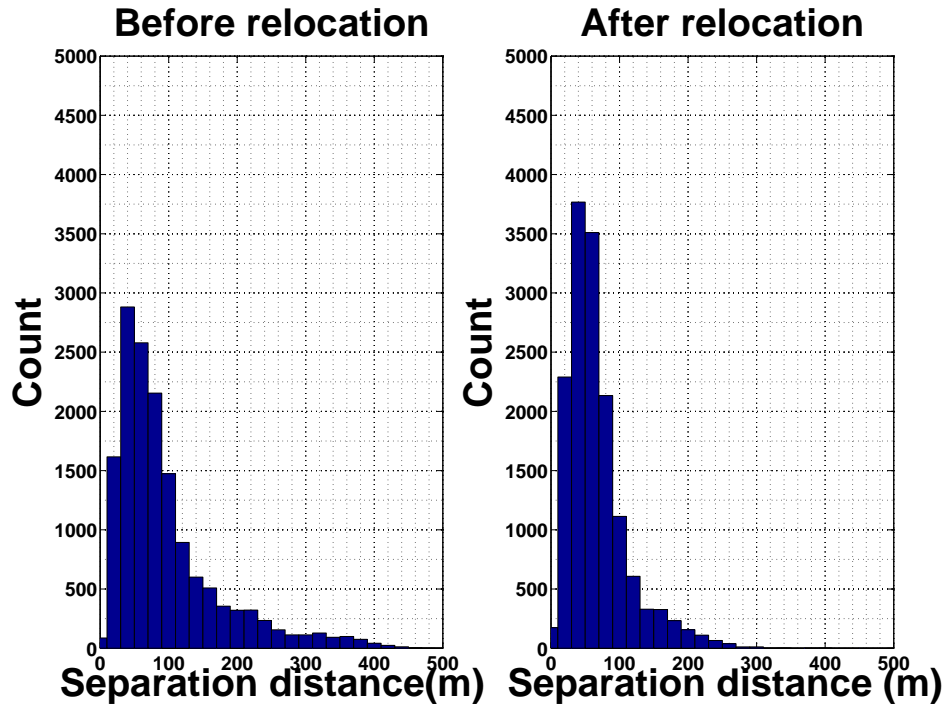


Figure 7.14: Histogram of separation distance between events in multiplet group 1 before (left) and after (right) relocation. The average separation distance between multiplets have reduced from 107 m to 86 m.

Figure 7.15 shows multiplet group 3 with 38 events, using the same weighting parameters as previously defined. In this case, events are located at the center of the array and between 400 and 500 m depth. Despite group 3 is not correlated with group 1, both clusters overlap at locations close to the main shaft and main tunnels. This can occur as there might be several seismic sources in the same area, especially in mining complex structures. Figure 7.16 shows the correlation values as a function of separation distance, where some event pairs 79% correlated are initially located almost 200 m apart (top of Figure 7.15), but after relocation, they have moved to 125 m or closer (bottom of Figure 7.15). Here, the exponential relationship between correlation and inter-event distance is not clearly visible due to the reduced amount of events. Finally, Figure 7.17 shows the corresponding relocation vectors for multiplet group 3 where doublets have collapsed on average by 6 m.

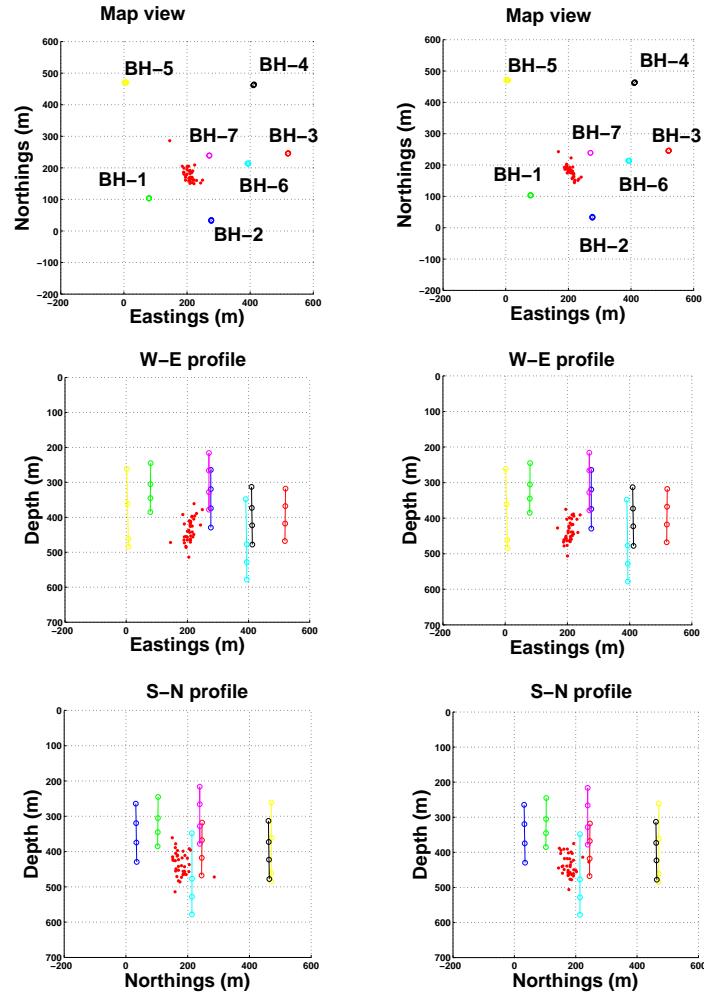


Figure 7.15: 38 events from multiplet group 3 before (left) and after (right) relocation using the double-difference method and the weighting scheme designed. From top to bottom: Map view, West-East and South-North cross-sections, respectively. After relocation, this main event cloud has been confined to depths between 420 and 520 m. Despite group 3 is not correlated with group 1, both clusters overlap.

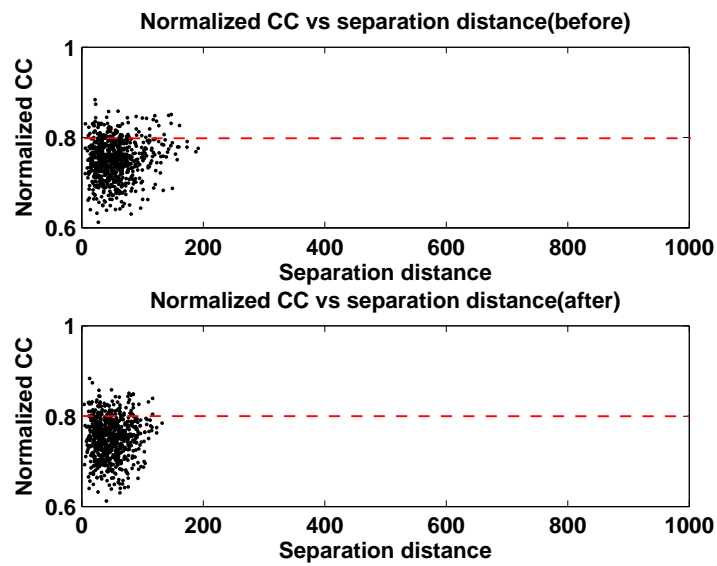


Figure 7.16: Normalized crosscorrelation coefficient versus event separation distance for all event pairs before (top) and after (bottom) relocation in multiplet group 3. A minimum correlation level of 0.8 (80%) was chosen to define multiplets. Note that after relocation, most events have tightened their distances, especially doublets. The red dashed line represents the correlation threshold.

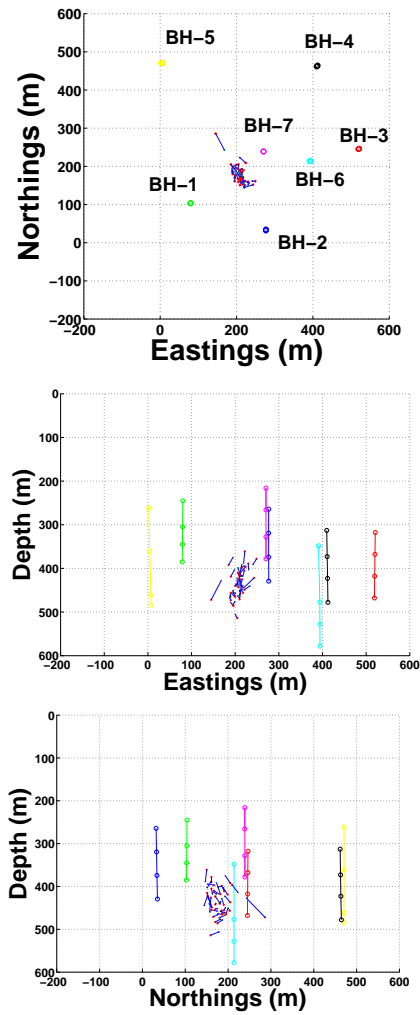


Figure 7.17: Relocation vector for multiplet group 3. Top: Map view. Middle: West-East cross-section. Bottom: South-North cross-section. Colored circles: Receiver boreholes. Blue arrow: Relocation vector for each event. Red points: initial locations. Blue points: relocations.

Figure 7.18 shows all 21 multiplet groups before (left) and after (right) relocation. There is no clear spatial differentiation between multiplet groups. In fact, most groups are located at the center of the array, with groups 1 and 3 plotted in red and orange, respectively.

In the next chapter, potential implications of the detected seismicity are discussed.

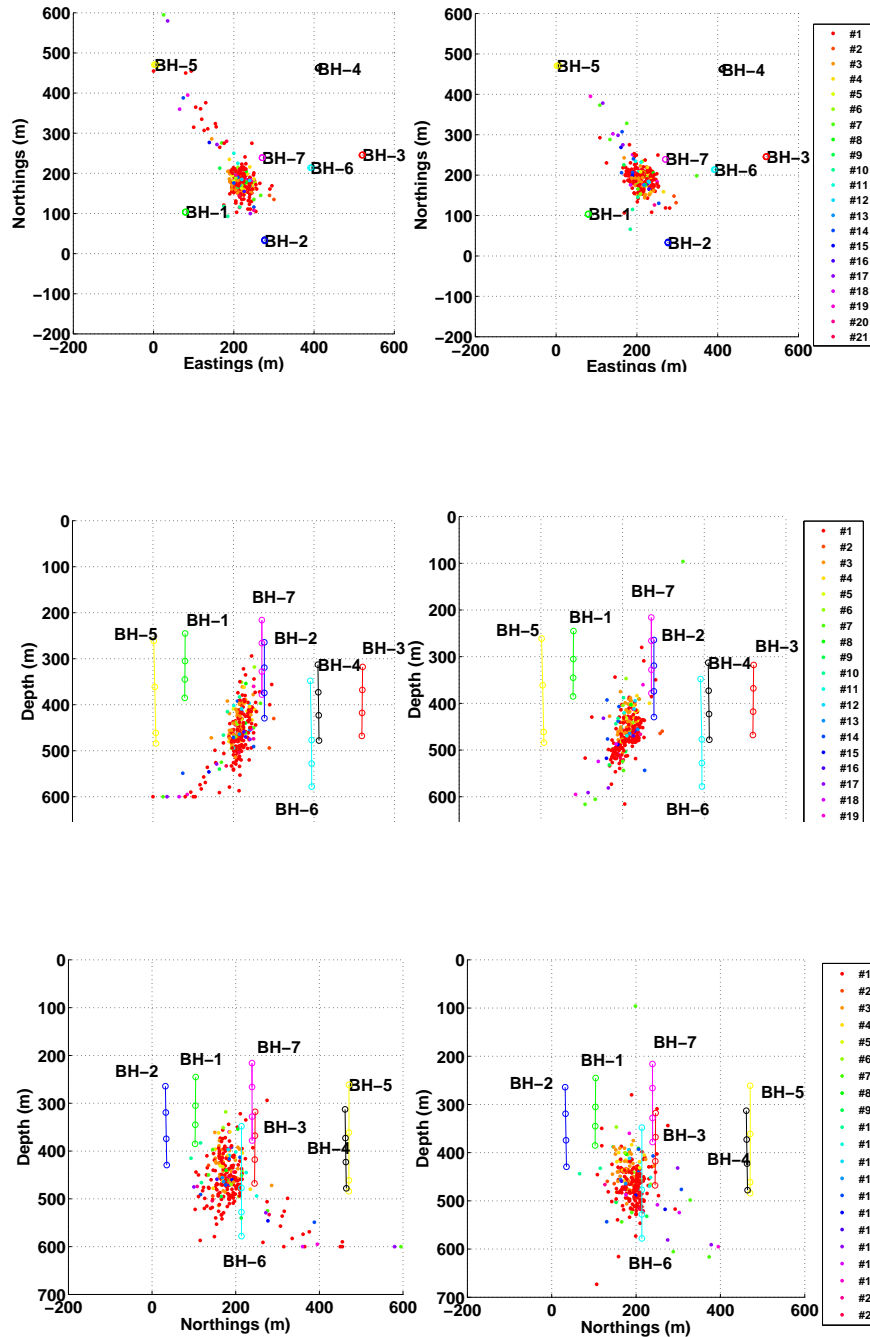


Figure 7.18: Initial (left) vs relocation (right) for all 21 multiplet groups found. Top: Map view. Middle: West-East cross-section. Bottom: South-North cross-section. Colored open circles: Receiver boreholes.

CHAPTER 8

Discussion.

8.1 Mining data interpretation

8.1.1 Pattern of multiplets occurrence over time

Figure 8.1 is a Gantt chart showing the occurrence of the 21 multiplet groups found during January 2011. In general, multiplet groups 1, 3 and 4 largely dominate the seismicity. In the first week (top of Figure), groups 1 to 10 occur. During the second week (middle Figure), there is a more quiet seismicity, except for groups 1 and 3. In the third week (bottom Figure), group 1 continues dominating the seismicity, and new smaller groups are generated, groups 14 to 21. This seismicity seems to happen at specific hours of the day, as evidenced in days such as the 5th, 7th and 20th of January. In principle, they could be induced by blasting activities, lifting operations along the shaft or depletion as a consequence of rock removal. In other words, the seismicity variations seem systematic and might correlate with scheduled mining operations within the mine and a causal link could be established, as there are no other mines nearby that could trigger seismicity and tidal effects of close lakes are discarded.

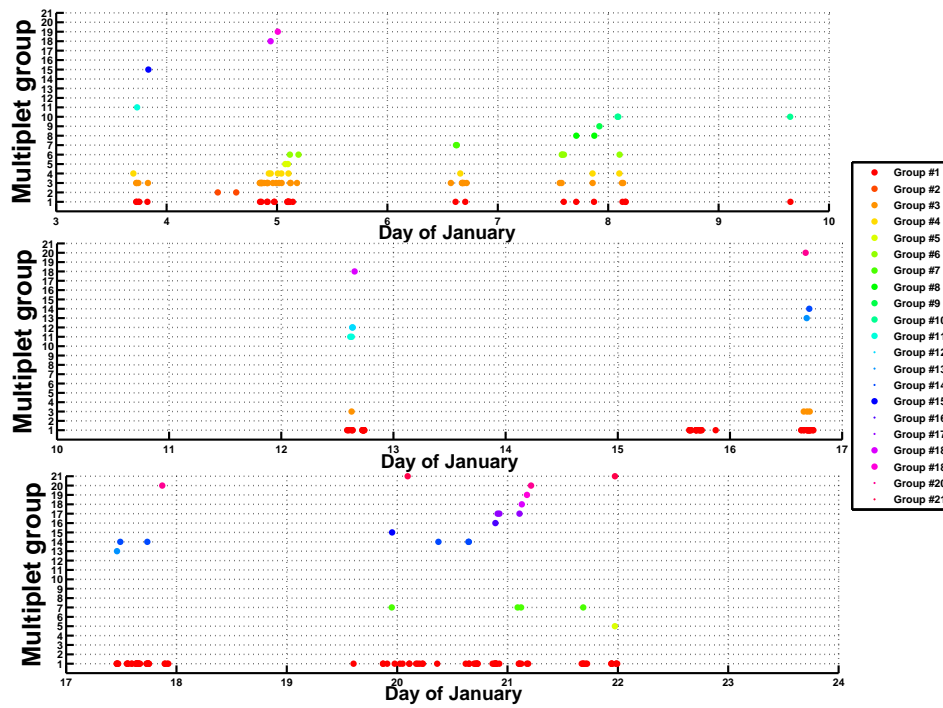


Figure 8.1: Gantt chart showing multiplets occurrence during January 2011. Each multiplet group (21 in total) is shown with a different color. Most events from the largest multiplet group (red) occur during the third week of January, compared to the second largest (orange) which occurs during the first two weeks. During January 25-31 no multiplets are detected.

8.1.2 Blasting activities

A major concern during mining operations is the possibility that blasts induce seismicity [Young et al., 1992, Shuifer et al., 2012]. Figure 8.2 compares the waveforms recorded from a microseismic event and a blast at a common station. The signal from a blast has notable features such as the very strong energy of the P-wave arrival, shorter duration and broader bandwidth (Figure 8.3). Given the high-energy arrivals, these blasts are very easy to detect using conventional algorithms [Allen, 1978, Sleeman and van Eck, 1999].

Figure 8.4 shows the temporal distribution of triggered files and blasting activities during January 2011. A total of 11 blasts occurred during the first three weeks. They are usually preceded by a high number of recorded seismograms, possibly triggered by purely surface activities and cultural noise. This is more evident in the hourly plot of Figure 8.5, showing the occurrence of triggered files during January 4th, where it is visible that after the blasting activities occur (red vertical lines around 7 a.m. or 7 p.m.), there is no triggered files during the next two to three hours. There is no available information on the amount of explosive used for the blasts; however, the absence of seismicity is unexpected since they are likely to stimulate rock mass slip along neighboring zones of weakness or fracturing intact rock, thus inducing microseismic events. This absence of seismicity also suggests that the mining operations stopped for safety reasons. In mining operations, after large events or blasting activities, there might be an increase of seismicity that over time decays to noise levels. As a result, if events had been induced, by applying an empirical relationship such as Omori's law, the rate of induced events as a function of time following each blast could be determined and the size of stimulated area.

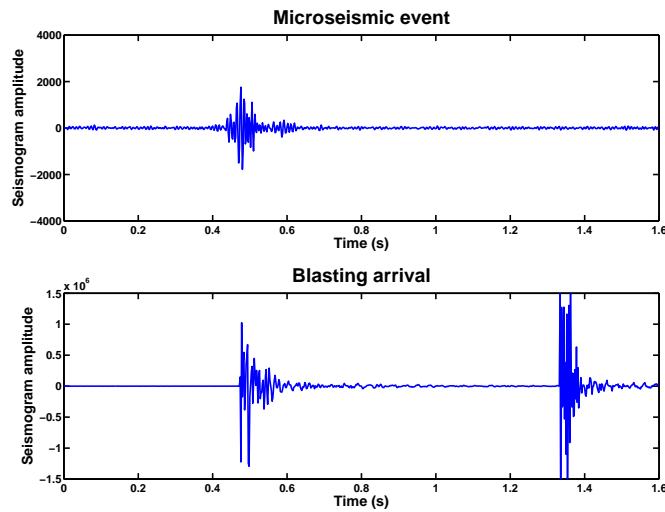


Figure 8.2: Top: Seismogram of a microseismic event. Bottom: Seismogram showing two blast detonations. Signals from both blasts show very strong P-wave arrivals and shorter duration.

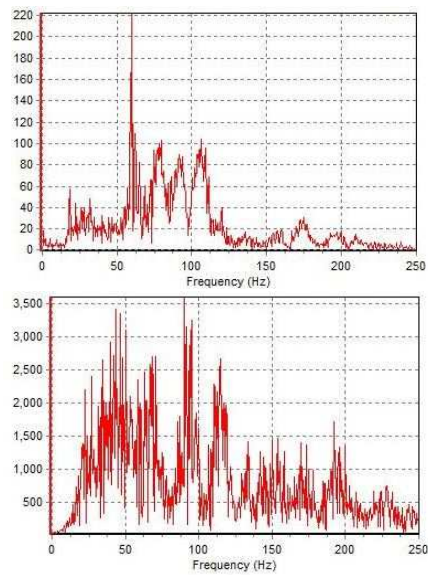


Figure 8.3: Amplitude spectrum comparison. Top: Raw microseismic signal. Bottom: Blast signal. The blast signal has a broader spectrum and higher energy than the microseismic event.

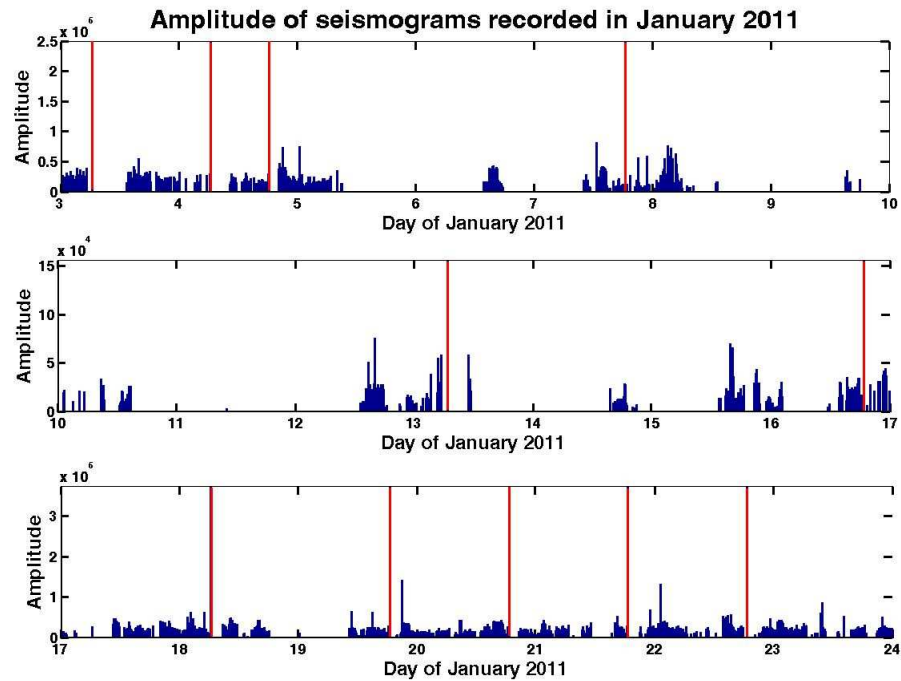


Figure 8.4: Triggered files during January 2011. Top: January 3rd to 9th. Middle: January 10th to the 16th. Bottom: January 17th to 23rd. The vertical red lines represent the times of the blasting activities. After each blast occurrence, there are barely any triggered files for at least two hours, except cases such as January 7th and 17th. The amplitude axis varies in each plot to better highlight the blasts from the rest of the triggered files.

Figure 8.6 shows the hourly distribution of all MS events, three main multiplet groups and blasting activities. Most of the seismicity occurs between 1 p.m. and 6 p.m., which suggests they are likely to be induced by routine mining operations. Neither these multiplets nor the rest of events seem to correlate with the blasting activities, which are scheduled around 6 a.m. and 6 p.m. since immediately after there is no significant detected seismicity.

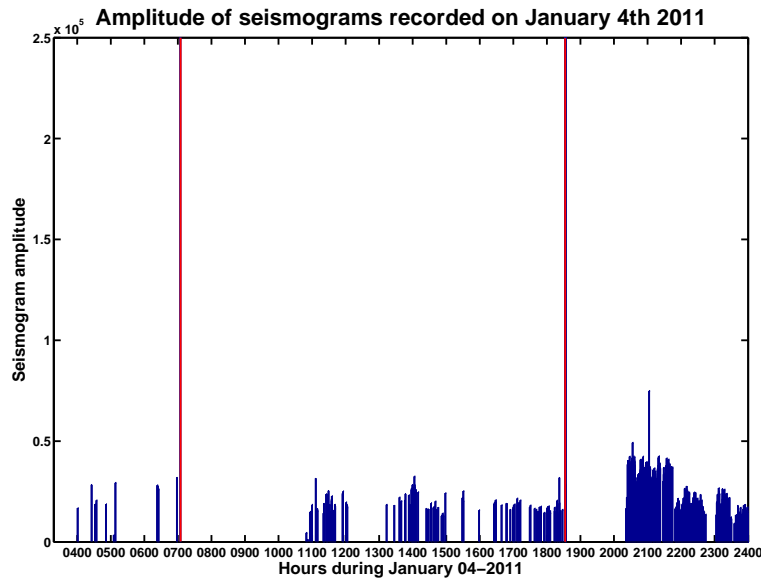


Figure 8.5: Triggered files during January 4th, 2011. The blasting activities (red vertical lines) start around 6:30 a.m. and 6:30 p.m. After each blast, no arrival triggers the recording equipment, suggesting no seismicity is induced by the blasts.

Tunnels where blasting activities occurred are listed in Table 8.1 and Figure 8.7 shows the correlation matrix for all 16 different blasts listed. There are correlation values up to 0.75 (shown as orange colors) and each of these high values represent a pairs of blasts occurring at similar tunnels. Despite 75% is not a very high correlation value, this simple matrix plot allows tracking blast positions, especially for cases where no coordinates are reported. Some arrivals due to blasts are not picked at common receivers (especially due to dead traces), producing a null value (blue color) such as the blasts occurred on January 1st and 19th.

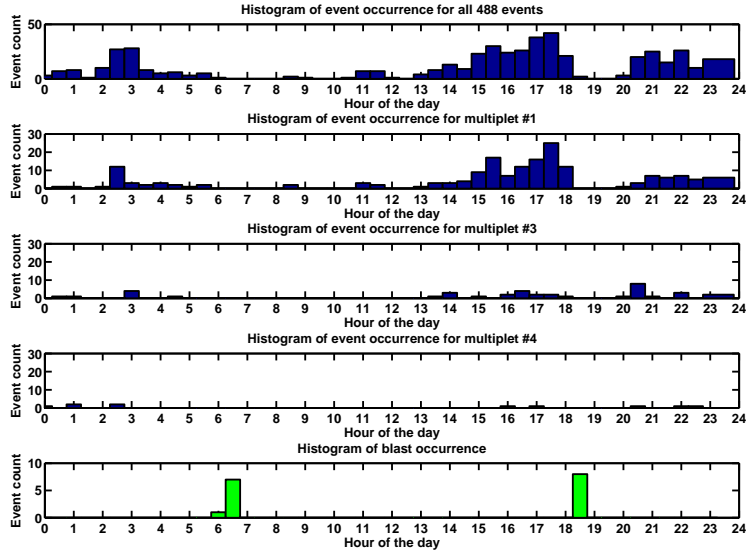


Figure 8.6: Histogram of hourly seismicity and blasting times during January 2011. From top to bottom: 488 MS events recorded, multiplet groups 1, 3, 4 and blasting activities, respectively. Two features are visible: i) the seismicity seem to occur at specific times of the day and ii) blasting activities are scheduled around 6 a.m. and 6 p.m. and they do not seem to induce microseismic events.

January 2011	Depth(m)	Time	Rock volume(m^3)
01	480-a	07:00	112
02	500-a	19:00	77
03	480-b	07:00	95
04	500-a	07:00	77
04	480-d	19:00	70
07	480-a	19:00	30
13	480-a	07:00	174
16	480-b	07:00	860
18	480-c	07:00	114
19	500-b	19:00	36
20	480-d	19:00	74
21	480-b	19:00	102
22	480-a	19:00	174
24	500-c	07:00	111
25	480-c	07:00	99
26	480-d	07:00	112

Table 8.1: Master advance of blasting activities during January 2011.

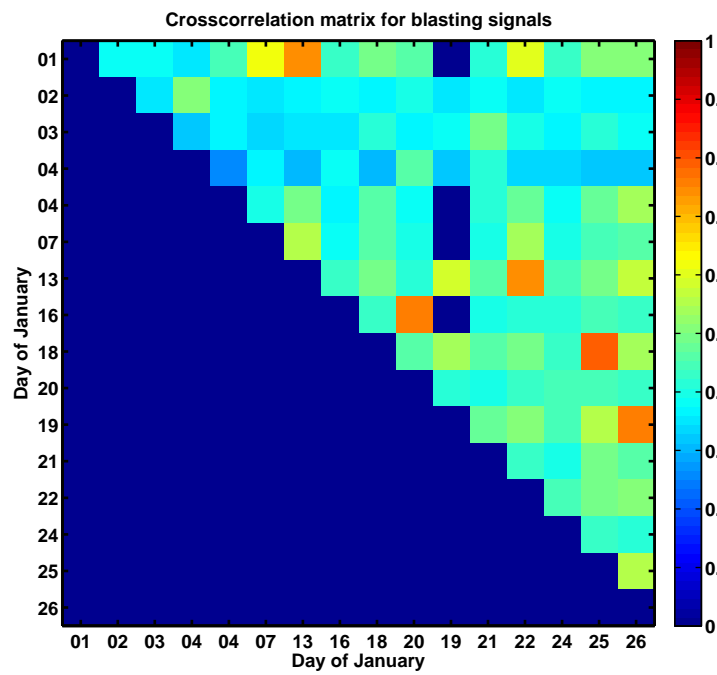


Figure 8.7: Crosscorrelation matrix of 16 different seismograms recording blasting activities listed in Table 8.1. Red cell: perfect correlation. Blue cell: null correlation.

8.1.3 Interpretation of largest multiplet groups

One of the questions when monitoring mining activities is whether we are able to discriminate between natural microseismic events and man-made events? In principle, multiplet analysis could provide insights since they represent different groups of source mechanisms, thus differences in amplitude between multiplet groups could indicate that some groups are associated to specific sources. In Figure 8.8, amplitudes of the three main multiplet groups are shown; however, no significant differences are observed. This is also observed in Figure 8.9 where histograms of S-to-P ratios for the three main groups are displayed. Despite that group 1 has the largest mean, 3.06, suggesting a higher shearing component; there is no significant difference that would allow for a relative interpretation of the types of sources generating these events. Studies on effects of tunnels has shown they can impact S-to-P amplitude ratios, especially when these scatterers are close to the source [Imhof and Tokso, 2000]. If integrated with moment tensor information, it can aid in the assessment of which source mechanism model better fits these S-to-P amplitude ratio values [Rutledge et al., 2004].

The pattern of located seismicity of group 1 shown in Figure 8.10 is the deepest among all groups, and likely relates to activities carried out in the main 480 m and 500 m levels, the main working tunnels in the mine. This group has its barycenter located 20 m to the North of shaft 1, approximately 100 m away from the orebody (see Figure 5.3 in chapter 5). There are events located at depths >500 m which are less constrained due to the shallower placement of the receiver array and also farther events due to poor linking with most doublets in the group.

The microseismic activity of group 3 in Figure 8.11 shows events located above the 420 m and 465 m tunnels and below the 420 m tunnel. Events above tunnels could be generated due to subsidence after rock removal. To confirm this, the located seismicity should be integrated with geomechanical analysis including moment tensor inversion and resulting focal mechanisms. It is also important to know the degree and extent of potential excavation damaged zones (EDZ). Especially in this mine, since they may create pathways for groundwater which raises concerns for new episodes of flooding. This multiplet cloud is located close to multiplet group 1 and the aforementioned Gantt chart shows a temporal correlation pattern between groups 1 and 3, which might suggest a connectivity/microseismic migration between them. As a result, more accurate methods such as displacement monitoring, borehole observations can be applied, which are able to better identify the EDZ, compared to microseismic monitoring and subsequent seismic locations. In other words, knowledge of these rock deformation processes and further study on the evolution of stress states within

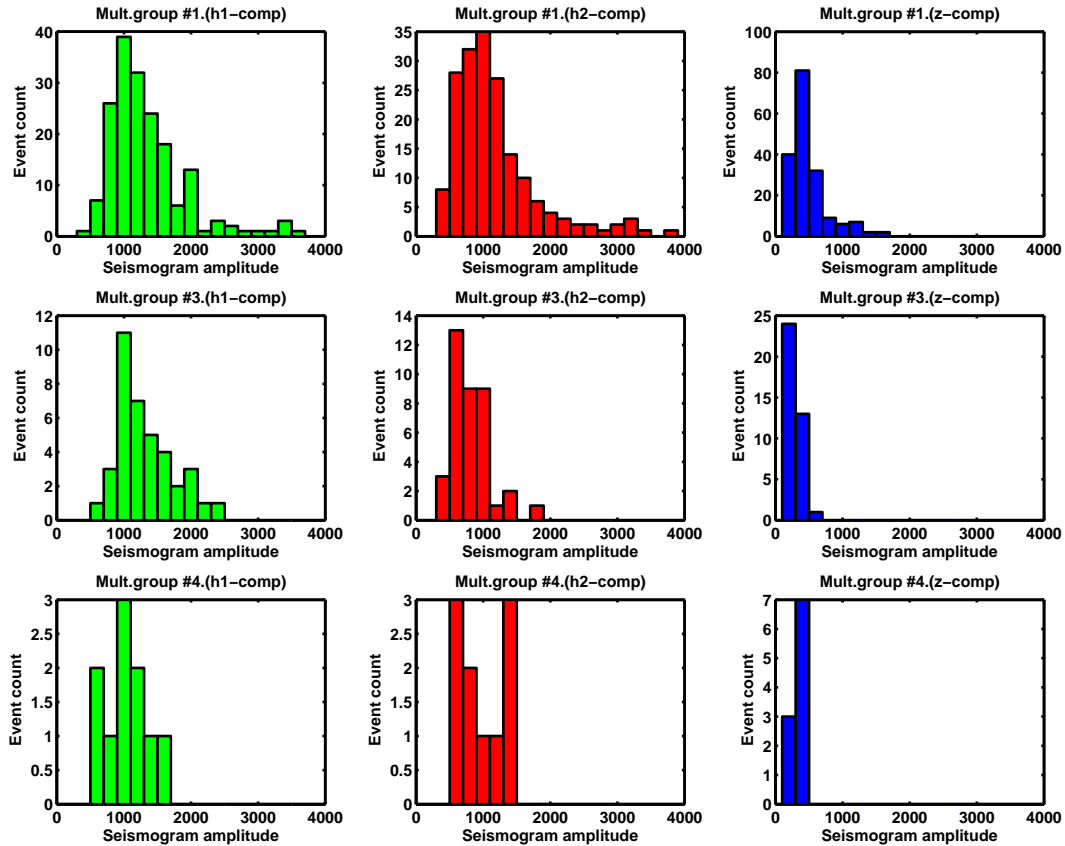


Figure 8.8: Histogram of amplitudes for the three largest multiplet groups. Top: Multiplet group 1. Middle: Multiplet group 3. Bottom: Multiplet group 4. Bar color: Green (h1-component), red (h2-component) and blue (vertical component). There are no significant differences in amplitude between multiplet groups.

the mine and how soft/weaker rocks are affected is necessary for the purpose of better planning at the mine. A second hypothesis suggests this seismicity has been induced by the passage of the lift along shaft 1, given this cluster is also close to it.

The pattern of seismicity of group 4 shown in Figure 8.12 appears to be entirely related to the activities in the 420 m level. According to Bishop et al. [2012], this tunnel is intended to be backfilled. Unfortunately, the provided mine reports do not provide whether there were activities along the 420 m level during January 2011.

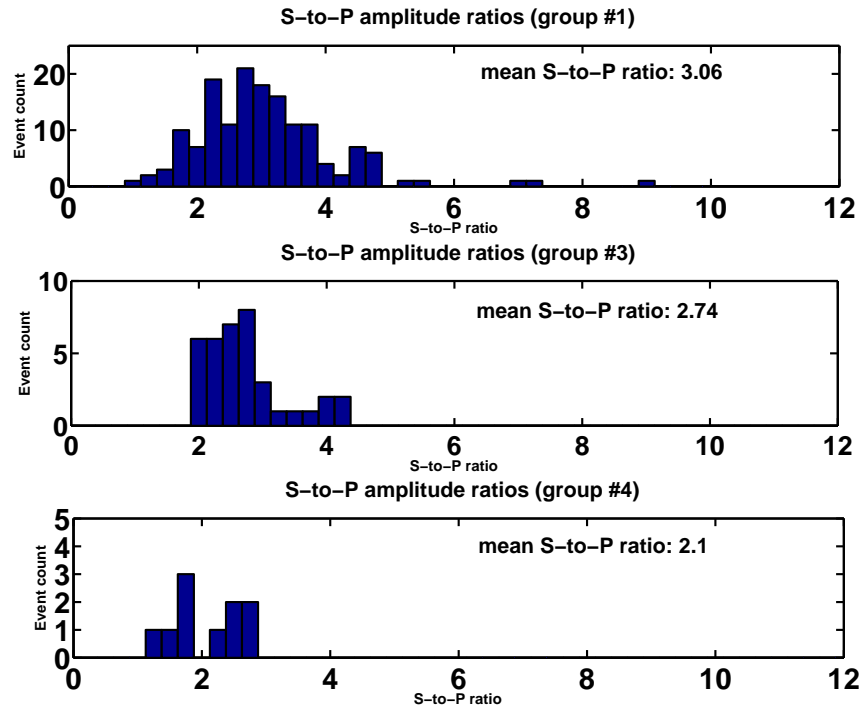


Figure 8.9: S-to-P amplitude ratios. Top: group 1. Middle: group 3. Bottom: group 4.

Despite that the locations are improved compared to the absolute initial locations, the seismicity is still diffuse in the main clusters. This seismicity may be affected by the presence of tunnels which can delay travel times due to diffraction effects and add location errors [Maxwell and Young, 1998]. The implications of this propagation effects are usually ignored during mining-induced projects but they should be taken into account especially in mines with dense presence of these heterogeneities.

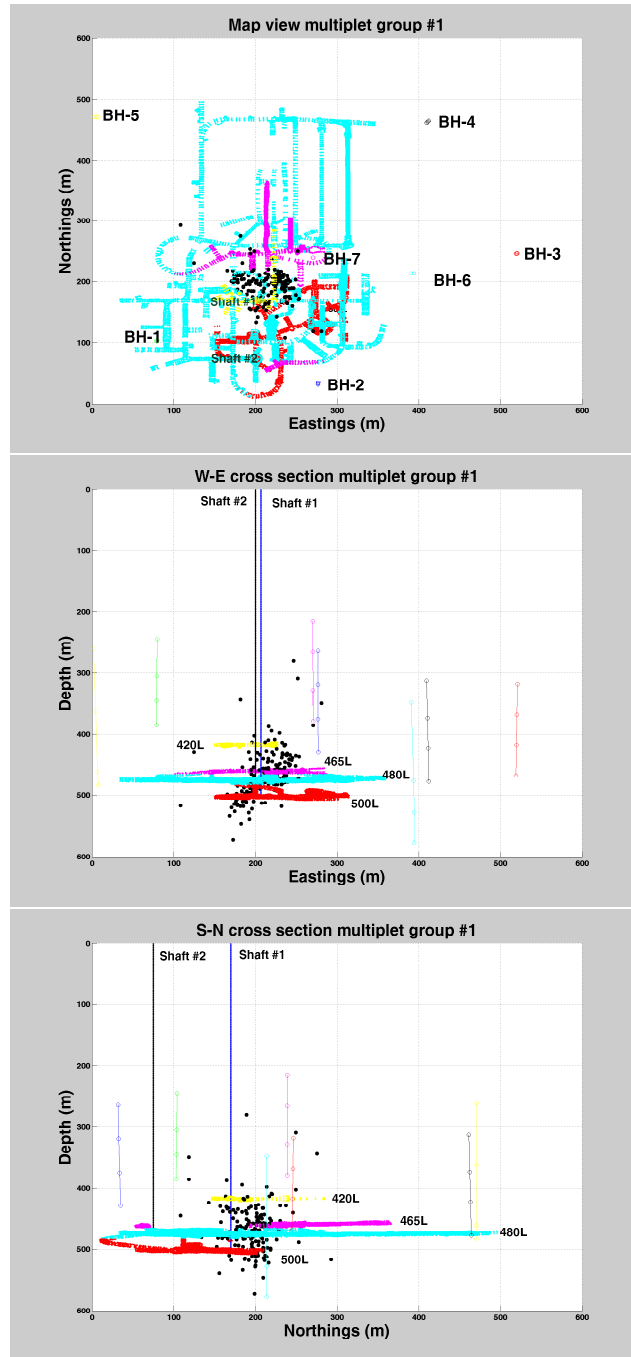


Figure 8.10: 3-D view of multiplet group 1 (179 events). Top: Map view. Middle: West-East cross-section. Bottom: South-North cross-section. The seismicity is clustered 20 m North to the shaft 1, and closer to the orebody location. Some events are farther apart as a result of poor multiplet linking. Open colored circles: Receiver stations. Colors of tunnels: 420 m (yellow), 465 m (pink), 480 m (blue) and 500 m (red).

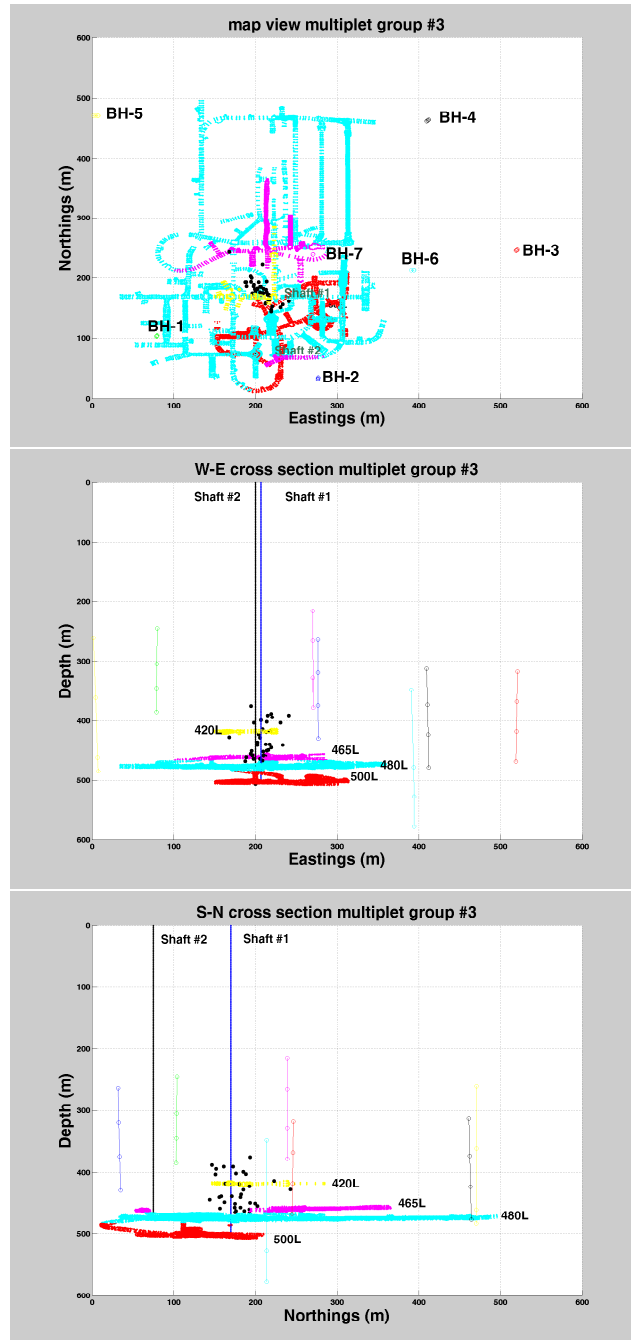


Figure 8.11: 3-D view of multiplet group 3 (38 events). Top: Map view. Middle: West-East cross-section. Bottom: South-North cross-section. This cluster surrounds shaft 1, between the 420 m and 465 m tunnels. Open colored circles: Receiver stations. Colors of tunnels: 420 m (yellow), 465 m (pink), 480 m (blue) and 500 m (red).

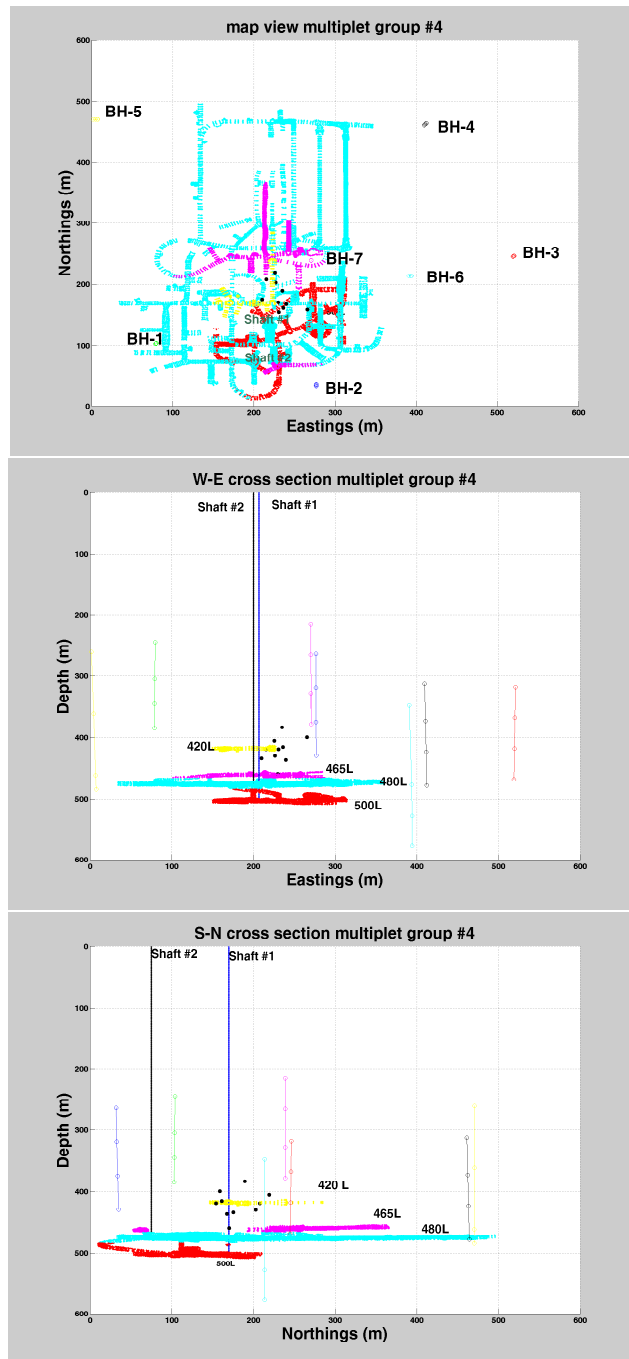


Figure 8.12: 3-D view of multiplet group 4 (10 events). Top: Map view. Middle: West-East cross-section. Bottom: South-North cross-section. The seismicity is clustered along the 420 m level. Open colored circles: Receiver stations. Colors of tunnels: 420 m (yellow), 465 m (pink), 480 m (blue) and 500 m (red).

8.2 Pre-processing workflow

The introduced pre-processing workflow ultimately determines event location using travel times only. This requires a receiver array that provides enough illumination (at least four receiver boreholes). P-wave polarizations are not estimated in this workflow. Nevertheless; by rotating the two horizontal components to radial and transverse components, both P- and S-wave arrivals might show more clear waveforms. S-wave travel times are not picked since they are usually obscured by the P-wave coda and their waveforms are more affected by cavities, although their addition could better constrain hypocentral distances. The implemented STA/LTA method discards a considerable amount of false alarms. Also, attention is required to not skip useful events, especially since a long STA window might not be sensitive to sudden increases in amplitude signal. An autoregressive method is applied for P-wave onset picking; although careful quality control is necessary to correct for visible time picking errors. Doublets might be unclear in their raw seismograms; however, after applying a band-pass filter these events show nearly-identical waveforms, as suggested by Geller and Mueller [1980]. The raw data are also highly contaminated at 60 Hz due to electrical noise. This can particularly impact crosscorrelation measurements, since these high peaks overwhelm desired event signals. These peaks are also removed during the filtering process.

For the initial locations a P-wave homogeneous velocity model is assumed, since a 1-D layered isotropic velocity model produces higher residuals between observed and calculated travel times and there are artifacts clearly related to this velocity model. The provided velocity model has a sudden increase at 500 m depth, which does not correspond to the depth of the unconformity (≈ 460 m) separating sandstones from basement rock. Calibration shots with their origin times are not available, information which would have been useful to confirm a better representation of the final velocity structure. The choice of a homogeneous velocity model is justified since I am interested in relative relocations and the approach accounts for shared ray paths irrespective of the complexity of the velocity model.

Regarding the lookup table, its application is recommended when using 1-D or 3-D velocity models, as these models require longer computation times to calculate source-receiver travel times. For example, the grid search is 80 and 230 times (node spacing of 100 and 20 m, respectively) faster when using such table and assuming a 1-D velocity model. When assuming a homogeneous velocity model, its implementation is not required, as it does not speed up the process. The grid search applied on this case study performs on a $600 \text{ m} \times 600 \text{ m} \times 600 \text{ m}$ volume with a 5 m spacing between nodes. For higher resolution in less computing time, a regional search based on neighborhood algorithms is recommended to locate the

most likely epicenter zone, followed by a finer search using a smaller bin size. This size can also depend on the desired resolution; for instance, if higher resolution is needed vertically, a smaller length of the bin in that direction is recommended.

8.3 Doublet definition

The doublet definition in real data is highly subjective as two events will never be 100% similar due to the presence of noise. In this case study, a minimum correlation of 0.8 (80%) is chosen, which is sufficiently low to create multiplets, but sufficiently high to differentiate between different groups. A chain-like similarity approach is used. Although applied for a mining case, this approach is also recommended for projects such as hydraulic fracturing where it is expected that similar faults and fractures are activated during stimulation. Weighting each component by its maximum amplitude is very useful as it emphasizes high-energy arrivals.

Although this doublet definition is subjective and may depend on factors such as data bandwidth, receiver geometry or SNR, it is a sufficient approach to meet the assumption of the double-difference method.

8.4 Relocation algorithm

A main difference of this method compared to the first double-difference algorithm is the forward modeling. Waldhauser and Ellsworth [2000] solve it using a 1-D layered P-wave velocity model especially because correlated and uncorrelated data are relatively relocated simultaneously, whereas in this thesis, a homogeneous velocity model is used to relocate groups of correlated data (see appendix for description of partial derivatives determination). If a more complex structure is assumed, please refer to Lee and Stewart [1981] which describe how to compute travel times and partial derivatives for heterogeneous media. It is also recommended to take into account the effect of cavities for the travel time calculations.

This relative relocation method is largely insensitive to inaccuracies in the local, homogeneous velocity model except for relative distances as these will be expressed in an expanding or contracting microseismic cloud for respective underestimated or overestimated velocities (Figures 4.12 and 4.11). In other words, events along a planar fault plane remain distributed within a plane, yet its spatial extent may vary. On the other hand, initial absolute locations

are likely spread out over a 3D cloud due to velocity and picking inaccuracies.

Accuracy of event locations depends strongly on picking quality. The complete data set shows an average SNR just above 3, which represent a medium-quality signal, as most waveforms show considerably clear onsets. It is shown that the implemented cross-correlation method corrects for potential mispicks and also acts as a quality control measure. For instance, Figure 7.6 shows that 28% of the time picks are perfectly consistent, and 65% are within ± 1 sample (2 ms). These time picking errors can be converted to location errors assuming a velocity profile, or simply to provide a first approximation of data uncertainties σ in equation 3.1.

Correlation values certainly contain information on relative distance between similar events; as a result, correlation versus distance plots also reveal location uncertainties as seen in Figure 7.12, where most mutual doublets in multiplet group #1 have separation distances < 40 m.

The constrain in the barycenter is a major step in this algorithm. As demonstrated in synthetic tests (Figure 4.7), this relative location method does not necessarily improve the absolute microseismic locations. To reduce this, the cloud barycenter is fixed before and after relocation, assuming that the initial absolute locations reflect a first approximate picture of the seismicity and there are no consistent errors shifting the locations.

A disadvantage of the double-difference method is that the system can become very large if all event pairs are used, unlike master-event relocation technique. To circumvent this, it is suggested to increase the minimum number of links between event pairs, so only strong event pairs are considered. Also, the minimum correlation threshold can be increased. Obviously, there is a trade-off between severity of the implemented thresholding and allowing for more flexibility in the inversion system permitting more constraints on the final relocations. Additionally, the maximum number of neighboring events can be reduced so that only those with higher correlation values (or smaller inter-event distances) are used.

8.5 Weighting scheme

Relocation results depend strongly on the chosen weighting scheme, based on the minimum correlation level and the maximum separation distance. It is recommended to set correlation

weights in equation 4.16 such that observations from pairs of events with correlations below a set threshold are downweighted. Likewise the distance weights in equation 4.17 are to be set such that they do not exclude any highly correlated doublets. In the case of multiplet group 1, distances up to 200 m have a near-uniform weight and those beyond 700 m are discarded. Likewise, correlation coefficients larger than 0.8 are greatly stressed. Obviously, these values may change with each application depending on acquisition geometries, signal to noise ratios and how rapid correlation values decay as a function of separation distances for a specific area. In addition, normalization of the derivative matrix is vital, a step which is usually overlooked, since its omission can significantly bias locations and origin times.

CHAPTER 9

Conclusions.

Microseismic monitoring has gained importance as a tool to provide information on underground processes occurring during mining operations. A proper location technique is necessary since knowledge of areas prone to generate either man-made or natural earthquakes is key for management and development of the mine and for evaluation of potential hazards during operations. In this thesis, I describe a relative relocation technique based on waveform similarity assessment, in order to detect and relocate microseismic events originated in the same source region with near-identical source mechanisms. This relocation technique is applied as a post-processing stage after a basic pre-processing workflow appropriate when good azimuthal coverage is provided by the source-receiver geometry. It has been demonstrated that picking errors are a major source of event mislocations, but they can be corrected through crosscorrelation methods. The double-difference method applied independently for multiplet groups significantly reduces errors in relative event locations by collapsing multiplet clusters. The assumption of a homogeneous velocity model greatly simplifies velocity model building; yet it is warranted since the methodology implies largely overlapping source-receiver raypaths. Additionally, I demonstrate the implemented weighting scheme is crucial in the inversion procedure for event location as the assumption of "ray-path similarity" is to be honored even for doublets separated due to large picking errors. This leads to some subjective choices such as the minimum correlation coefficient and maximum allowed inter-event distance. Nonetheless, by linking similar events in a chain-like fashion ultimately uncertainty in relative event locations is greatly reduced.

The distribution of seismicity shows a temporal pattern suggesting microseismic events occur during certain times along the day. The improved locations of the main clusters are associated to mining activities, especially along the main 420, 465, 480 and 500 m levels.

The two largest groups are located close to one another, suggesting a possible connectivity between them. This hypothesis is also supported since the S-to-P wave amplitude ratios are similar. Unexpectedly, the blasting activities do not induce seismic activity, at least during the next two to three hours after each blast. It becomes necessary to analyze subsequent months to detect potential fractured areas close to the blast locations.

Moreover, crossplots of correlation values versus event distances and histograms of time-lags of highly correlated events serve as useful quality control measures both of absolute locations and subsequent relative relocations. As a consequence, multiplet analysis and double-difference relocations can greatly aid in quality assessment of time picks and hypocenters, as well as considerably facilitate any geologic interpretations.

9.1 Further research

- Include uncorrelated events into the system of equations described in 4.11, i.e., microseismic events that do not belong to any multiplet group. Despite the weighting scheme takes into account inter-event distances, this scheme might fail for larger separations, and this is the reason why a 1-D or 3-D isotropic velocity model is recommended.
- Use the existing microseismic data with subsequent months for seismic tomography studies. This could provide a better representation of changing conditions within the rock mass that is being mined.
- Apply this relocation technique to a single borehole receiver array. As shown in the synthetic tests, the double-difference technique relies on a distribution of receivers that allows for a good azimuthal coverage. When a single borehole receiver array is used, a change in the coordinate system to a cylindrical system to include P- and S-wave polarization measurements can improve location accuracy.
- Complement the relocated seismicity with geomechanical models to better understand the relationship between stress changes and detected microseismicity.
- Study the propagation effects of the tunnels and underground excavations. They can delay travel times and also change amplitudes and waveforms, affecting location accuracy and interpretation of the stress state and seismic energy release.

Bibliography

- Agh, R Cieplicki, L Eisner, and T Aboot. “Correlation Detection and Location for Microseismic Events Induced by Hydraulic Fracturing.” *EAGE*. 2012, 4–7.
- Akram, Jubran and David Eaton. “Adaptive microseismic event detection and automatic time picking.” *2012 CSEG Annual Convention..* 2012, 1–5.
- Allen, Rex. “Automatic Earthquake Recognition and Timing from Single Traces.” *Bulletin of the Seismological Society of America* 68 (1978): 1521–1532.
- Arrowsmith, Stephen J. and Leo Eisner. “A technique for identifying microseismic multiplets and application to the Valhall field, North Sea.” *Geophysics* 71 (2006): V31–V40.
- Artman, Brad, Igor Podladtchikov, and Ben Witten. “Source location using time-reverse imaging.” *Geophysical Prospecting* (2010): 861–873.
- Baisch, S, L Ceranna, and H P Harjes. “Earthquake Cluster: What Can We Learn from Waveform Similarity?.” *Bulletin of the Seismological Society of America* 98 (2008): 2806–2814.
- Bickle, Mike, Andy Chadwick, Herbert E. Huppert, Mark Hallworth, and Sarah Lyle. “Modelling carbon dioxide accumulation at Sleipner: Implications for underground carbon storage.” *Earth and Planetary Science Letters* 255 (March 2007): 164–176.
- Bishop, Scott, Grant Goddard, Alain Mainville, and Eric Paulsen. Cigar Lake Project Northern Saskatchewan, Canada. Technical report, 2012.
- Block, L.V., C.H_i Cheng, M.C_i Fehler, and W. Scott Phillips. “Seismic imaging using microearthquakes induced by hydraulic fracturing.” *Geophysics* 59 (1994): 102–112.
- Butt, Stephen, Derek Apel, and Peter Calder. “Analysis of High Frequency Microseismicity Recorded at an Underground Hardrock Mine.” *Pure and Applied Geophysics* 150 (1997): 693–704.

- Castellanos, Fernando and Mirko van der Baan. "High-accuracy relative event locations using a combined multiplet analysis and the double-difference inversion." *SEG Technical Program Expanded Abstracts*. 2012, 1–5.
- Castellanos, Fernando and Mirko van der Baan. "Microseismic Event Locations using the Double-Difference Algorithm." *CSEG Recorder* (2013).
- Chambers, Kit, J Kendall, Sverre Brandsberg-dahl, and Jose Rueda. "Testing the ability of surface arrays to monitor microseismic activity." *Geophysical Prospecting* (2010): 821–830.
- Cipolla, C, S Maxwell, M Mack, and R Downie. "SPE 144067 A Practical Guide to Interpreting Microseismic Measurements." *SPE International* (2011): 14–16.
- Cook, N.G.W. "The seismic location of rockbursts." *5th Rock Mechanics Symposium*. Oxford: Pergamon Press, 1963, 493–518.
- Cumming, G. L. and J. Rimsaite. "Isotopic studies of lead-depleted pitchblende, secondary radioactive minerals, and sulphides from the Rabbit Lake uranium deposit, Saskatchewan." *Canadian Journal of Earth Sciences* 16 (September 1979): 1702–1715.
- Davis, E, C Wright, S Demetrius, Pinnacle Technologies, J Choi, and G Craley. "Precise Tiltmeter Subsidence Monitoring Enhances Reservoir Management." *SPE International*. 2000.
- De Meersman, K., J. Kendall, and M. van der Baan. "The 1998 Valhall microseismic data set: An integrated study of relocated sources, seismic multiplets, and S-wave splitting." *Geophysics* 74 (2009): B183–B195.
- Deichmann, Nicholas and Mariano Garcia-Fernandez. "Rupture geometry from high-precision relative hypocentre locations of microearthquake clusters." *Geophysical Journal International* 110 (September 1992): 501–517.
- Earle, Paul S and Peter M Shearer. "Characterization of Global Seismograms Using an Automatic-Picking Algorithm." *Bulletin of the Seismological Society of America* 84 (1994): 366–376.
- Eisner, Leo, B. J. Hulse, Peter Duncan, Dana Jurick, Heigl Werner, and William Keller. "Comparison of surface and borehole locations of induced seismicity." *Geophysical Prospecting* 58 (September 2010): 809–820.
- Eisner, Leo, Heigl Werner, and William Keller. "Uncertainties in passive seismic monitoring." *The Leading Edge* (2009).

- Fayek, Mostafa and T Kurtis Kyser. "Characterization of multiple fluid-flow events and rare-Earth-element mobility associated with formation of unconformity-type uranium deposits in the Athabasca Basin, Saskatchewan." *The Canadian Mineralogist* 35 (1997).
- Fehler, Michael, Andy Jupe, and Hiroshi Asanuma. "More Than Cloud : New techniques for characterizing reservoir structure using induced seismicity." *The Leading Edge* (2001).
- Fischer, T., S. Hainzl, L. Eisner, S. a. Shapiro, and J. Le Calvez. "Microseismic signatures of hydraulic fracture growth in sediment formations: Observations and modeling." *Journal of Geophysical Research* 113 (February 2008): 1–12.
- Fréchet, J. *Sismogenese et doublets sismiques*. PhD thesis, L'Universite Scientifique et Medicale de Grenoble, 1985.
- Fremont, Marie-Jose and Stephen Malone. "High Precision Relative Locations of Earthquakes at Mount St. Helens, Washington." *Journal of Geophysical Research* 92 (1987): 10223–10236.
- Geller, Robert and Charles Mueller. "Four Similar Earthquakes in Central California." *Geophysical Research Letters* 7 (1980): 821–824.
- Gibbons, Steven J. and Frode Ringdal. "The detection of low magnitude seismic events using array-based waveform correlation." *Geophysical Journal International* 165 (April 2006): 149–166.
- Got, J.-L., J. Fréchet, and Fred W. Klein. "Deep fault plane geometry inferred from multiplet relative relocation beneath the south flank of Kilauea." *Journal of Geophysical Research* 99 (1994): 15375–15386.
- Han, Lejia. *Microseismic Monitoring and Hypocenter Location*. PhD thesis, University of Calgary, 2010.
- Imhof, Matthias G and M Nafi Tokso. "Scattering from Tunnels near Sources and their Effect on Seismic Signatures of Explosions." *Bulletin of the Seismological Society of America* (2000): 229–242.
- Jansky, Jaromir, Vladimir Plicka, and Leo Eisner. "Feasibility of joint 1D velocity model and event location inversion by the Neighbourhood algorithm." *Geophysical Prospecting* 58 (March 2010): 229–234.
- Jones, Michael and Richard Parker. "Microseismic Event Location Accuracy Enhancement using Anisotropic Velocity Models." *CSEG annual convention*. 2010, 1–4.
- Kocon, Ken and Mirko van der Baan. Multiplet relocation in a heavy oil field using the double difference method. Technical report, 2011.

- Lee, W.H.K and S.W Stewart. *Principles and applications of microearthquake networks*. Ed. Barry Saltzman. 1981.
- Lomax, Anthony, Alberto Michelini, and Andrew Curtis. 2008 : 2449–2473.
- Maxwell, S C, J Du, J Shemeta, U Zimmer, N Boroumand, L G Griffin, and Pinnacle Technologies. “Monitoring SAGD Steam Injection Using Microseismicity and Tiltmeters.” *SPE International*. 2007, 1–7.
- Maxwell, S C, T I Urbancic, N Steinsberger, Devon Energy, and R Zinno. “Microseismic Imaging of Hydraulic Fracture Complexity in the Barnett Shale.” *SPE International*. 2002, 1–9.
- Maxwell, S.C. and T.I. Urbancic. “Real-Time 4D Reservoir Characterization Using Passive Seismic Data.” *SPE International*. Society of Petroleum Engineers, September 2002.
- Maxwell, S.C., T.I. Urbancic, M. Prince, and C. Demerling. “Passive Imaging of Seismic Deformation Associated With Steam Injection in Western Canada.” *SPE International*. Society of Petroleum Engineers, October 2003, 1–8.
- Maxwell, S.C and R.P Young. “Propagation effects of an underground excavation.” *Tectonophysics* 289 (April 1998): 17–30.
- Maxwell, Shawn. “An introduction to this special section : Microseismic.” *The Leading Edge* (2010): 2010.
- Maxwell, Shawn. “Microseismic : Growth born from success.” *The Leading Edge* (2010): 338–343.
- Menke, William. “Using Waveform Similarity to Constrain Earthquake Locations.” *Bulletin of the Seismological Society of America* 89 (1999): 1143–1146.
- Michelet, Sophie and M. Nafi Toksöz. “Fracture mapping in the Soultz-sous-Forêts geothermal field using microearthquake locations.” *Journal of Geophysical Research* 112 (July 2007): 1–14.
- Moriya, Hirokazu, Koji Nagano, and Hiroaki Niitsuma. “Precise source location of AE doublets by spectral matrix analysis of triaxial hodogram.” *Geophysics* 59 (1994).
- Moriya, Hirokazu, Hiroaki Niitsuma, and Roy Baria. “Multiplet-Clustering Analysis Reveals Structural Details within the Seismic Cloud at the Soultz Geothermal Field , France.” *Bulletin of the Seismological Society of America* 93 (2003): 1606–1620.

- Murase, Masayuki, Takeo Ito, Yoshinari Hayashi, Takeshi Sagiya, Fumiaki Kimata, and Hidefumi Watanabe. "Spatio-temporal distribution of magma intrusions inducing repeated earthquake swarms off the east coast of the Izu peninsula, central Japan, for 1973-1998." *Journal of Volcanology and Geothermal Research* 193 (June 2010): 25–36.
- Paige, C.C. and M.A. Saunders. "LSQR: Sparse linear equations and least squares problems." *ACM Transactions on Mathematical Software* 8 (1982): 195–209.
- Pandey, M. R., R. P. Tandukar, J. P. Avouac, J. Lavé, and J. P. Massot. "Interseismic strain accumulation on the Himalayan crustal ramp (Nepal)." *Geophysical Research Letters* 22 (April 1995): 751–754.
- Pavlis, Gary. "Appraising relative earthquake location errors." *Bulletin of the Seismological Society of America* 82 (1992): 836–859.
- Pearson, Chris. "The Relationship Between Microseismicity and High Pore Pressures During Hydraulic Stimulation Experiments in Low Permeability Granitic Rocks." *Journal of Geophysical Research* 86 (1981): 7855–7864.
- Pei, Donghong, John Quirein, Bruce Cornish, Erkan Ay, Steve Zannoni, Calvin Kessler, and Will Pettit. "Layered Models With and Without Perforation Timing Measurements." *SPE International* (2008).
- Philippe, S and J R Lancelot. "Formation and evolution of the Cigar Lake uranium deposit based on U- Pb and K - Ar isotope systematics." *Canadian Journal of Earth Sciences* 30 (1993): 720–730.
- Phillips, W., T. Fairbanks, J. Rutledge, and D. Anderson. "Induced Microearthquake Patterns and Oil-Producing Fracture Systems in the Austin Chalk." *Tectonophysics* 289 (1989): 153–169.
- Phillips, W. Scott, Leigh S. House, and Michael C. Fehler. "Detailed joint structure in a geothermal reservoir from studies of induced microearthquake clusters." *Journal of Geophysical Research* 102 (1997): 11745.
- Pike, Kimberly and David W. Eaton. "Velocity model construction for microseismic event location." *Microseismic Industry Consortium Book Report*. . 2012. chapter 10, 1–17.
- Poupinet, G., W. L. Ellsworth, and J. Frechet. "Monitoring Velocity Variations in the Crust Using Earthquake Doublets: An Application to the Calaveras Fault, California." *Journal of Geophysical Research* 89 (1984): 5719–5731.
- Raleigh, C.B., J.H. Healy, and J.D. Bredehoeft. "An experiment in earthquake control at Rangely, Colorado.." *Science* (1976): 1230–1237.

- Read, R.S. “20 years of excavation response studies at AECL’s Underground Research Laboratory.” *International Journal of Rock Mechanics and Mining Sciences* 41 (December 2004): 1251–1275.
- Richardson, Eliza and Thomas H Jordan. “Seismicity in Deep Gold Mines of South Africa : Implications for Tectonic Earthquakes.” *Bulletin of the Seismological Society of America* 92 (2002): 1766–1782.
- Roman, Diana C. and Katharine V. Cashman. “The origin of volcano-tectonic earthquake swarms.” *Geological Society of America* 34 (2006): 457.
- Rowe, C A, R C Aster, W S Phillips, R.H Jones, B Borchers, and Michael C. Fehler. “Using automated, high-precision repacking to improve delineation of microseismic structures at the Soultz geothermal reservoir.” *Pure and Applied Geophysics* (2002): 593–596.
- Rubin, Allan M. and Dominique Gillard. “Dike-induced earthquakes: Theoretical considerations.” *Journal of Geophysical Research* 103 (1998): 10017.
- Rutledge, J T, W S Phillips, and M J Mayerhofer. “Faulting Induced by Forced Fluid Injection and Fluid Flow Forced by Faulting : An Interpretation of Hydraulic-Fracture Microseismicity , Carthage Cotton Valley Gas Field , Texas.” *Bulletin of the Seismological Society of America* 94 (2004): 1817–1830.
- Sambridge, Malcolm. “Exploring multidimensional landscapes without a map.” *Inverse* 14 (June 1998): 427–440.
- Scarfi, L., H. Langer, and A. Scaltrito. “Relocation of microearthquake swarms in the Peloritani mountains - implications on the interpretation of seismotectonic patterns in NE Sicily, Italy.” *Geophysical Journal International* 163 (October 2005): 225–237.
- Shaw, Peter and Jian Lin. “Causes and Consequences of Variations in Faulting Style at the Mid-Atlantic Ridge of seafloor.” *Journal of Applied Physics* 98 (1993).
- Shearer, Peter M. *Introduction to Seismology*. Cambridge University Press (1999), 1999.
- Shuifer, M.I., E.S. Argal, and I.A. Dobrynin. “Propagation characteristics of a blast-induced seismic effect in the beds of structures during construction of the dam at the NO. 2 Kambaratinskaya HPP-2.” *Soil Mechanics and Foundation Engineering* 49 (2012): 13–18.
- Sleeman, Reinoud and Torild van Eck. “Robust automatic P-phase picking: an on-line implementation in the analysis of broadband seismogram recordings.” *Physics of The Earth and Planetary Interiors* 113 (1999): 265–275.

- Slunga, Ragnar, Sigurdur Rognvaldsson, and Reynir Bodvarsson. "Absolute and relative locations of similar events with application." *Geophysical Journal International* 123 (1995): 409–419.
- Smith, R J, Imperial Oil Resources, N S Alinsangan, and S Talebi. "Microseismic Response of Well Casing Failures at a Thermal Heavy Oil Operation." *SPE International*. 2002.
- St-Onge, Andy and David Eaton. "Noise Examples from Two Microseismic Datasets." *CSEG annual convention*. 2011, 2009–2012.
- Stein, Seth and Michael Wysession. *An introduction to Seismology, Earthquakes and Earth Structure*. Blackwell Publishing Ltd., 2003.
- Tarantola, Albert and Bernard Valette. "Inverse Problems = Quest for Information." *Journal of Geophysics* 50 (1982): 159–170.
- Tkalčić, Hrvoje, Mallory Young, Thomas Bodin, Silvie Ngo, and Malcolm Sambridge. "The shuffling rotation of the Earth's inner core revealed by earthquake doublets." *Nature Geoscience* 6 (May 2013): 497–502.
- Tselentis, G.-Akis. "Temporal variation of body wave attenuation as related to two earthquake doublets in W. Greece." *Pure and Applied Geophysics PAGEOPH* 140 (1993): 49–62.
- Vandecar, B Y J C and R S Crosson. "Determination of teleseismic relative phase arrival times using multi-channel crosscorrelation and least squares." *Bulletin of the Seismological Society of America* 80 (1990): 150–169.
- Verdon, James P. and J.-Michael Kendall. "Detection of multiple fracture sets using observations of shear-wave splitting in microseismic data." *Geophysical Prospecting* 59 (July 2011): 593–608.
- Verdon, J.P., J.-M. Kendall, D.J. White, and D.a. Angus. "Linking microseismic event observations with geomechanical models to minimise the risks of storing CO₂ in geological formations." *Earth and Planetary Science Letters* 305 (May 2011): 143–152.
- Vidale, John. "Complex polarization analysis of particle motion." *Bulletin of the Seismological Society of America* 76 (1986): 1393–1405.
- Waldhauser, F. and William Ellsworth. "A Double-Difference Earthquake Location Algorithm: Method and Application to the Northern Hayward Fault, California." *Bulletin of the Seismological Society of America* 90 (December 2000): 1353–1368.

- Waldhauser, Felix, David Schaff, Paul G Richards, and Won-young Kim. "Lop Nor Revisited : Underground Nuclear Explosion Locations , 1976 - 1996 , from Double-Difference Analysis of Regional and Teleseismic Data." *Bulletin of the Seismological Society of America* 94 (2004): 1879–1889.
- Warpinski, N R, Sandia Natl Labs, R B Sullivan, J E Uhl, Sandia Natl, K Waltman, and S R Machovoe. "SPE 84488 Improved Microseismic Fracture Mapping Using Perforation Timing Measurements for Velocity Calibration." *SPE International*. 2003, 1–11.
- Warpinski, N R, Sandia Natl, T B Wright, J E Uhl, B P Engler, P M Drozda, R E Peterson, and P T Branagan. "Microseismic Monitoring of the B-Sand Hydraulic-Fracture Experiment at the DOE / GRI Multisite Project." *SPE International* (1999): 242–250.
- Warpinski, Norm. "Microseismic Monitoring : Inside and Out." *SPE International*. 2009, 80–85.
- Westman, Erik, K. Luxbacher, and S. Schafrik. "Passive seismic tomography for three-dimensional time-lapse imaging of mining-induced rock mass changes." *The Leading Edge* (2012): 288–290.
- Wong, Joe, Leija Han, John C Bancroft, and Robert R Stewart. Automatic time-picking of first arrivals on noisy microseismic data. Technical report, 2009.
- Young, Paul, Shawn C Maxwell, Ted Urbancic, and B. Feignier. "Mining-induced Microseismicity: Monitoring and Applications of Imaging and Source Mechanism Techniques." *Pageoph* 139 (1992).
- Zhou, Rongmao, Lianjie Huang, James Rutledge, Huseyin Denli, and Haijiang Zhang. "Double-difference tomography of microseismic data for monitoring carbon sequestration." *SEG Technical Program Expanded Abstracts* (2009): 4064–4068.

APPENDIX A

Appendix: Partial derivatives determination

This section shows explicitly how to calculate the partial derivatives with respect to the model parameters $m = (t, x, y, z)^T$ for two events i and j recorded at the k th station for the DD algorithm. The observed arrival time t_k^{obs} for the i th event at the k th station is:

$$t_k^{obs} = t_o + \frac{1}{vp} [(x_k - x_i)^2 + (y_k - y_i)^2 + (z_k - z_i)^2]^{\frac{1}{2}}. \quad (\text{A-1})$$

Where x_k, y_k, z_k are the station coordinates, x_i, y_i, z_i, t_o the hypocentral parameters and vp the P-wave velocity in the source region. This is a nonlinear problem. We can have a rough idea of the hypocentral parameters by using an absolute location algorithm, and obtain the initial solution $m_o = (t_o, x_o, y_o, z_o)^T$ for a single event. To linearize the problem, we need to apply a first-order Taylor series expansion and find the partial derivatives with respect to all model parameters evaluated at the current model m_o , obtaining:

$$t(m) - t(m_o) = \frac{\partial t}{\partial m} (m - m_o). \quad (\text{A-2})$$

Where

$$\frac{\partial t}{\partial m} = \frac{\partial t}{\partial x} + \frac{\partial t}{\partial y} + \frac{\partial t}{\partial z} + \frac{\partial t}{\partial t}. \quad (\text{A-3})$$

$$\frac{\partial t_k^i}{\partial t} = 1. \quad (\text{A-4})$$

$$\frac{\partial t_k^i}{\partial x} = -\frac{1}{vp} \frac{(x_k - x_o)}{[(x_k - x_o)^2 + (y_k - y_o)^2 + (z_k - z_o)^2]^{\frac{1}{2}}}. \quad (\text{A-5})$$

$$\frac{\partial t_k^i}{\partial y} = -\frac{1}{vp} \frac{(y_k - y_o)}{[(x_k - x_o)^2 + (y_k - y_o)^2 + (z_k - z_o)^2]^{\frac{1}{2}}}. \quad (\text{A-6})$$

$$\frac{\partial t_k^i}{\partial z} = -\frac{1}{vp} \frac{(z_k - z_o)}{[(x_k - x_o)^2 + (y_k - y_o)^2 + (z_k - z_o)^2]^{\frac{1}{2}}}. \quad (\text{A-7})$$

Equations A-4 to A-7 are the partial derivatives evaluated at m_o . Thus, for the i th event recorded at the k th station, equation A-2 converts to:

$$(t_k^{obs})^i - (t_k^{cal})^i = \frac{\partial t_k^i}{\partial x} \Delta x^i + \frac{\partial t_k^i}{\partial y} \Delta y^i + \frac{\partial t_k^i}{\partial z} \Delta z^i + \Delta t^i. \quad (\text{A-8})$$

Consequently, the difference for two events i and j is obtained:

$$(t_k^i - t_k^j)^{obs} - (t_k^i - t_k^j)^{cal} = \frac{\partial t_k^i}{\partial x} \Delta x^i + \frac{\partial t_k^i}{\partial y} \Delta y^i + \frac{\partial t_k^i}{\partial z} \Delta z^i + \Delta t^i - \frac{\partial t_k^j}{\partial x} \Delta x^j - \frac{\partial t_k^j}{\partial y} \Delta y^j - \frac{\partial t_k^j}{\partial z} \Delta z^j + \Delta t^j. \quad (\text{A-9})$$

Where $(t_k^i - t_k^j)^{obs} - (t_k^i - t_k^j)^{cal}$ is the DD residual, and $(\Delta x^i, \Delta y^i, \Delta z^i, \Delta t^i, \Delta x^j, \Delta y^j, \Delta z^j, \Delta t^j,)$ are the eight unknown perturbations we need to determine to better fit the data. Equation A-9 is one single observation of the system of linear equations shown in equation 4.11.